Optical and quantum optical properties of a quantum dot-atomic vapor interface

Von der Fakultät Mathematik und Physik der Universität Stuttgart
zur Erlangung der Würde eines Doktors der Naturwissenschaften
(Dr. rer. nat) genehmigte Abhandlung

Vorgelegt von

Hüseyin Vural

aus Antakya

Hauptberichter:	Prof. Dr. Peter Michler
1. Mitberichter:	Prof. Dr. Tilman Pfau
2. Mitberichter:	Prof. Dr. Stephan Reitzenstein

Tag der mündlichen Prüfung: 9. Februar 2021

Institut für Halbleiteroptik und Funktionelle Grenzflächen
Universität Stuttgart

2021

Abstract

The pathway to advanced quantum technological applications often includes hybrid quantum systems of matter mediated by quantum-states of light. While the quantum-states of light are well suited as mediators of quantum information to remote nodes, hybrid systems are envisioned to fuse the in general complementary strength of individual ones to fulfill the promise of practical quantum technologies. Despite this clear advantage, combining together two different quantum systems is very challenging because of the inherent differences between the constituting components. Understanding the physics that underlines the hybrid system is crucial for carefully designing the experimental conditions.

This thesis examines a particular hybrid system formed by a single semiconductor quantum dot (QD) and cesium (Cs) atoms in a hot vapor. The interface is realized by Fock-states of light as mediators. While the QD is known to be, among other things, an efficient single-photon emitter, alkali vapors are established as storage media for classical light pulses. Achieving slow-light for Fock-states represents the first step in the implementation of a quantum memory, which is an important building block in photonic quantum technological applications. Furthermore, the capability of interfering single photons after they interacted with the vapor is of utmost importance to prove the validity of these hybrid systems in several branches of quantum technology.

To be beneficial for advanced quantum implementations, ultra pure and highly indistinguishable photons have to be generated on-demand. We utilize pulsed resonant excitation of single InGaAs QDs, which are engineered to emit at a wavelength matching the Cs-D_1 transitions,

to realize precisely timed emission of pure single and indistinguishable photons. This enables detailed studies of the interaction of one- and two-photon Fock-states with a hot atomic Cs vapor within the framework of the slow-light effect. Thanks to time-resolved measurements of the optical and quantum-optical properties of photons, a clear understanding of the photon-vapor interaction is gained, which is key knowledge for the implementation of complex quantum technology tasks. By exploiting the slow-light effect, a delay line for both aforementioned Fock-states is realized achieving high fractional delays, while the photon statistics of the transmitted light is investigated after the vapor. Moreover, the impact of the slow-light effect on photon wavepacket coherence is studied.
A major aspect of the present studies is related to the pulse distortion that is induced by the dispersion of the slow-light medium. On the one hand, via Hong-Ou-Mandel (HOM) measurements, we investigate the implications of pulse distortion for future quantum networks that rely on two-photon interference. On the other hand, we exploit the essential connection between dispersion and unique pulse distortion for time-domain high-resolution spectroscopy. In particular, a novel method based on slow-light photon-correlation is established: it allows to tackle the open problem of characterizing and understanding spectral diffusion dynamics of on-demand operated quantum emitters. With this method, assessing their performances for quantum optical applications by straightforward photon-correlation is achieved.

By using this method, the full extent of the dynamics of spectral diffusion is measured by probing the emitted photons of charged exciton states of single QDs under pulsed resonant excitation. Understanding the temporal evolution of emission line broadening will allow to tailor QD-based light sources for future realizations of multi-photon quantum implementations with even higher performances. This achievement will have an important impact on several fields of photonic quantum technology.

Contents

Danksagungen

Gott sei Dank für die vielfältige Unterstützung, die mir während dieser Arbeit zuteil wurde. Im Besonderen möchte ich herzlich danken:

- meinem Doktorvater Prof. Dr. Peter Michler für die große Unterstützung von Beginn an bis hin zur Finalisierung der Arbeit und die allzeitige herzliche Führung durch ihre verschiedenen Etappen,
- Herrn Prof. Dr. Tilman Pfau und Herrn Prof. Dr. Stephan Reitzenstein zur freundlichen Übernahme der Mitberichte, und Herrn Prof. Dr. Hans Peter Büchler für die Übernahme des Prüfungsvorsitzes,
- meinem Gruppenleiter Herrn Dr. Simone Luca Portalupi für die stete tatkräftige Unterstützung und das Teilen seiner wertvollen Erfahrungen, wie auch Herrn Dr. Ilja Gerhardt für seine herzliche und produktive Unterstützung über die gesamte Zeit,
- meinen Vorgängern am IHFG, deren Leidenschaft mir eine erhellende Weisung im dunklen Labor war: vorrangig Dr. Markus Müller, dessen Zielstrebigkeit ich nacheiferte, Dr. Jan F. Kettler, dessen Sorgfalt ich nachzuahmen versuchte und Dr. Mario Schwartz, dessen Ausdauer ich reproduzieren versuchte,
- meinen Studenten und Labor- und Bürofreunden für große Beiträge an meinem persönlichen Werdegang sowie der Arbeit: den Herren Julian Maisch, Jonas H. Weber, Tim Strobel, Julius Fischer, Simon Seyfferle, Stefan Simmler, Sasha Kolatschek, Simon Kern, Cornelius Nawrath sowie vielen weiteren Damen und Herren am IHFG, die alle gemeinsam der tollen Atmosphäre beitragen und mir viel bedeuten,

- Frau Sonja Humphrey, Herren Dr. Michael Jetter, Thomas Herzog, Ewald Wagner und Klaus Lehmann, die mit ihrer entgegenkommenden Art und Weise stete Quelle von Freude waren,
- sowie Herren Rene Rehwagen, dessen liebevolle Tritte mich erst soweit gebracht haben, und Jelde Elling dessen Motivation für die Wissenschaft ich gerne geteilt habe,
- meinen Freunden aus dem Studium der Physik, Gottes und der Welt: Lukas Eisemann, Cebrail Pür und Ömer Bayraktar,
- meinen verehrten Lehrerinnen und Lehrern der Uhlandschule in Gladbeck und des Gymnasiums Wanne in Herne, meinen verehrten Dozenten und Betreuern der TU Dortmund und Uni Stuttgart und allen weiteren verehrten Persönlichkeiten die meinem schulischen Werdegang beigetragen haben,
- meinen Eltern und Geschwistern, die mir die höchste Liebe und Geduld entgegen gebracht haben und denen ich meine Arbeit widme.

Abbreviations

AlAs	aluminium arsenide
APD	avalanche photo diode
BS	beam splitter
Cs	cesium
CX	charged exciton
e	electron
FCSPC	frequency-correlated single-photon counting
FPI	Fabry-Pérot interferometer
FWHM	full width at half maximum
GaAs	gallium arsenide
h	hole
HOM	Hong-Ou-Mandel
HRPL	high resolution photoluminescence
HWP	half wave plate
InGaAs	indium gallium arsenide
MOVPE	metal-organic vapor-phase epitaxy
MZI	Mach-Zehnder interferometer
OU	Ornstein-Uhlenbeck
PBS	polarization beam splitter
PSB	phonon side bands
QD	quantum dot
QWP	quarter wave plate

TAC time-to-amplitude converter
TCSPC time-correlated single-photon counting
TCSPCp TCSPC under postselection
TTM time-tagging module
XX biexciton
X exciton
WL wetting layer
ZPL zero-phonon line

Chapter 1

Introduction

Since the turn of the millennium, the development of advanced quantum technologies points to much more practical applications. Famously described as the second quantum revolution [1], quantum effects have been continuously exploited for much sought-after practical applications.
To this end, various quantum systems are being studied, including quantum states of light [2–4], natural atoms and ions [5, 6], defects in solid-state like color centers in diamond [7] and semiconductor quantum dots [8], as well as quantizations in mesoscopic superconductors [9] and nanomechanical structures [10].

Within the scope of quantum technologies, quantum states of light are well suited as mediators of quantum information between remote nodes using optical fibers or free space links to satellites in order to form a global quantum network [11]. Using single-photon quantum bits, it is expected that photonic technologies provide advantages for secure communication [12–14], advances in information processing and computation [15, 16], and sensing with precision beyond the standard quantum limit [17–19].

Quantum memories play a central role in the synchronization of the temporal modes of photonic quantum bits. These memories are generally realized in long-lived ground level spin states [20], which is challenging to realize in the systems used for photon generation at high rates [2–4]. An appealing approach to circumvent this issue is based on hybrid quantum systems [21–23], which are envisioned

to fuse their complementary strengths withdrawing their limitations. The realization of a quantum memory capable of storing an retrieving information carried by non-classical light states will have an enormous impact on several fields of photonic quantum technologies.

Semiconductor quantum dots (QDs) brought impressive progresses as sources of single and entangled photons [8,24–27] due to the strong emission of a single transition into the zero-phonon line as well as their compatibility with photonic resonator structures. The highest reported rates of single photons to date (40 MHz out of 76 MHz excitation rate) [28] operate the QD in an open micro-cavity, while multi-photon interferometry with up to 20 input photons [16] was recently realized with a QD embedded in a micropillar structure. Remarkably, both of these emitters are single InGaAs quantum dots, revealing the strength of this technology for the generation and collection of highly coherent single-photons.

Storing photons in order to introduce a waiting time for parallel quantum operations increases the efficiency of quantum gates with multi-photon inputs. Regarding this task, atomic alkali vapors offer deterministic coherent storage and retrieval [29–31]. However, an interface realizing a quantum memory for QD emission in an alkali vapor is still an open issue due to decoherence and noise in both systems. Within the vapor, the strong control pulses needed for storing single photons induce residual signals via processes like Raman scattering and four-wave-mixing, which eventually corrupt the quantum state of the retrieved photons [30,32]. Filtering and discrimination of signals become even more challenging in connection with the broadening of QD emission spectra. The relatively large natural broadening of its emission line width, which is further increased due to inhomogeneous broadening processes, reduces the spectral matching to the atomic transitions [23, 33]. For these reasons, a working memory for QD photons remains elusive.

Nevertheless, preliminary steps have been taken to create a practical QD-alkali vapor interface. Up to now, the efforts focused on achieving efficient absorption of QD photons by alkali vapors [34,35], slowing down light via chromatic dispersion of the Doppler-

broadened D-transitions [23, 36, 37], and narrow-band filtering in cesium (Cs)-vapor by Faraday-anomalous dispersion [38]. In these studies, however, non-resonant pumping or resonant continuous-wave excitation of the QD was used, which lacks the ability to create precisely timed emission, that is important for efficient multi-photon quantum implementations.

In this thesis, we realize an interface of a hot Cs vapor and on-demand generated QD photons, which expands existing efforts in the following aspects: First, this study operates with resonantly generated photons (under the π-pulse excitation), in order to minimize the impact of excitation on both the line broadening and timing jitter. Secondly, the interaction of Fock-states of light with the vapor is investigated in various experiments with regard to their optical and quantum-optical properties. Thirdly, the interface is utilized as a novel spectroscopic apparatus that enables insights to the QD's environmental coupling. This is made possible by the strong dispersion in the vapor which imprints the frequency domain of photons onto the time domain by unique temporal shapes. By this spectroscopic method, the outstanding problem of characterization of spectral diffusion dynamics of QDs is addressed, by probing the on-demand emitted photons after the vapor. Finally, the influence of pulse distortion on quantum interference is investigated to evaluate the potential of this interface for realistic applications. This thesis is divided as follows:

Chapter 2 first introduces the basic properties of semiconductor quantum dots and their transitions from which the single-photon emission results. Next, the linear response of the cesium vapor is discussed as it is responsible for the slow-light effect. The emphasis of this introductory chapter is on the comprehensive description of time-resolved two-photon interference for exponentially decaying photon wavepackets and the related correlation functions. All fundamentals required to describe the following experimental studies are introduced.

Chapter 3 describes the overall experimental setup and methods required for the characterization of basic quantum dot properties in both frequency and time domain.

Chapter 4 is dedicated to the experimental characterization of the building blocks of the presented hybrid interface. In particular, the distinct optical and quantum optical features of single quantum dots are exemplarily demonstrated for the investigated heterostructure. The important on-demand generation of single and indistinguishable photons is investigated and the formation of two-photon Fock-states is demonstrated.

Chapter 5 gives a comprehensive study on optical and quantum optical properties of quantum-states of light after their slowing down upon interaction with the Cs vapor.
The first section is devoted to an introduction and benchmarking of the concepts of time-domain spectroscopy by the slow-light medium, which relies on the medium's strong dispersion. Mapping the frequency domain of QD emission spectrum onto the time domain after propagation through the vapor is demonstrated. Based on this, in the next section, a novel photon-correlation technique is established, which allows the investigation of the spectral diffusion dynamics of on-demand operated QDs.
In the third section, the quantum-states of light are investigated while using the medium as a variable delay line. The propagation of single and two-photon Fock-states in the dispersive medium is experimentally observed and validated. In the final section, we explore the influence of pulse distortion, that arises from the Cs vapor - single-photon interaction, on the quantum interference of transmitted photons.

Chapter 2

Theoretical background

In the following sections, first the fundamentals are briefly introduced that determine the electronic structure and photoluminescence of the semiconductor quantum dots (QDs) this work deals with. This is followed by the description of the role of alkali vapors for the hybrid interface. Finally, the basics of a single-photon wavepacket propagation and quantum interference is derived in a time-resolved manner.

2.1 Semiconductor quantum dots

Electronic configuration

Epitaxially grown semiconductor quantum dots being considered in this work are lense shaped heterostructures that confine electronic motion in all directions giving rise to an electron-photon interaction similar to natural atoms [8, 39, 40]. Using metalorganic vapor-phase epitaxy in the Stransky-Krastanow mode [41], the growth is conducted by the subsequent deposition of semiconductor materials. In the present case, the substrate is GaAs and the QD layer is InAs which possess a lattice constant mismatch of $\sim 7\,\%$ [42]. This forms a strained InAs quantum well, usually referred to as the wetting layer (WL), which eventually foster the self-assembled formation of InAs islands. Finally the substrate material is used to overgrow the sample giving rise to InGaAs QDs due to material diffusion in a GaAs barrier matrix. Typically the QD's height ($\sim 5\,\mathrm{nm}$) is much less than

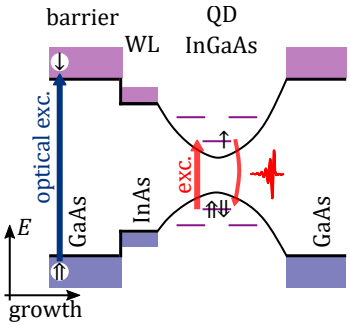

Figure 2.1. Schematic energy level diagram of an InGaAs QD under non-resonant optical excitation, resonant excitation of a charged exciton and its recombination via photon emission.

the diameter ($\sim$ 20 nm) resulting in almost an order of magnitude larger confinement energies along the growth direction. Thus, the often non-uniform lateral potential has a chief role in determining the QD's transitions. In contrast to the alternative growth with molecular beam epitaxy, the vapor phase deposition operates at higher chamber pressures and temperatures that allow higher growth rates facilitating fabrication at industrial dimensions [43]. However, the benefits are accompanied by unwanted crystal defects that impoverish the photonic properties of these QDs compared to those grown by molecular beam epitaxy.

The QDs lateral confinement potential can be approximated by a two-dimensional harmonic oscillator. However, the inherent strain and generally present anisotropy results in peculiarities. Being the quantization axis along the growth direction, the ground state electron (e) states are s-like and two fold degenerate, whose spin projections in the angular momentum basis is denoted as ($\uparrow$ and $\downarrow$). The ground state of the valence-band hole (h) states are p-like, while the highest energy states are governed by the so called heavy holes with the projection $J_z = \pm 3/2$ denoted as ($\Uparrow$ and $\Downarrow$) [44]. The light hole states with $J_z = \pm 1/2$ are energetically tens of meV lower and the

split-off states with $J = 1/2$ even hundreds of meV, which is why they are generally disregarded. However, mixing of heavy hole-light hole states can have in particular significant impact on the spin and optical properties of a QD's transition [42]. As for the generation of single photons, an optically active e-h pair is constituted by the so called bright excitons ($\Uparrow\downarrow$ or $\uparrow\Downarrow$) and charged excitons (positive: $\Uparrow\Downarrow\uparrow$ or $\Uparrow\Downarrow\downarrow$, negative: $\Uparrow\downarrow\uparrow$ or $\Downarrow\downarrow\uparrow$) which posses an excessive resident charge carrier in the QD. However, in general the present anisotropy lifts the degeneracy of the exciton states due to an effect by the electron-hole Coulomb exchange interaction leading to two linearly polarized transitions [45]. In contrast, a charged exciton does exhibit degeneracy (in the absence of a magnetic field [46]) due to the Kramers theorem resulting in a single emission line that renders it interesting for photonic links. The charge state of the QD can be set by (often unintentional, in MOVPE due to carbon and hydrogen) doping with impurities or be deterministically initialized by coupling to heavily doped layers through a tunnel barrier in voltage controlled diode devices [47].

Optical excitation

Figure 2.1a depicts a schematic energy level diagram of the QD along the growth direction. The discrete states of the QD can be populated by charge carriers using electrical diode structures or by means of optical excitation with a laser energy above the GaAs band-gap. Mediated by non-radiative relaxation processes, the charge carriers are captured within tens of picoseconds into the states of the WL and the discrete levels of the QD, but also in impurities which especially occur at layer interfaces [48]. The density of states and to a certain extent transition strength are revealed in the photoluminescence spectrum, which contains the continuous spectrum of the WL and several discrete (cascaded) transitions of the randomly and multiply occupied ground and excited states of the QD conduction and valence states. The charge fluctuations which necessarily occur in this non-resonant excitation scheme leads to decoherence and substantial

inhomogeneous broadening of transitions, limiting quantum optical properties [49].
In recent years, resonant excitation schemes for selective population of transitions in the levels of a single QD have established [27, 50]. Under ultra-fast pumping near-unity state preparation fidelity can be reached, rendering QDs nowadays as the best on-demand single-photon sources emitting at a single transition [16, 51]. However, decoherence still occurs as a result of the QD's coupling to its fluctuating environment. Major contributions stem from coupling of exciton-acoustic phonon bands, the Stark-effect of fluctuating charges trapped in the vicinity of the QD and hyperfine coupling of the charge carrier spins to fluctuating nuclear spins of the atoms constituting the QD [33, 42, 52–56].

2.2 Absorption and dispersion in alkali vapor

An atomic vapor contained in a glass cell allows a very robust and comfortable investigation of basic atom-light interactions and can be designed to reach important goals in quantum technologies [31, 57]. Alkali metals, the elements of the first main group possess a single electron in their outermost shells which simplifies optical investigations and theoretical description. Besides spectroscopy, alkali vapors have found numerous applications in combination with non-classical light states, relevant ones with regard to QDs are Faraday-filtering [38] and broad-bandwidth quantum memories [30, 58]. The focus in our work is on the dispersive properties of a hot vapor, as it can give rise to the so called fast- and slow-light effects [59, 60]. The latter one significantly reduces the group velocity v_g of an electromagnetic pulse with respect to free space propagation. The transitions of rubidium and cesium are most suitable as they match the emission wavelengths of high performance GaAs/AlGaAs and InGaAs/GaAs QDs [23, 61], respectively, while the atomic hyperfine splittings nicely fit to QDs line widths. This facilitates them as single photon de-

lay lines without the need for complex manipulation of the storage medium.

With this regard, the knowledge of the linear response of a vapor to a single photon or more general, to a weak-probe is of major interest. This demand has been satisfied for the main transitions D_1 and D_2 of alkali vapors by a publicly accessible program named ElecSus [62]. It calculates the electric susceptibility $\mathcal{X}$ of an atomic ensemble which is used to derive the complex refractive index $n_c = \sqrt{1+\mathcal{X}} \approx 1 + \mathcal{X}_{re}/2 + i\mathcal{X}_{im}/2$. The real part describes the dispersion of the atomic ensemble via the refractive index $n(\omega) = 1 + \mathcal{X}_{re}/2$ over the angular frequency ω, while the imaginary part delivers its absorption coefficient via $\alpha(\omega)/2k = \mathcal{X}_{im}/2$, where k is the wavenumber.
ElecSus assumes Lorentzian line shapes for the transitions originated in natural lifetime broadening and a dipole-dipole induced self-broadening at higher temperatures. Moreover, as the main broadening mechanism is given by the Doppler effect, the line shapes are convoluted with the corresponding Gaussian yielding inhomogeneously broadened lines. The susceptibility depends besides on the transition strength, that is calculated using a matrix representation of the atomic Hamiltonian in the completely uncoupled basis, linearly on the number density, which is determined strongly by the temperature dependence of the vapor pressure. This is why, the vapor temperature T_V is a tuning knob for its linear response.

Figure 2.2a depicts exemplary absorption and refractive index profiles of the cesium D_1 ($6^2S_{1/2} \rightarrow 6^2P_{1/2}$ at $\sim 894.5\,\mathrm{nm}$) hyperfine-split transitions ($\Delta F' \sim 1\,\mathrm{GHz}$ and $\Delta F \sim 9\,\mathrm{GHz}$, where F' and F denote the total angular momentum of the first excited and ground states, respectively) for a vapor temperature of 25 °C and 125 °C, respectively. Comparing the linear response an almost unchanged line shape over the frequency is found (thick curve represents 25 °C and the thin one 125 °C). There are four absorption peaks with Voigt-profiles arising from the Doppler-broadening with amplitudes coming from their respective transition strength (see appendix and [63, 64]), however with an increase of absorption strength by a factor of thou-

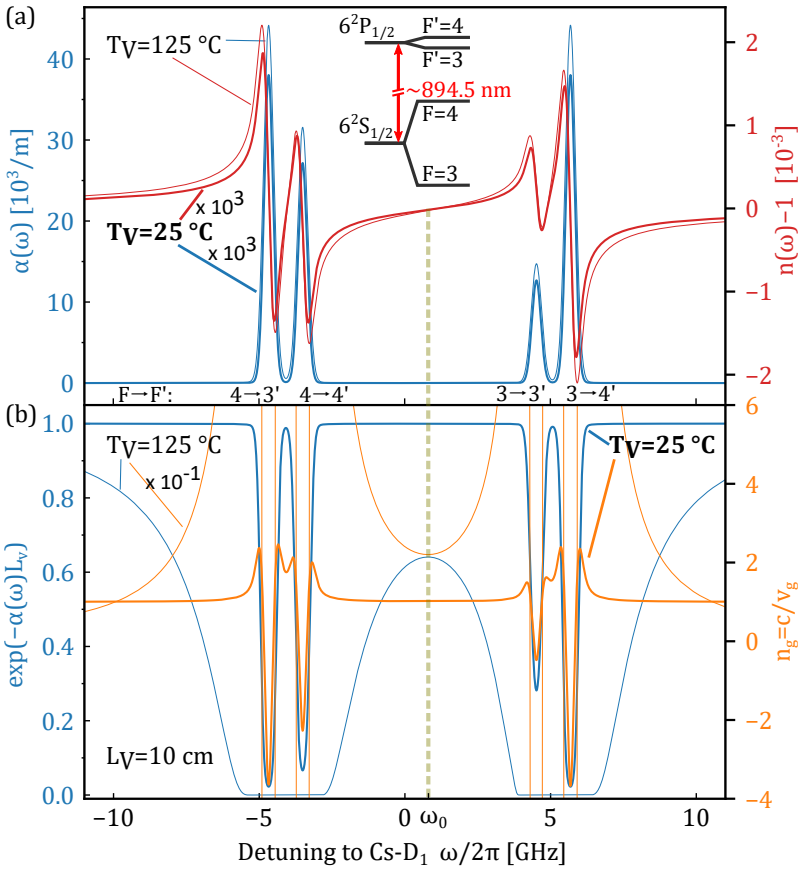

Figure 2.2. Linear response of a Cs vapor over the hyperfine split cesium D_1 transitions ($6^2S_{1/2} \rightarrow 6^2P_{1/2}$ at $\sim$ 894.5 nm). F' and F denote the total angular momentum of the excited and ground states, respectively. Inset shows the relevant energy level diagram. (a), Absorption coefficient α and refractive index n for two vapor temperatures T_V. Light curves correspond with 125 °C and thick curves with 25 °C. (b) Transmission profile and group index n_g for a certain length L_V of the vapor cell. ω_0 indicates the frequency at which least pulse distortion is expected for a pulse propagation through the vapor.

sand for the higher temperature. The refractive index compares in exact analogy as both are connected via the Kramers-Kronig relation [65]. The regime of anomalous dispersion at the resonances and the regime of normal dispersion in between preserve their shape but with a factor of thousand increase in absolute magnitude for the real part of the susceptibility. In consequence, the temperature change has a huge impact on both the speed v_g of a propagating light pulse and its transmission.

The group velocity of a light pulse within the medium can be estimated by $v_g = c/n_g$, where the group index is defined as $n_g(\omega) = n(\omega) + \omega \frac{\partial n}{\partial \omega}$. Figure 2.2b shows n_g and the transmission profile $\exp(-\alpha L_V)$ of a vapor with length $L_V = 10\,\mathrm{cm}$. Increasing the vapor temperature turns the transmission profile, where all four absorption peaks are distinctly present, to a complete merging of neighboring resonances. The transmission now is reduced over tens of GHz reaching zero at the resonances and leaving a bell shaped transmission window between the two further apart (ground-state) transitions.

At the transmitted frequencies, the initial group velocity can be reduced by more than an order of magnitude. The transmission window in the center of the transitions surviving at high temperatures is particularly appealing. As the group index has a local extremum there, the group velocity dispersion possesses a zero crossing which falls together with the maximum of the bell shaped transmission window at ω_0. Consequently a broad bandwidth pulse with this carrier frequency will experience both the least distortion and absorption when propagating through the vapor.

Although anomalous dispersion at the resonances allows fast light propagation, it will play no role for our experiments since strong absorption at these frequencies prevents any detected signal.

2.3 Quantum optics of the single-photon wavepacket

2.3.1 The single-photon wavepacket

We consider single photons generated as a result of spontaneous emission from a two-level system after its excitation by a short inversion pulse. The photon wavepacket created in this way is in the time domain very closely described by an exponentially decaying oscillation at the transition frequency [64] which corresponds to a Lorentzian spectrum in the frequency domain. For such a photon wavepacket the narrow bandwidth approximation holds, that is the spectral line width is much narrower than the carrier frequency. Assuming a single polarization and transversal mode profile, the quantum state of the single-photon wavepacket can be defined as [66]:

$$|1\chi\rangle = \hat{A}^\dagger(\chi)|0\rangle = \int_{\mathbb{R}} d\omega\ \chi(\omega)\hat{a}^\dagger(\omega)|0\rangle \quad . \tag{2.1}$$

Hereby, the creation operator $\hat{a}^\dagger(\omega)$ of a monochromatic single photon mode at angular frequency ω obeys the usual bosonic commutation relations:

$$\left[\hat{a}_i(\omega), \hat{a}_j^\dagger(\omega')\right] = \delta_{ij}\delta(\omega - \omega') \tag{2.2}$$

where i, j indicate polarization or spatial modes. The normalization of the wavepacket states hence require $\int d\omega |\chi(\omega)|^2 = 1$. Single-photon wavepackets have the intriguing property to resemble classical electromagnetic fields in many aspects [67] while showing non-classical features, too. To interpret the coefficients $\chi(\omega)$ of the states $|1\omega\rangle = \hat{a}^\dagger(\omega)|0\rangle$, we calculate the probability to find the photon at a

given frequency:

$$\begin{aligned} |\langle 1\omega|1\chi\rangle|^2 &= |\langle 0|\hat{a}(\omega)\int d\omega'\ \chi(\omega')\hat{a}^\dagger(\omega')|0\rangle|^2 \\ &= |\langle 0|\int d\omega'\ \chi(\omega')\left(\hat{a}^\dagger(\omega')\hat{a}(\omega)+\delta(\omega-\omega')\right)|0\rangle|^2 \\ &= |\chi(\omega)|^2 = \chi(\omega)\chi^*(\omega) \quad , \end{aligned} \tag{2.3}$$

where $\hat{a}(\omega)|0\rangle = 0$ was used. Thus, $\chi(\omega)$ is the amplitude spectrum of the photon wavepacket. Using the Fourier transformation $\mathcal{FT}$:

$$\chi(t) = \mathcal{FT}\left\{\chi(\omega)\right\} = \int_{\mathbb{R}} \frac{d\omega}{\sqrt{2\pi}} e^{-i\omega t}\chi(\omega) \quad , \tag{2.4}$$

and defining

$$\hat{a}(t) = \int_{\mathbb{R}} \frac{d\omega}{\sqrt{2\pi}} e^{-i\omega t}\hat{a}(\omega) \quad , \tag{2.5}$$

it follows $|1\chi\rangle = \int d\omega\ \chi(\omega)\hat{a}^\dagger(\omega)|0\rangle = \int dt\ \chi(t)\hat{a}^\dagger(t)|0\rangle$. The probability to detect the photon wavepacket at a given time instant t is $|\chi(t)|^2 = |\langle 1t|1\chi\rangle|^2$, thus $\hat{a}^\dagger(t)$ is identified as the creation operator of a photon at time t. The relations (2.2) apply also for this operator.

Propagation of the photon in a linear medium

The propagation of a single photon wavepacket in free space or a linear dispersive medium is a fundamental part of this thesis. It is described by the unitary transformation [68]:

$$\hat{a}(\omega) \mapsto e^{-i\omega\frac{Ln(\omega)}{c}}\hat{a}(\omega) \quad , \tag{2.6}$$

where L is the propagation distance, c the speed of light and $n(\omega)$ the refractive index of the medium. Please note, that in the final step of calculations, the absorption $\alpha(\omega)$ according to the Beer-Lambert's law is taken into account by transforming to the complex refractive index $n(\omega) \mapsto n(\omega) + \frac{i}{2\omega/c}\alpha(\omega)$, where absorption appears in analogy to a frequency dependent detection efficiency [67].

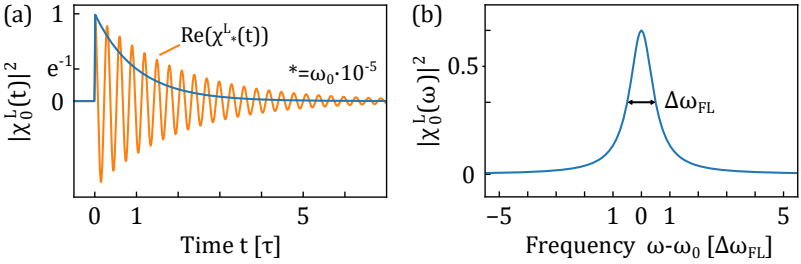

Figure 2.3. (a), Exponentially decaying time domain of the considered wavepackets in units of the decay constant τ while hitting the detector with its sharp front. For a single-photon only a time-correlated measurement on an ensemble will deliver the whole curve, while it constitutes the probability distribution for a single one. The reel part of the temporal amplitude (orange) is illustrated with a 10^{-5} slower oscillation frequency than typical in the experiments. (b), Lorentzian frequency domain of the wavepackets in units of the Fourier-limited line width $\Delta\omega_{FL} = \tau^{-1}$.

The general amplitude spectrum we consider takes the form:

$$\chi_0^L(\omega) = \sqrt{\frac{2\tau}{\pi}} \frac{e^{i\omega t_0}}{1 - 2i\tau(\omega - \omega_0)} e^{i\omega \frac{Ln(\omega)}{c}} \quad , \tag{2.7}$$

where t_0 is the time of photon generation, τ the decay constant and ω_0 the carrier frequency of the wavepacket which will be indicated by the subscript. The power spectrum $|\chi_0^L|^2$ thus is a Lorentzian with a Fourier-limited line width of $\Delta\omega_{FL} = \tau^{-1}$ regardless the propagation in a (non-absorbing) linear medium. In *free space* the temporal amplitude after $\mathcal{FT}$ has the form:

$$\chi_0^L(t) = \sqrt{\frac{1}{\tau}}\, \Theta(t - t_0 - \frac{L}{c}) e^{\frac{-\left(t - t_0 - \frac{L}{c}\right)}{2\tau}} e^{-i\omega_0\left(t - t_0 - \frac{L}{c}\right)} \quad , \tag{2.8}$$

where Θ is the Heaviside step function (Fig. 2.3). In this case, as expected, the propagation induces only a delay of $\delta t = \frac{L}{c}$ in detection time while the photonic temporal shape remains the same exponential decay $|\chi_0^L(t)|^2 = |\chi_0^0(t - \frac{L}{c})|^2$. In contrast, the time domain

is strongly affected by a present chromatic dispersion, as each frequency component in Eq. (2.7) propagates a different effective length $L \cdot n(\omega)$. This results in an interference effect of the various frequency components of the wavepacket, which is as intriguing as the interference of a photon after the two spatial modes of a double-slit or an interferometer. It expresses itself as a shift in detection time due to a fast-/slow-light effect and accompanied pulse distortion, where group velocity dispersion is a famous subset of this effect [65].

2.3.2 Mach-Zehnder interferometer and quantum coherence

The famous Mach-Zehnder interferometer (MZI) consists of two beam splitters, where the first one splits each of the two independent incoming modes and combines them in two outgoing modes. After a certain path length, the second beam splitter superposes each splittet mode in its outgoing modes. Depending on the input modes and the path length difference, it can serve as a tool to study classical and/or quantum interference.

The lossless beam splitter connects input modes $\hat{a}_1, \hat{a}_2$ to output modes $\hat{a}_3, \hat{a}_4$ [66] via the transformation:

$$\begin{pmatrix} \hat{a}_3(\omega) \\ \hat{a}_4(\omega) \end{pmatrix} = \begin{pmatrix} t' & r \\ r' & t \end{pmatrix} \begin{pmatrix} \hat{a}_1(\omega) \\ \hat{a}_2(\omega) \end{pmatrix} \quad , \tag{2.9}$$

where the reflection and transmission amplitudes of the output modes (r, t) and (r', t') are constants due to the narrow bandwidth framework. Requiring relations (2.2) to hold and conservation of energy $\sum_i \hat{a}_i^\dagger(\omega)\hat{a}_i(\omega) = const.$ before and after the beam splitter yields the following constrains:

$$\begin{aligned} |r'| = |r|,\ |t'| = |t|,\ |r|^2 + |t|^2 = 1 \\ r^* t' + r' t^* = 0 = r^* t + r' t'^* \quad , \end{aligned} \tag{2.10}$$

which can be fulfilled by the choice $r = r' = i\sin(\theta)$, where $\theta = \pi/4$ results in the symmetric beam splitter. The choice used in this the-

ses introduces the phase $-i$ to the reflected mode of the creation operator: $\hat{a}_1^\dagger(\omega) \mapsto \frac{1}{\sqrt{2}}(\hat{a}_3^\dagger(\omega) - i\hat{a}_4^\dagger(\omega))$.

Traditionally, the detection of one output of a MZI is referred to as first-order coherence which is defined as:

$$G_i^{(1)}(\Delta L) = \langle \hat{E}_i^-(t)\hat{E}_i^+(t + \frac{\Delta L}{c})\rangle \quad , \tag{2.11}$$

with the continuous-mode quantized electric field operator in a single spatial and polarization mode within the narrow bandwidth approximation [69]: $\hat{E}_i^+(L,t) \propto \int d\omega\, \hat{a}_i(\omega)\, e^{-i\omega(t-\frac{n(\omega)L}{c})}$.

Exemplarily, a single photon wavepacket input at $t_0 = 0$ shall be considered which is transformed threefold by the first beam splitter (BS), by propagation of path lengths L and $L' = L+\Delta L \geq L$ in each output mode (Ph), respectively, and a second beam splitter (BS):

$$\begin{aligned}
|1\chi\rangle_{in} = |1\chi_0^{0;1}\rangle &= \int d\omega\ \chi_0^0(\omega)\hat{a}_1^\dagger(\omega)|0\rangle \\
\overset{BS}{\mapsto} \frac{1}{\sqrt{2}} &\int d\omega\ \chi_0^0(\omega)\left(\hat{a}_3^\dagger(\omega) - i\ \hat{a}_4^\dagger(\omega)\right)|0\rangle \\
\overset{Ph}{\mapsto} \frac{1}{\sqrt{2}} &\int d\omega\ \chi_0^0(\omega)\left(\hat{a}_3^\dagger(\omega)e^{i\omega\frac{L}{c}} - i\hat{a}_4^\dagger(\omega)e^{i\omega\frac{L'}{c}}\right)|0\rangle \\
\overset{BS}{\mapsto} \frac{1}{2} &\int d\omega \left(\chi_0^L(\omega) - \chi_0^{L'}(\omega)\right)\hat{a}_5^\dagger(\omega) - \left(\chi_0^L(\omega) + \chi_0^{L'}(\omega)\right) i\hat{a}_6^\dagger(\omega)\,|0\rangle \\
|1\chi\rangle_{out} = \frac{1}{2} &\left(|1\chi_0^{L;5}\rangle - |1\chi_0^{L';5}\rangle - i\left(|1\chi_0^{L;6}\rangle + |1\chi_0^{L';6}\rangle\right)\right)
\end{aligned} \tag{2.12}$$

The probability to detect the photon for instance at output 5 is then

given by:

$$
\begin{aligned}
&|\langle 0|\hat{a}_5(t)|1\chi\rangle_{out}|^2 = \frac{1}{4}|\chi_0^L(t) - \chi_0^{L'}(t)|^2 \\
=&\frac{1}{4}\left(|\chi_0^L(t)|^2 + |\chi_0^{L'}(t)|^2 - \chi_0^L(t)\chi_0^{*L'}(t) - \chi_0^{*L}(t)\chi_0^{L'}(t)\right) \\
=&\frac{1}{4\tau}\{\Theta(t-\frac{L}{c})e^{-(t-\frac{L}{c})/\tau} + \Theta(t-\frac{L+\Delta L}{c})e^{-(t-\frac{L+\Delta L}{c})/\tau} \\
&- 2\Theta(t-\frac{L}{c})\Theta(t-\frac{L+\Delta L}{c})e^{-(t-\frac{L+\Delta L}{c})/\tau}e^{-\frac{\Delta L}{2c\tau}}\cos\left(\omega_0\frac{\Delta L}{c}\right)\}
\end{aligned}
\tag{2.13}
$$

The first two detection terms in Eq. (2.13) appear as if the photon took the mode of path length L or L', while the last term appears as a damped oscillation over the path length difference hitting the detector only when the time for the longer path has elapsed. For equal paths ($\Delta L = 0$) nothing can be detected at this output, i.e. incoming photons are guided always to the other port. For increasing ΔL one would observe oscillation of detection rates showing classical interference of the photon [49, 65]. Remarkably, any detection event t_D within $\Delta t_L = \frac{L}{c} \leq t_D < \Delta t_{L+\Delta L}$ signifies a photon that has taken the short path of length L without interference. In the same way, too late detection events are signified as a photon that has taken the long path. For a path length difference well exceeding the coherence length $2\tau c$ of the photon, classical interference does not show up any more in the now unbalanced MZI, since the photonic path can be identified with certainty based on the detection time.

In our experiments a stream of consecutively generated photons is fed into a MZI from one input port as depicted in Figure 2.4a, followed by photon correlation measurements at the outputs, which is traditionally [66] referred to as the second-order coherence:

$$
G^{(2)}_{i,j}(t,\delta t) = \langle \hat{E}_i^-(t)\hat{E}_j^-(t+\delta t)\hat{E}_j^+(t+\delta t)\hat{E}_i^+(t)\rangle \tag{2.14}
$$

Each wavepacket of the initial state $|1\chi_1, 1\chi_2\rangle_{in} = |1\chi_1^{0;1}, 1\chi_2^{L_0;1}\rangle$ (the subscript i of $\chi_i^{j;k}$ indicates the carrier frequency, the superscript

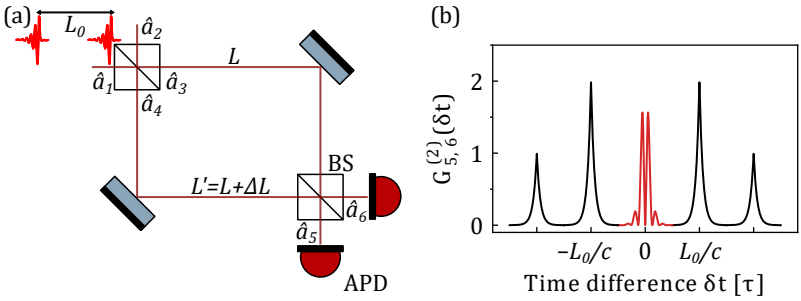

Figure 2.4. (a), Mach-Zehnder interferometer (MZI) consisting of two beam splitters (BS), spatial modes $\hat{a}_i$, path lengths L and L'. (b), For pairs of consecutive photons the unbalanced MZI with $\Delta L = L_0$ yields two-photon interference in the central peak of the second-order coherence for the case that photons have taken different paths to coincide at the output beam splitter; depicted for $\delta\omega = 3\Delta\omega_{FL}$. Combinations of photon paths that yield no temporal coincidence display cross-correlation peaks.

j before the semicolon indicates the propagation length and k marks the spatial mode; see Eq. (2.7) and Eq. (2.12)) transforms through the MZI to deliver the following correlation pattern at different output modes:

$$|\langle 0|\hat{a}_5(t_1)\hat{a}_6(t_2)|1\chi_1, 1\chi_2\rangle_{out}|^2 \tag{2.15a}$$

$$= \frac{1}{4}|\chi_1^L(t_1)\chi_2^{L+L0}(t_2) + \chi_1^L(t_2)\chi_2^{L+L0}(t_1) \tag{2.15b}$$

$$-\chi_1^{L'}(t_1)\chi_2^{L'+L0}(t_2) - \chi_1^{L'}(t_2)\chi_2^{L'+L0}(t_1) \tag{2.15c}$$

$$+\chi_1^L(t_1)\chi_2^{L'+L0}(t_2) - \chi_1^L(t_2)\chi_2^{L'+L0}(t_1) \tag{2.15d}$$

$$+\chi_1^{L'}(t_2)\chi_2^{L+L0}(t_1) - \chi_1^{L'}(t_1)\chi_2^{L+L0}(t_2)|^2 \tag{2.15e}$$

Hereby, $t_2 = t_1 + \delta t$ shall account for different detection times and detector locations that are generally not at equal distance to the beam splitter. The absolute square in Eq. (2.15a) leads to multiplication of intensities and amplitudes similar to Eq. (2.13), which could give

rise to interference phenomena. In deed, even new interference features arise as a consequence of the multi-photon state. First of all, the outcome has no phase sensitivity to L_0 as expected for an interferometer and classical interference. Furthermore, the (complex conjugate) multiplication of the terms as in (2.15b, 2.15c) where both photons have taken the same path of the interferometer do not neither show a path length dependent interference. In contrast, the multiplication of terms where one of the photons has taken a different path show up the usual path length difference dependent oscillation, however now for the coincidence detection.

More remarkably, the terms where both photons have taken both of the paths yields a phase dependence which is doubled with regard to the usual phase dependency. This is due to the detection of two photons where each contribute with the factor for the single-photon interference described above. Also as a result of the two photon detection, damping over the path length difference is not $e^{-\frac{\Delta L}{2c\tau}}$ as in the single-photon interference, but $e^{-\frac{\Delta L}{c\tau}}$ since each photon contribute with the damping factor.

Yet, the most interesting feature arises from the term (2.15e), where the first photon takes the longer interferometer path while the second one takes the short arm. If they temporally overlap at the second beam splitter, a correlation pattern arises showing up interference over the detection time difference δt which depends on the carrier frequency difference $\delta\omega$ of the photons. The most striking property here is the absence of a true coincidence (i.e. coalescence at $\delta t = 0$). Figure 2.4b shows the correlation histogram that arises when an unbalanced MZI is fed by two successive photons with a carrier frequency difference that amounts to three times their bandwidth $\Delta\omega_{FL}$. In the unbalanced interferometer classical interference is not present showing only the quantum interference in the central coincidence peak and at the sides the cross-correlation peaks of photons that do not coincide temporally at the output beam splitter. In the following, this quantum effect, which is often referred to as two-photon interference at the beam splitter, is discussed in more detail.

2.3.3 Time-resolved two-photon interference

An unbalanced MZI eliminates path length dependent classical interference and yields at the output beam splitter probabilistically the state $|1\chi_1, 1\chi_2\rangle_{in} = |1\chi_1^{0;3}, 1\chi_2^{0;4}\rangle$, which displays quantum interference. This effect is also known as the Hong-Ou-Mandel (HOM) interference [70, 71] and results in bunching of photons in the output modes. It can be studied by correlation measurements at different outputs $G^{(2)}_{5,6}(\delta t)$ or at one output $G^{(2)}_{6,6}(\delta t)$ in a time-resolved manner [72].

$$\begin{aligned} G^{(2)}_{5,6}(t,\delta t) =& {}_{in}\langle 1\chi_1, 1\chi_2|\hat{a}_5^\dagger(t)\hat{a}_6^\dagger(t+\delta t)\hat{a}_6(t+\delta t)\hat{a}_5(t)|1\chi_1, 1\chi_2\rangle_{in} \\ \equiv& |\langle 0|\hat{a}_5(t)\hat{a}_6(t+\delta t)|1\chi_1, 1\chi_2\rangle_{out}|^2 \\ =& \frac{1}{4}|\chi_1^0(t+\delta t)\chi_2^0(t) - \chi_1^0(t)\chi_2^0(t+\delta t)|^2 \end{aligned} \tag{2.16}$$

$$\begin{aligned} G^{(2)}_{6,6}(t,\delta t) =& {}_{in}\langle 1\chi_1, 1\chi_2|\hat{a}_6^\dagger(t)\hat{a}_6^\dagger(t+\delta t)\hat{a}_6(t+\delta t)\hat{a}_6(t)|1\chi_1, 1\chi_2\rangle_{in} \\ \equiv& |\langle 0|\hat{a}_6(t)\hat{a}_6(t+\delta t)|1\chi_1, 1\chi_2\rangle_{out}|^2 \\ =& \frac{1}{4}|\chi_1^0(t+\delta t)\chi_2^0(t) + \chi_1^0(t)\chi_2^0(t+\delta t)|^2 \end{aligned} \tag{2.17}$$

If both photons have the same carrier frequency, $G^{(2)}_{5,6}(t,\delta t)$ vanishes for all times giving rise to bunching into one output mode. It is worth to mention, that the state of the bunched photons is a superposition of two-photon Fock-states in the output modes 5 and 6 that establishes a path-entangled state [19]. If the photons possess orthogonal

polarization H and V:

$$
\begin{aligned}
&G^{(2)}_{5,6}(t,\delta t)\\
&=_{in} \langle 1\chi_{1H}, 1\chi_{2V}| \sum_{i,j} \hat{a}^{\dagger}_{5i}(t)\hat{a}^{\dagger}_{6j}(t+\delta t)\hat{a}_{6j}(t+\delta t)\hat{a}_{5i}(t)|1\chi_{1H}, 1\chi_{2V}\rangle_{in}\\
&\equiv |\left(\langle 0|\hat{a}_{5H}(t)\hat{a}_{6V}(t+\delta t) + \langle 0|\hat{a}_{5V}(t)\hat{a}_{6H}(t+\delta t)\right)|1\chi_{1H}, 1\chi_{2V}\rangle_{out}|^2\\
&= \frac{1}{4}|\chi^0_1(t+\delta t)\chi^0_2(t)|^2 + \frac{1}{4}|\chi^0_1(t)\chi^0_2(t+\delta t)|^2 \quad ,
\end{aligned}
\tag{2.18}
$$

thus the correlation displays intensities only and as expected no interference occurs.

An experiment usually integrates over a long time and samples over a large number of photons which results in the histogram patterns as:

$$G^{(2)}_{i,j}(\delta t) = \int_{\mathbb{R}} dt\, G^{(2)}_{i,j}(t,\delta t) \tag{2.19a}$$

$$G^{(2)}_{5,6}(\delta t) = \frac{1}{4\tau} e^{-|\delta t|/\tau}\left(1-\cos(\delta\omega\cdot\delta t)\right) \tag{2.19b}$$

$$G^{(2)}_{6,6}(\delta t) = \frac{1}{4\tau} e^{-|\delta t|/\tau}\left(1+\cos(\delta\omega\cdot\delta t)\right) \quad , \tag{2.19c}$$

where $\delta\omega$ denotes the carrier frequency difference of the photons.

Influence of broadening

A quantum emitter is often influenced in its emission frequency. General cases are Gaussian or Lorentzian emission frequency distributions arising from slow or fast fluctuations (here assumed to be far from leading to motional narrowing effects [49, 73]), respectively.
Assuming a Gaussian normal distribution $\mathcal{N}(\overline{\omega}, \sigma^2)$ with mean $\overline{\omega}$ and variance σ^2 as frequency jitter results in $\mathcal{N}(0, 2\sigma^2)$ for the distribution of the frequency difference $\delta\omega$, while a normalized Lorentzian $\mathcal{L}(\overline{\omega}, \Delta\omega)$ with mean $\overline{\omega}$ and full width at half maximum (FWHM)

$\Delta\omega$ results in $\mathcal{L}(0, 2\Delta\omega)$ (see appendix for the definitions). For the ensemble averages of the integrated histograms one obtains:

$$\langle G^{(2)}_{i,j}(\delta t)\rangle_{\mathcal{N}(0,2\sigma^2)} = \frac{1}{4\tau} e^{-|\delta t|/\tau} \left(1 \mp e^{-\sigma^2 \delta t^2}\right) \tag{2.20a}$$

$$\langle G^{(2)}_{i,j}(\delta t)\rangle_{\mathcal{L}(0,2\Delta\omega)} = \frac{1}{4\tau} e^{-|\delta t|/\tau} \left(1 \mp e^{-\Delta\omega|\delta t|}\right) \quad , \tag{2.20b}$$

where $\langle G^{(2)}_{i,j}(\delta t)\rangle_f = \int d(\delta\omega) f(\delta\omega) G^{(2)}_{i,j}(\delta t)$ and the minus (plus) in the brackets is to be taken for the case of different (same) output modes. Despite broadening of the emission spectrum, one can notice that coincidence at different outputs still completely vanishes for $\delta t = 0$, and hence bunching in one output mode is present. However, the oscillation pattern is averaged out to a dip in the coincidence peak. The Gaussian distribution leads to a Gaussian dip, while the Lorentzian yields an exponential dip. It is worth noting that the structure of the dip is equivalent to the damping of classical interference due to broadening when applied to Eq. (2.13) as a result of the integration over the cosine. Hence, the classical interference expresses itself in the quantum interference and allows in principle the deduction of broadened spectrum and coherence time of the emitter. However, this is challenged by detector resolution, but in particular by the Gaussian broadening which exhibits noise correlation arising from slow spectral diffusion rendering quantum interference variable over the temporal distance of the photon generation times [33, 56]. This issue is comprehensively discussed in chapter 5.

Figure 2.5a shows the different output coincidence pattern for various discrete frequency differences $\delta\omega$ in units of the Fourier-limited line width $\Delta\omega_{FL}$ (to appear as the central peak of a histogram as in Fig. 2.4). For increasing $\delta\omega$ the coalescence dip gets narrower as a result of higher oscillation frequency. Similarly, for a coincidence pattern at the same output port (Figure 2.5b), the bunching (compared to non-interfering orthogonal polarized photons) becomes increasingly narrower. Figure 2.5d shows the incorporation of broadening for the discussed cases. The coalescence and bunching features still survive and may, for a very high time resolution, allow to distin-

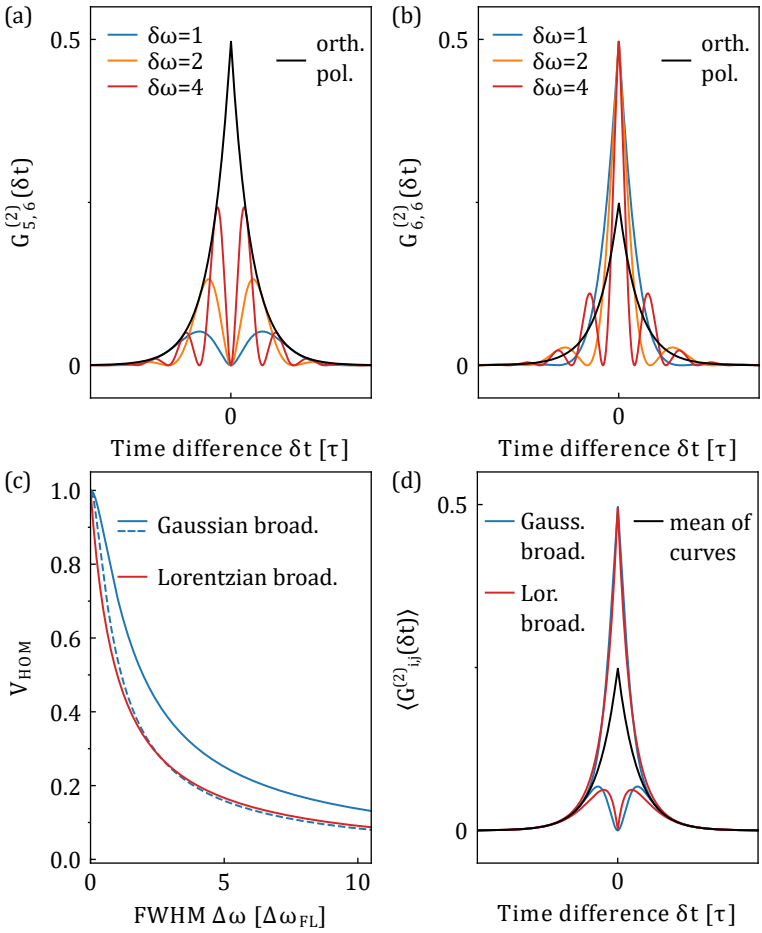

Figure 2.5. (a), Correlation of different output ports for various frequency differences $\delta\omega$ (in units $\Delta\omega_{FL} = \tau^{-1}$, the Fourier-limited line width) between the photons. Black curve is for the case of non-interfering orthogonal polarized photons. (b), Correlation at the same output port. (c), HOM visibility V_{HOM} over the FWHM (over standard deviation σ, dashed curve) for a Lorentzian and Gaussian frequency jitter. (d), Correlations for the ensemble of a broadened emission with $V_{\mathrm{HOM}} = 0.5$.

guish the underlying broadening mechanism.
In practice however, detector time resolution will limit the deduction of the interference profile in the time-resolved histogram pattern. In this case, integration over the area of coincidence and comparison to the non-interfering case of orthogonal photon polarization can be used to infer information on the emitter. Considering coincidences at different outputs, the HOM interference visibility defined as $V_{\mathrm{HOM},f} = 1 - 2\int_{\mathbb{R}} d(\delta t)\langle G^{(2)}_{5,6}(\delta t)\rangle_f$ yields:

$$V_{\mathrm{HOM},\mathcal{N}(0,2\sigma^2)} = \frac{\sqrt{\pi}}{2\sigma\tau} e^{(2\sigma\tau)^{-2}} \mathrm{erfc}\left((2\sigma\tau)^{-1}\right) \tag{2.21a}$$

$$V_{\mathrm{HOM},\mathcal{L}(0,2\Delta\omega)} = \frac{1}{1+\Delta\omega\tau} = \frac{1}{1+\frac{\Delta\omega}{\Delta\omega_{FL}}} \quad , \tag{2.21b}$$

which allows to quantify the line width of the underlying frequency distribution.
Note also, that the HOM visibility corresponds not only to the wavepacket overlap of two photons but also to the fidelity F of the two-photon state in one arm of the beam splitter to the two-photon Fock-state $|2\chi\rangle$:

$$\begin{aligned} V_{\mathrm{HOM}}(\delta\omega) &= \frac{1}{1+\delta\omega^2\tau^2} = |\langle 1\chi_1|1\chi_2\rangle|^2 \\ F = |\langle 2\chi_1|1\chi_2, 1\chi_1\rangle|^2 &= |\langle 2\chi_2|1\chi_2, 1\chi_1\rangle|^2 = |\langle 1\chi_1|1\chi_2\rangle|^2 \quad . \end{aligned} \tag{2.22}$$

The integration of Eq.(2.22) over the broadened distributions yield Eq.(2.21a) & (2.21b), respectively, thus they constitute the mean photon wavepacket overlap and the mean fidelity of the two-photon state in one output arm.

Figure 2.5c compares HOM visibilities for an emitter under the two cases of broadening. With increasing line width of the jitter $\Delta\omega$ ($=2\sqrt{2\ln(2)}\sigma$ for the Gaussian case), the visibility drops rapidly while keeping significantly higher for the Gaussian broadening at the same jitter FWHM. This is a result of the infinite variance of a Lorentzian distribution. It can be kept in mind that both curves overlap well, if the dependency over the FWHM of the Lorentzian

jitter is compared to the dependency over the standard deviation σ of the Gaussian broadening. This analogy is directly evident when coherence times (T_2) are compared.

For the simple case of a time-invariant pure dephasing process [74], its rate is $1/T_2^* = \Delta\omega/2$ and thus determines the line width of the homogeneously broadened Lorentzian jitter distribution. This results in a spectrum with total line width of $\Delta\omega_{QD} = \Delta\omega_{FL} + \Delta\omega$ where the coherence time is given through $T_2 = 2/\Delta\omega_{QD}$. Assuming purely radiative recombination of a QD transition, the decay constant of the photon is equal to the relaxation time of the two-level system, $\tau = T_1$. Thus Eq. (2.21b) leads to a connection between coherence time T_2 and HOM visibility: $V_{\mathrm{HOM},\mathcal{L}(0,2\Delta\omega)} = \frac{T_2}{2T_1}$.

For a dominantly Gaussian broadened spectrum far from being Fourier-limited, the coherence time is given through $T_2 = \frac{\sqrt{\pi}}{\sigma}$ [40]. This is comparable with the coherence time given for a Lorentzian broadening when the denominator is switched from standard deviation σ to the FWHM, and constitutes the explanation for the similarity of curves (red & dashed blue) in Fig. 2.5c.
The HOM visibility can again be expressed in terms of T_1 and T_2: $V_{\mathrm{HOM},\mathcal{N}(0,2\sigma^2)} = \frac{T_2}{2T_1} e^{(\frac{T_2}{\sqrt{\pi}2T_1})^2} \mathrm{erfc}\left(\frac{T_2}{\sqrt{\pi}2T_1}\right)$.

Chapter 3

Experimental methods

The following sections introduce the experimental methods to address single QDs and to characterize basic properties of their emission.

3.1 Photoluminescence spectroscopy of single QDs

3.1.1 Micro-photoluminescence

In this work, InGaAs QDs are excited by optical means. The subsequent emission of photons from their discrete transitions are collected and investigated in both spectral and temporal domains. The overall experimental setup is sketched in Figure 3.1.
The sample containing the QDs is glued on a piezoelectric transducer that delivers wavelength fine-tuning via the application of uniaxial strain. Both are attached with silver paste to a cold finger inside a liquid helium flow cryostat delivering $\gtrsim 4\,\mathrm{K}$ at the sample while kept in vacuum at $\sim 10^{-6}$ mbar. The optical excitation of QDs is realized through a confocal dark-field microscopy setup. The Nikon microscope objective with a numerical aperture of 0.7 and 100 x magnification is mounted on a piezoelectric transducer to allow fine tuning of the focal plane with sub-micron resolution. The in-plane positioning is realized via translation stages that move the whole cryostat and thus the sample. The excitation light of the pulsed resonant (Ti:Sa

Coherent Mira 900, operated @ 894 nm) or non-resonant (Thorlabs laser diode @ 808 nm) continuous-wave (cw) lasers are directed in reflection through a polarization beam splitter (PBS) which serves as a suppression setup for the reflected laser light from the sample. The emitted photons of the QD take the path of excitation, but partly transmit the PBS in contrast to the laser and are coupled into a single mode polarization maintaining fiber, which serves both as a spatial filter to suppress scattered laser light and to ease the guidance of photons for following investigations at different setups. Fine tuning of polarization suppression is aided by a quarter wave plate (QWP) which shall compensate polarization changes induced by optical components or the sample. An optional half wave plate (HWP) serves to rotate the optically addressed and probed axis.

3.1.2 Spectroscopy of single QDs

For the direct investigation of the QDs in the spectral domain, the aforementioned fiber is connected to a spectrometer (Figure 3.1b). A commercial PI Acton grating spectrometer with 1800 lines/mm and $\sim$ 10 GHz resolution @ 894 nm at the CCD camera is used for acquiring spectra and basic investigations of the sample. A half-wave plate (HWP) in front of the entrance slit is used to maximize the polarization sensitive diffraction. Once a certain QD is chosen for experiments, its emission is guided through a home-built transmission spectrometer. It provides high transmission ($\sim$ 80 %), negligible polarization and spatial mode distortion and with its $\sim$ 20 GHz transmission bandwidth, serves to eliminate residual scattered laser light, unwanted transitions and phonon side bands.
Such a selected transition can further be investigated in the frequency domain. A commercial polarization insensitive scanning Fabry-Pérot interferometer (FPI) [75], which consists of two plane mirrors providing a finesse of $\mathcal{F} \approx 150$ (@ 894 nm) and a free spectral range of 15 GHz, is used to capture a high-resolution photoluminescence spectrum and to resolve the line shape of the zero-phonon line of the QD emission. The histogram of transmitted and detected photons

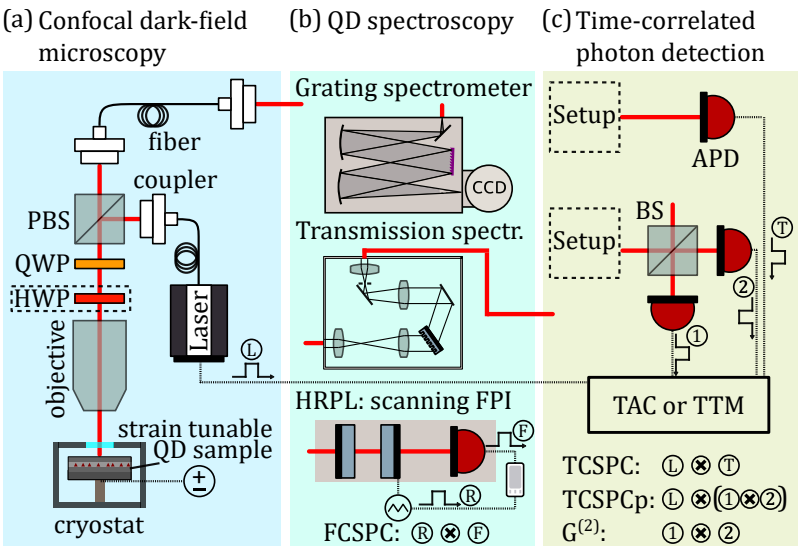

Figure 3.1. Sketch of the overall setup: (a), QDs are excited optically and their photons are collected into a polarization maintaining single-mode fiber. (b) QDs emission is investigated in the frequency domain with a grating spectrometer for coarse spectrum and a scanning Fabry-Pérot interferometer is used for high resolution photoluminescence (HRPL). For further experiments, the emission is guided through a transmission spectrometer that serves as a monochromator. (c) Photons propagate through further experimental setup and are detected via APDs. Electronic signals are correlated via TAC or TTM delivering time resolved measurements.

(at a silicon-based Perkin Elmer avalanche photo diode (APD)) is evaluated with a multi-channel buffer over the position of the mirror displacement, which is triggered by the piezoelectric transducer ramp to provide the frequency information. For that, in the following, this measurement will be referred to as frequency-correlated single-photon counting (FCSPC).

Furthermore, this setup is used to fine tune the QDs emission wave-

length to the Cs-D_1 transitions. For that, its spectrum is referenced and compared to the spectrum of a single mode cw laser resonant to the Cs transition. It shall be noted, that a calibration of the absolute frequency reference of the scanning FPI must be updated over time due to a slow drift. Figure 3.2c shows such a spectrum of a DL Pro cw laser which constitutes the instrumental response of the FPI and references the target frequency.

3.2 Time-correlated photon detection

For the time-correlated detection of single QD photons, two fiber coupled APDs are used, which signal the detection of a photon via an electric pulse. For these measurements, the resonance florescence is first filtered via the aforementioned transmission spectrometer. The time correlation is triggered by the electrical pulse of a fast internal diode of the excitation laser, as depicted in Figure 3.1. A histogram of APD clicks over their detection time difference to the laser trigger is referred to as time-correlated single-photon counting (TCSPC).

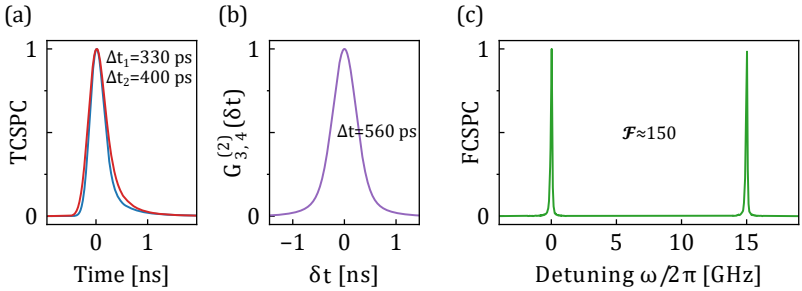

Figure 3.2. Measured instrumental system responses and FWHMs Δt. (a), TCSPC of the attenuated pulsed laser ($\sim 3\,\mathrm{ps}$) at the two APDs utilized in the time correlated measurements. (b), Correlation of the pulsed laser after the different outputs of a beam splitter. (c), FCSPC of a single-mode cw laser at a scanning Fabry-Pérot interferometer of finesse $\mathcal{F}$.

It delivers the time resolved intensity profile $|\chi(t)|^2$ of photons. A histogram of APD1 clicks triggered by APD2 clicks at different outputs of a beam splitter over their detection time difference delivers the second-order coherence $G^{(2)}$. Depending on the setup prior to the beam splitter, it can serve various purposes. For instance, when the emission is just directed on a beam splitter, the correlation is used to investigate the photon statistics; in our case to proof the single-photon nature of the emission via absence of coincidence. Alternatively, using the beam splitter as part of an unbalanced MZI (see section 2.3.2), the $G^{(2)}$ serves to investigate HOM interference and as a novel method, following a dispersive medium the $G^{(2)}$ is exploited to investigate the dynamics of spectral diffusion (see chapter 5).
The time difference between APD detections is determined using a time-to-amplitude converter (TAC) which starts a voltage ramp with the electronic pulse of an APD click to stop the ramp with the click of the other APD or laser trigger, depending on the measurement. The final value of the voltage is sorted by a multi-channel analyzer that delivers the time difference after being calibrated by the known laser repetition rate. In parts of the measurements a time-tagging module (TTM) was available (Pico Quant and Swabian Instruments), which marks time stamps for the electronic triggers of all detectors simultaneously to allow post-processed correlations among all detection signals. In particular, in this way time-correlated single-photon counting under postselection (TCSPCp) can be realized, which correlates laser trigger to an APD signal only if a coincidence of APD clicks occurred in a certain time window. TCSPCp probes photon pairs in contrast to single photons in TCSPC.

Figure 3.2a and b show TCSPC and $G^{(2)}$ for attenuated, close to Gaussian laser pulses of $\sim 3\,\mathrm{ps}$ duration. These measurements probe the total timing jitter of the correlation electronics, thus represent the system response. TCSPC displays an asymmetric response fitting to a split-Voigt profile of 330 ps (400 ps) FWHM due to after pulsing, while the jitter of the $G^{(2)}$ is a single Voigt profile with 560 ps FWHM. Note, that all theoretical curves in this thesis that are drawn on top of data incorporate these measured responses.

Chapter 4

Building blocks of the QD-Cs vapor interface

4.1 The single-photon source: Single InGaAs QDs

Single semiconductor QDs have been established as quantum emitters with the potential to fulfill the portfolio of requirements posed on a perfect source for quantum technological applications [8]. For on-demand operation, the deterministic inversion of a two-level system is crucial as well as the subsequent emission of light into a single temporal, polarization and spatial mode. To benefit from the quantum aspect, the emission needs to be purely in the one-photon Fock-state $|1\rangle$ in both the photon number basis and its spectral composition.

In the following, basic optical and quantum optical properties of the emission of single InGaAs QDs of the considered sample are investigated and compared to the aforementioned portfolio. In particular, the identification of the desired charged exciton state is shown, and its emission is investigated with regard to on-demand operation and quantum-state purity.

4.1.1 Identification of CX in the spectrum of a QD

The investigated sample consists of a single layer of self-assembled In(Ga)As quantum dots grown by MOVPE. The quantum dot layer is sandwiched between GaAs/AlAs distributed Bragg reflector layers at the center of a GaAs λ-cavity. This planar sample structure already accelerates optical transitions by a factor of two compared to a bare sample ($\sim 1\,\mathrm{ns}$) and supports directional emission. Based on detection rate and a rough estimate of overall setup transmission, $\sim 1-10\%$ efficiency for a single spatial mode into the collection path is indicated. While this design cannot claim to satisfy high collection efficiency demands, the ease of its fabrication is advantageous for basic research.

It was already argued, that among basic QD transitions, the charged exciton (CX) transition of a QD recombines at a single energy due to absence of line splitting, which is why it is suitable for interconnecting hybrid quantum systems. This work therefore focuses on charged excitons; as a first step its identification by specific characteristics is presented.

A micro-photoluminescence spectroscopy setup allows to investigate the basic emission properties of QDs. A typical florescence spectrum of a single QD (which will be referred to as QD B) is depicted in Fig. 4.1a. Under non-resonant pumping well below saturation, the QD spectrum mainly contains discrete lines from electron-hole recombination of its lowest states ($s-$shell). These transitions are the exciton (X) which is a recombination that occurs when the QD confines one electron and one hole, the CX transition where an additional charge carrier resides in the QD and the biexciton (XX) transition where the recombination occurs while two electron and two holes occupy the lowest state, respectively. Due to occupation probabilities, typically the X line appears to be the brightest, while the XX line is the dimmest. However, in general a (unintentional) background doping can influence the occupation probabilities, thus power and polarization dependent measurements are necessary to unambiguously

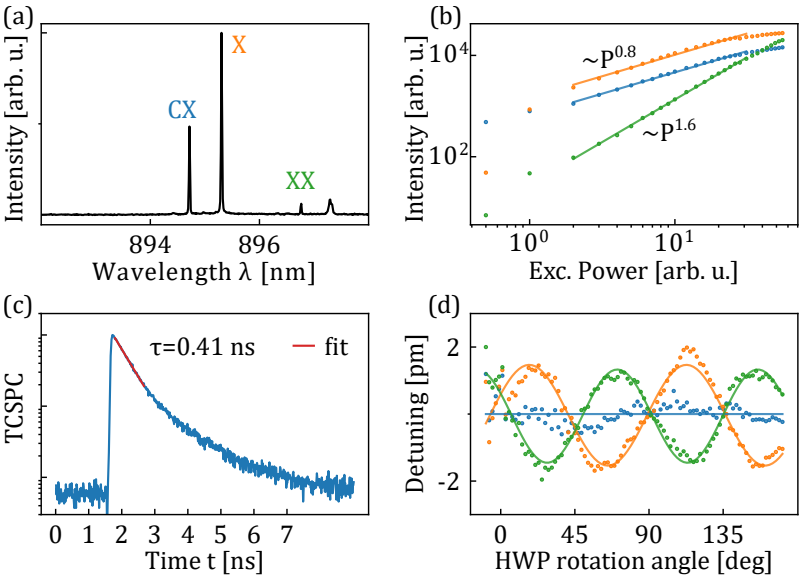

Figure 4.1. (a), The emission spectrum of QD B under non-resonant excitation well below saturation. Lines are assigned to charged exciton (CX), exciton (X) and biexciton (XX). The same color code for all graphs. (b), Non-resonant excitation power (P) dependence of emission lines. (c), Time-correlated single photon counting of CX under resonant excitation. The decay constant τ is obtained by an exponential fit. (d), Polarization dependence of the detuning of respective emission line centers.

assign the lines of the spectrum to specific states of the QD.

Fig. 4.1b shows the intensity of the lines as the non-resonant laser power is increased. The QD transitions that result from a single pair of charge carriers, X and CX, are expected to scale linearly with the excitation power, while the state XX which relies on two pairs is expected to scale quadratically. Indeed, below saturation an approximately linear dependence of emission rates on the power $P^{0.8}$ is observed for X and CX, while XX scales exactly quadratically to

the single pair states with $P^{1.6}$. This leads at higher powers to XX count rates well above the CX rates. While the recombination of CX leaves a single charge carrier in the QD, the recombination of XX most likely leads to the cascaded emission of an X transition, which is why X saturates at higher intensities than XX.

In general, multiple QDs can be located within the spot size of the microscope objective. To lift any ambiguity that may occur as a result of overlapping lines of different QDs, the special polarization dependence of X in contrast to CX can be used. For elliptically shaped QDs, the two linearly polarized transitions (parallel to the spatial QD axes) of X are non-degenerate and can be identified in polarization dependent spectra. For that, the angle of the half wave plate (HWP) in front of the PBS in the collection path is rotated, while the center of the emission lines are recorded. Fig. 4.1d shows the detuning of the respective transitions with the angle of rotation of the HWP and allows final assignment of the lines. CX shows no dependence of its line center to the analyzed linear polarization as a result of its circularly polarized emission. In contrast, X and XX show a sinusoidal dependence but with a phase shift of 45°, i.e. maxima are reached for orthogonal polarization of analysis. This behavior is related to the fine-structure splitting due to the in-plane anisotropy of the QD [76] and amounts to $\Delta E_{\mathrm{FSS}} \sim 5\,\mu\mathrm{eV}$.

Alternatively, time-correlated single photon counting (TCSPC) after pulsed resonant excitation can be performed to distinguish between X and CX lines. In case of X with a fine-structure splitting, the coherent excitation of both lines yields a sinusoidal oscillation in TCSPC when analyzed in linear polarization. Its absence proves CX as the addressed transition. Fig. 4.1c shows TCSPC of the CX which reveals once again the absence of a polarization dependent line-splitting. Notably, the detected photons show a sharp rising edge and a mono-exponential decay (after accounting for the APD after pulsing) as expected from the spontaneous emission of a two-level system. Besides the absence of a line-splitting, this precise timing of the photon emission in resonant excitation makes the CX most attractive for interfacing with another two-level system and on-demand operation.

4.1.2 On-demand single-photon generation

Although non-resonant excitation constitutes a comfortable way for basic QD characterization, it is obvious that uncontrolled QD state preparation can not yield high photon generation rates of a single transition. Moreover it comes along with various dephasing mechanisms, most significantly timing jitter and enhanced line broadening which diminish quantum optical properties [49,77]. Fortunately, QDs allow excitation into higher states, phonon-assisted and resonant excitation of their transitions. The latter approach is used here which is a promising scheme to push QD emission to its best performance [8,25].

On-demand operation

Ideal inversion of a two-level system can theoretically be achieved by driving with a resonant laser field. Depending on the product of the dipole moment μ, driving field amplitude $\varepsilon(t)$ and interaction time, a superposition of ground and excited state is created. The sinusoidal evolution of excited state population is referred to as Rabi oscillations [64]. When the pulse area $\Theta = \mu/\hbar \int \varepsilon(t)dt = \pi$, an undamped system would result in unity occupation probability of the excited state. To estimate the inversion fidelity of the CX transition of a QD, the coherence of the two-level system is probed by increasing the power of a resonant pulsed laser where the pulse duration ($\sim 3\,\mathrm{ps}$) is fixed. Fig. 4.2c shows the pulse area dependent resonance florescence which is proportional to the excited state population probability. With increasing pulse area the intensity of CX emission increases linearly to continue a damped oscillation after the maximum at $\Theta = \pi$. The adjustment of excitation power to the value which delivers the maximum of resonance florescence intensity is referred to as π-pulse excitation ($\sim 250\,\mathrm{nW}/\mu\mathrm{m}^2$).
To extract the maximum excited state preparation probability, optical Bloch equations of a two-level system with a power dependent dephasing term are numerically solved according to the model in [78]. For the present data, the CX preparation fidelity of ~ 0.75 is found at the π-pulse. The damping of Rabi oscillations reveals a strong impact

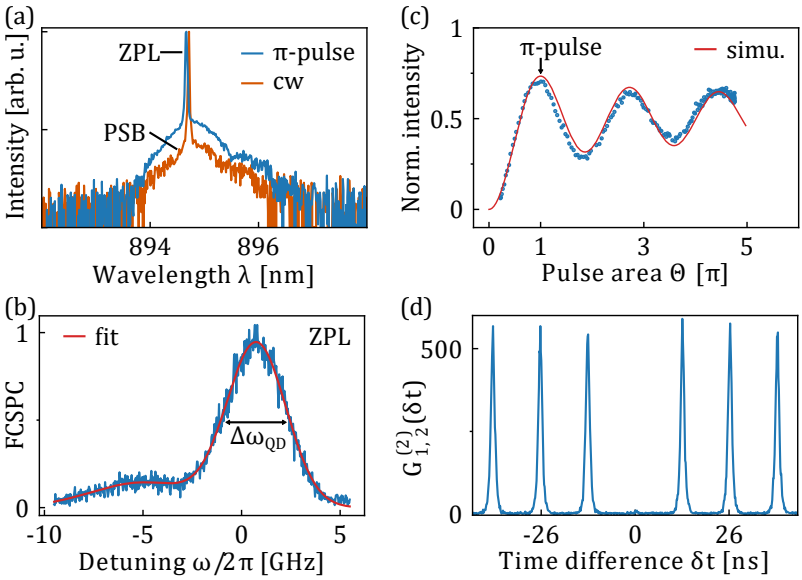

Figure 4.2. (a), Logarithmic plot of the emission spectrum of QD A under resonant cw or the π-pulse excitation of its charged exciton. The maximum strain tuning is applied in the latter case. Zero-phonon line (ZPL) and phonon side bands (PSB) are indicated. (b), High-resolution spectrum of the filtered ZPL under π-pulse excitation. Gaussian fit yields a QD line width of $\Delta\omega_{QD}/2\pi = 3.5\,\mathrm{GHz}$. (c), Rabi rotations of the ZPL. Pulse area $\Theta \propto \sqrt{P}$ is increased by increasing excitation power P of the pulsed resonant laser. A simulation of excited state population is fitted to the data. (d), Second-order coherence of the ZPL under the π-pulse excitation.

of phonon-induced dephasing which is known to be the main cause of damping and reduction of excited state preparation probability in QDs [79, 80].

Recently, pulse area dependent studies showed a rich dynamics of QD emission [51, 81]. One interesting regime is the emission of a QD excited below the π-pulse. Here, the coherent preparation of a

superposition of ground and excited state of the CX is mapped on to an emitted superposition of vacuum and one-photon Fock-state. Surprisingly, at the various minima of the Rabi oscillations, multi-photon emission dominates the photon statistics while the time domain deviates strongly from a mono-exponential decay. The studies further suggest a finite but negligible probability for multi-photon emission at the π-pulse. Nevertheless, the latter case constitutes the operation point for yielding highest photon rates and has been favored for QD-based quantum implementations [16, 19, 27].

For on-demand operation of a quantum emitter, besides deterministic excitation, the spectral mode of emission is a crucial figure of merit. Solid-state quantum emitters couple strongly to the crystal lattice of the host material. For that reason, their emission contains not only the transition of the two-level system, the zero-phonon line (ZPL), but also the so called phonon side bands (PSB). In QDs, the PSB amounts to less than 10% of the total emission in resonance florescence and is independent of the resonant excitation power [82, 83]. This fraction is significantly lower than for other quantum emitter like nitrogen vacancy centers [84], but still poses a fundamental limitation to the useful photons. However, by coupling (weak coupling regime) the relevant QD transition to a narrow bandwidth micro-cavity, the fraction emitted into the PSB can further be decreased [85].

To evaluate the PSB for the QDs of the present sample, Fig. 4.2a depicts exemplarily the total CX emission spectrum of QD A under π-pulse excitation in comparison to its resonant cw excitation. The ZPL appears as a bright discrete line, while the PSB ranges over a few nm. The PSB is asymmetric which reflects the higher probability to release energy via phonon interaction at cryogenic temperatures. The area under the broad feature of the spectrum amounts to $\sim 38\%$ of the total emission when the π-pulse excitation is utilized. In contrast, cw excitation yields $\sim 22\%$ for the broad feature. While in the latter case, the broad bands reflect the actual PSB, the apparent higher fraction in the pulsed excitation is most likely a result of imperfect laser suppression. The short broad bandwidth excitation pulse covers a similar spectrum as the PSB prohibiting a clear assign-

ment. However, even when the lower value is taken as the PSB, the fraction is much higher than reported for high performance samples in literature, suggesting that the temperature at the sample may be higher than the anticipated 4 K due to attachment of the sample to the cold finger via a piezo transducer. This would also explain the relatively strong reduction of CX state preparation fidelity due to coupling to acoustic phonons.
Conclusively, the on-demand operation by driving a CX at the π-pulse achieves an efficiency of $0.75 \times 0.78 \approx 0.59$ into the ZPL, when the polarization suppression setup is not accounted for. Indeed, alternative schemes, e.g. coherent dichromatic excitation can circumvent the polarization suppression thereby approaching the fundamental limits imposed only by the driving and emission properties of the QD transition [86].

Other aspects that may be specific to the present sample have to be mentioned with regard to on-demand operation. It should be noted, that while the fraction emitted into the PSB under resonant π-pulse pumping appears reproducible from dot-to-dot, the visibility of Rabi oscillations varies significantly not only from dot-to-dot, but also on daily basis on the very same QD. The actual dynamics of a QD is much more complex than a simple two-level system and specific to the QD and its environment, which may reconfigure at the daily cooling cycles.
Furthermore, despite the resonant pumping of the CX line, many QDs show in addition unwanted X recombination that most likely is a result of an Auger process or tunneling [87,88] that further quenches CX emission rate. The small fraction of these excitons $\sim 1 - 10\%$ is generally also subjected to daily changes and show a strong dependence on an additional weak ($< 10\,\mathrm{nW}/\mu\mathrm{m}^2$) cw non-resonant laser. The extracted maximum occupation probability of the CX therefore has to be understood rather as an estimation.
However, it should be pointed out, that the high-resolution spectrum of the ZPL, its photon statistics and quantum interference visibility, which are studied in the following, are stable properties of a QD that are preserved over any number of cooling cycles of the sample.

Photon statistics of a QD emission

Photon statistics of the QD emission is performed by directing it onto a beam splitter and the measurement of the second-order coherence $G^{(2)}_{1,2}$ at the output ports (1 & 2) [39]. Depending on the value of the central coincidence peak, the emission can be classified. In case of pure single quanta, a coincidence detection will never occur.
Fig. 4.2d shows the correlation histogram for the ZPL of QD A (see Fig. 4.2c). Correlations are present at the repetition times of the excitation pulse ($t_{rep} = 13.1\,\mathrm{ns}$), while simultaneous coincidences are strongly suppressed. The normalized value amounts to $g^{(2)}_{1,2}(0) = 0.015 \pm 0.005$ proving excellent fidelity to the one-photon Fock-state of the emission under π-pulse excitation. The finite value contains contributions of emission and re-excitation during the excitation pulse, but can mainly be considered as the result of imperfect laser suppression ($\sim 10^4$ laser photons are needed for the excitation of a single QD transition). Having proven excellent purity in the photon number basis, in the next step purity in the wavepacket basis is investigated.

4.1.3 Two-photon interference

Two-photon interference at a beam splitter is a basic building block of many quantum technological applications. For example, the Bell-state measurement in a quantum repeater [13] and in linear optical quantum computing [15] or N00N-state generation for quantum enhanced sensing [89] rely on this effect. In case of bosonic single photon inputs, it is also referred to as Hong-Ou-Mandel (HOM) interference [70] which results in both bunching of photons into the same output mode and entanglement of outputs. Traditionally this is measured by the absence of coincidence detection. This effect is not limited to optical wavepackets but can also be observed with i.e. phonons [90] and even atoms [91] by suitable mode splitting operations on initial modes that induce an overlap of the two following trajectories.

Using single photon emitters, HOM interference visibility is a measure of mode overlap between the two interfering photons. In our case of resonantly excited CX transitions, the temporal mode is exactly determined, such that an unbalanced Mach-Zehnder interferometer can be used to bring successively emitted photons to overlap at the output beam splitter. The classical interference of a laser can be used to align spatial modes perfectly. When the photons are furthermore prepared in identical polarization mode, the interference visibility and temporal dependence of correlations after the beam splitter are only determined by the spectral properties of the photons (see chapter 2 and [72,92]). Thus, HOM interference constitutes not only a method for entangling operations but also to probe broadening of the emission line. As such, it is the basic tool to characterize quantum emitters for their performances in multi-photon quantum implementations, as it crucially determines the fidelity of quantum gates that rely on quantum interference at a beam splitter.

However, since the first realization of HOM with QD photons [71], a discrepancy of HOM visibility and the independently measured coherence time via Fourier spectroscopy is known. The presence of a slow spectral diffusion process of the QD has been suggested which is not probed by the interference of successively emitted photons that are typically apart by a few nanoseconds. Indeed, HOM interference has been shown to reduce with the distance of emission time difference of interfered photons [93–95]. However, synchronization of photons at the beam splitter by delaying the preceding one has been limited to 15 μs, thus the independently measured coherence time or stationary spectrum of the emitter could not be reproduced. Noise spectroscopy in fact suggests spectral diffusion ranging to milliseconds and beyond [52,53]. A solution to this issue is provided in this work, being addressed in the next chapter [56]. While active and passive schemes to control spectral diffusion can be exploited to reduce the dephasing [33], alongside with high quality sample growth, high Purcell enhanced acceleration of radiative recombination in micro-cavity structures under resonant excitation turns out to be most effective to achieve near unity HOM interference visibility [28,77,96].

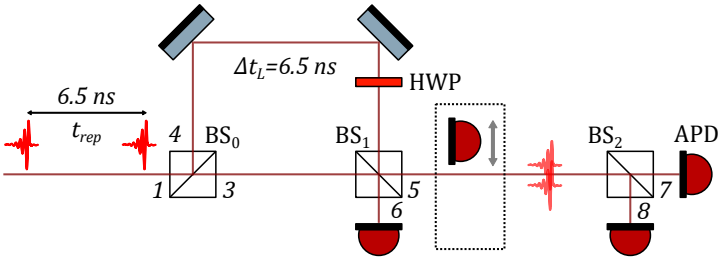

Figure 4.3. Experimental setup to perform HOM interference of successive photons at BS_1. The time difference given by the excitation laser repetition period t_{rep} is compensated for in the unbalanced MZI. The HWP serves to align the photon polarization parallel or perpendicular to each other. Successful interference directs both photons into one output. This is measured by second-order coherence at ports (5 & 6) or through correlations after BS_2 at output ports (7 & 8).

Here, the HOM interference of QD A is studied under resonant π-pulse excitation of the CX state, while both anti-correlation at the outputs and bunching into one output port are investigated.

HOM interference of successive QD photons

The experimental setup to realize HOM two-photon interference of successively emitted QD photons is shown in Fig. 4.3. The ZPL of the emission of a QD under resonant π-pulse excitation is directed into a HOM setup with the doubled laser repetition period of $t_{rep} = 6.5\,\text{ns}$. The unbalanced MZI compensates for the time difference, so that successively emitted photons can impinge on BS_1 simultaneously to interfere. Successful interference of indistinguishable single photon wavepackets $|1\chi^{0;3}\rangle$ (see Eq. (2.12)) from port 3 and $|1\chi^{L;4}\rangle$ from port 4 results in $\frac{1}{\sqrt{2}}(|2\chi^{0;5}, 0\chi^{0;6}\rangle + |0\chi^{0;5}, 2\chi^{0;6}\rangle)$.

This section is reproduced in parts from:
H. Vural et al., PRB **103**, 195304 (2021) ©2021 American Physical Society

This state exhibits path-entanglement and the conversion of one-photon Fock-states into two-photon Fock-states, and is referred to as a N00N-state (here for N=2). In contrast to completely distinguishable photons which exhibit 1/4 probability to create the classically possible output formations, the N00N-state will show no coincidences $G^{(2)}_{5,6}(0)$ when measured at output ports (5 & 6). The deviation under the consideration of line broadening is discussed in chapter 2. Alternatively, directing one output port to an additional beam splitter BS_2, 2002-state formation is testified by doubled coincidences for correlation $G^{(2)}_{7,8}$, which serves as a pseudo-photon number resolving detector. While indistinguishable photons generate a two-photon Fock-state $|2\chi^{0;5}\rangle$ in the output mode 5 in half of the cases, distinguishable photons propagate as a pair only in a quarter of cases. The exact temporally resolved behavior under line broadening is discussed in chapter 2.

Fig. 4.4a shows the HOM interference as traditionally measured after BS_1 for both parallel and perpendicular polarized inputs. Due to the possible paths consecutive photons can take in the HOM setup, a peak pattern arises where only the central coincidence peak consists of the photons entering at the beam splitter simultaneously from different ports (3 & 4). When perpendicularly polarized, i.e. non-interfering photons are considered (orange curves), the central coincidence peak amounts to half of the outermost peaks which relate to the Poissonian level. For the parallel polarized case (blue curves), a strong reduction of coincidences is found. Moreover, a dip is indicated, which in case of a jitter-free detector would reach zero. The coalescence reveals indistinguishability of successive photons [71], while the still present modulated peak reveals broadening of the emission line [72, 92]. By a fit to the data, the areas under the coincidence peaks deliver the HOM interference visibility $V_{\mathrm{HOM}} = 1 - G^{(2)}_{5,6\parallel}/G^{(2)}_{5,6\perp} = 0.53 \pm 0.03$. Moreover, a coherence time $T_2 \approx T_1 = 0.43\,\mathrm{ns}$ and a corresponding line broadening of $\Delta\omega = 0.9\,\mathrm{GHz}$ is revealed when the frequency jitter is assumed to be a Gaussian distribution. This assumption is motivated by the

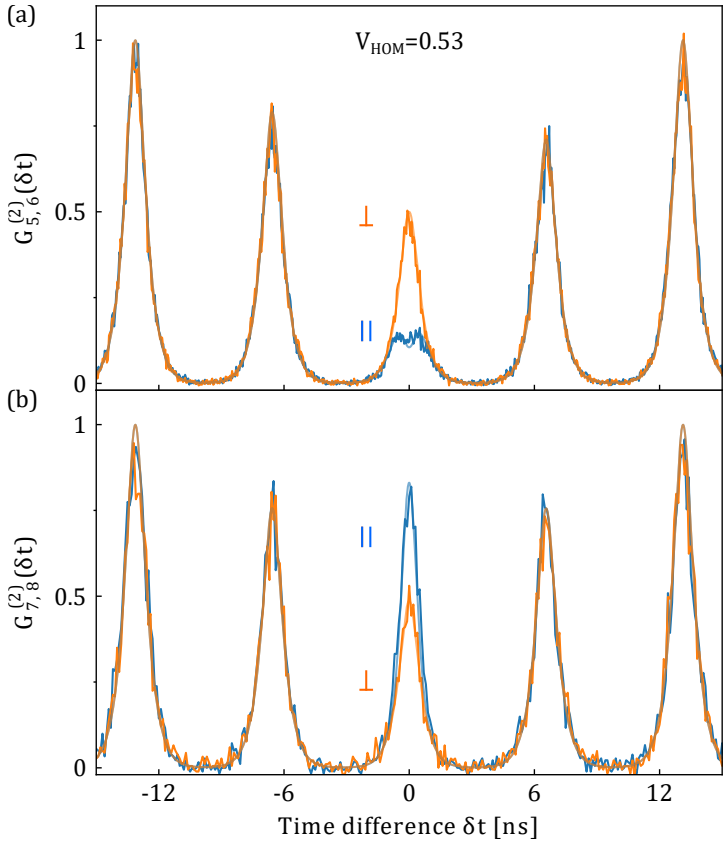

Figure 4.4. (a), Second-order coherence at the output ports of BS_1 to probe HOM interference for parallel (‖) and perpendicular (⊥) photon inputs. Light solid lines on top of data are theory curves. (b), Second-order coherence at the output ports of BS_2 to reveal photon-correlation after the HOM interferometer output port 5.

Gaussian broadening of the ZPL, as shown in Fig. 4.2b. However $\Delta\omega$ appears much narrower than the main emission line of the QD with its $\Delta\omega_{QD} = 3.5\,\mathrm{GHz}$ FWHM. This is a clear indication of the presence of a spectral diffusion process that is significantly slower than the probed timescale (6.5 ns). On the other hand, the only moderate HOM visibility points towards a strong influence of phonon dephasing and a higher temperature than the expected 4 K [54], as was also indicated in the relatively large fraction of the QD's PSB (Fig. 4.2a).

To study the possible impact of excitation pulse power on the visibility, the HOM experiment was repeated at $\Theta = \pi/2$ and the two other maxima of the Rabi oscillations at $\Theta \approx 3\pi$ and $\Theta \approx 5\pi$ (see Fig. 4.2c). The HOM visibility is found to be preserved, indicating that excitation power does not add any notable dephasing upon the already existing one.

The observed coalescence in the HOM experiment implies both preparation of the two photon N00N-state with a fidelity of 53% [19] and consequent bunching of photons in one output port which is now inspected in the central coincidence peak of the correlation $G^{(2)}_{7,8}$ (see Fig. 4.4b). The case of perpendicular polarized photons reproduces the previous pattern with the central peak reaching half the Poissonian level. Note that the signal-to-noise ratio decreases due to reduction of detected rates as photons in output 6 do not contribute anymore. For parallel polarized photons the central peak displays a strong increase of coincidences as opposed to the previously observed reduction. Notably, the visibility reproduces the value of the previous HOM measurement proving the equivalence of both detection schemes. Moreover, this demonstrates the successful propagation of two-photon Fock-states between the two beam splitters of spatial mode 5 again with a fidelity of 53% (see Eq.(2.22)). This scheme does not only constitute a complementary measurement to the HOM experiment, moreover, it will serve to study the interaction of two-photon states with atoms in the next chapter.

4.1.4 Peculiarities of the sample

Although there is room for improvement to fulfill the portfolio of requirements posed on a perfect quantum emitter, the QDs of the investigated sample possess firm quantum optical properties that make them suitable for basic research. In particular, the purity of single-photon emission under resonant π-pulse excitation is excellent for all studied QDs, qualifying them for instance to realize secure quantum key distribution [97]. However, HOM interference visibility, which reflects the indistinguishability of successively emitted photons, shows moderate values that range randomly from 0.35 to 0.53. Especially, there is no correlation of visibility to neither the brightness of QD emission nor the line width of its ZPL. The measured HOM visibilities correspond to frequency jitter that amount to only a fraction of the total emission spectra, strongly indicating line broadening mechanisms beyond the nanosecond timescale.

It should be noted, that the ZPL often consists of more than a single line, with randomly varying detuning to each other and respective amplitudes, although the spectra of CX should not display a line-splitting. Indeed, the occurrence of complex spectra consisting of multiple lines has been attributed to quantum confined Stark-shifts of charge carriers trapped in the QD's vicinity [48].

The majority of QDs necessitate the assistance of a weak non-resonant laser to be resonantly addressable in their CX states. Depending on the wavelength [98] and power [99] of the non-resonant laser, the QDs charge state can be manipulated and set properly to realize resonant excitation. Although clear Rabi oscillations can be observed for all the majority of QDs, due to the non-deterministic charge state preparation as well as emission of X instead of CX, the extracted fidelities of excited state populations often remain questionable. In particular, due to daily changes of the coherent excitation, QD Rabi oscillations can show a drastic reduction of visibility pointing towards a complicated interaction with its environment. Remarkably, the HOM visibility remains unaffected by these changes, indicating the origin of Rabi dephasing not to be connected to the

photonic coherence of the two-level system but in Auger or tunneling processes.

The investigated QDs have been chosen to emit their CX lines very close to the Cs-D_1 transition. In an area of the sample with a QD density below $\sim 1/\mu m^2$, to find a suitable candidate necessitated a scan over an area of $50 \times 50\,\mu m^2$. This subset of QDs of the sample showed often very similar spectra with $\Delta E_{\text{CX-X}} \approx 0.9\,\text{meV}$ and $\Delta E_{\text{X-XX}} \approx 2.2\,\text{meV}$, such that a few spectra were not distinguishable even in non-resonant excitation, which is known as the fingerprint of a QD. Identification had to rely in these cases on neighboring QDs or the high-resolution spectrum of the ZPL.

The strain-field applied to the sample allows a tuning range of $\Delta E/h \approx 20\,\text{GHz}$ which covers the total range of the hyperfine-split Cs-D_1 lines, thus being helpful to fine-tune the CX wavelengths. For the investigated QDs, the uniaxial strain field resulted only in a red tuning, which is a result of several dependencies like QD material composition, its shape, potential and strength of applied stress [100]. In principle, the tuning range can reach over a THz [101], when stress is effectively translated to the QD's location.

Most crucially, strain-tuning preserves the emission quality, as is validated for the investigated QDs by unchanged HOM visibilities. In contrast, a similar tuning range provided by heating the sample to a nominal temperature of $\sim 20\,\text{K}$ results in a drop of visibility from ~ 0.5 to ~ 0.15. This underlines the clear benefit of the strain-tuning mechanism despite the present small tuning range.

4.2 Dispersive medium: hot Cs vapor

The counterpart of QDs are Cs atoms in vapor phase. The emitted photons of CX transitions will be interacting with the Cs vapor in a glass cell of length $L_V = 10\,\text{cm}$ or $L_V = 25\,\text{cm}$. As the interaction is linear, the transmission spectrum of the vapor contains all relevant information, since the absorption can be used to deduce the dispersive properties via the Kramers-Kronig relation.

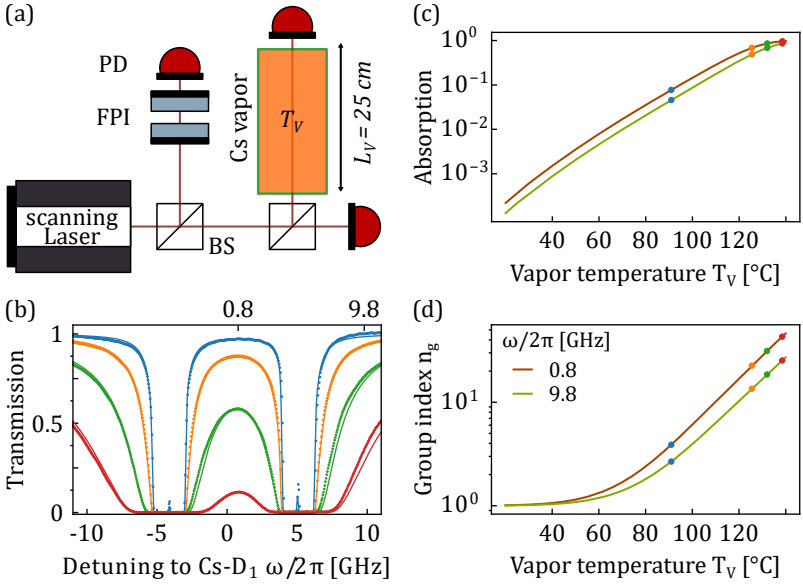

Figure 4.5. (a), Experimental setup to perform transmission spectroscopy of hot Cs vapor. Detectors are photo diodes (PD). Fabry-Pérot interferometer (FPI) serves for linearization of frequency axis.(b) Transmission spectra of a Cs vapor of length L_V at the temperatures $T_V = 75.8\,°C$, $96.3\,°C$, $115.2\,°C$ and $132.7\,°C$. Dots represent data and solid lines are theory curves. Color code applies for the whole figure. (c) Logarithmic plot of vapor absorption at two particular detunings. (d) Logarithmic plot of group index. Legend applies also to (c).

Fig. 4.5a depicts the experimental setup to perform transmission spectroscopy of Cs vapor at various vapor temperatures T_V. The linearly polarized scanning cw laser is split in three parts. One part is used to calibrate the frequency axis of the scanning laser by the transmission profile of a Fabry-Pérot interferometer, one part is used to acquire the continuously changing laser intensity over the scan frequency for calibration, and a last part is send through the vapor

to detect its transmission profile.
Fig. 4.5b shows the transmission spectrum at various temperatures which have been nominally set to $T_{V,\mathrm{set}} = 80\,^{\circ}\mathrm{C}$, $100\,^{\circ}\mathrm{C}$, $120\,^{\circ}\mathrm{C}$ and $140\,^{\circ}\mathrm{C}$. Even at the lowest investigated temperature, the transmission profile of neighboring (excited state hyperfine-splitted) transitions tend to merge due to strong Doppler-broadening of the various velocity classes of atoms within the vapor. With increasing temperature its impact strengthen to form a bell-shaped transmission window between the fully absorbing broadened lines. From the comparison to the theoretical fits of ElecSus [62] the actual vapor temperature, which lie slightly below the set temperatures, can be deduced to $T_V = 75.8\,^{\circ}\mathrm{C}$, $96.3\,^{\circ}\mathrm{C}$, $115.2\,^{\circ}\mathrm{C}$ and $132.7\,^{\circ}\mathrm{C}$. Note that, due to strong linear increase of laser intensity over the scan frequency, the weak probe limit (laser intensity$I_L \ll I_{\mathrm{sat}} = 25\,\mu\mathrm{W/mm^2}$, the saturation intensity of Cs D_1 line [64]) of the theoretical framework is not fulfilled over the full scan range. This is reflected in slight deviation of theory and data. In case of single photons however, the weak probe limit is fully valid, such that theory curves of the vapor response from ElecSus can be used for simulations.

For two particular detunings which play a role in the next chapter, the dependencies of absorption and group index over the vapor temperature is investigated. At detuning $\omega/2\pi = 0.8\,\mathrm{GHz}$, the maximum of the transmission window as well as at its wing $\omega/2\pi = 9.8\,\mathrm{GHz}$, the absorption has an exponential increase up to close to total absorption (Fig. 4.5c). This is a consequence of the strong temperature dependence of the atomic density in the vapor phase, as well as the strength of atom-light interaction cross section which is influenced by the Doppler width [102].
For the group index n_g, which constitutes an important figure of merit of the slow-light effect, again an exponential dependence at both detunings is found in the experimentally investigated temperature range, since it depends approximately linearly to the absorption coefficient [103]. The higher absorption at detuning $\omega/2\pi = 0.8\,\mathrm{GHz}$ in comparison to $\omega/2\pi = 9.8\,\mathrm{GHz}$ results in significantly higher group index. Note, that n_g is independent of the vapor cell length. The

following experiments will be mainly performed at group indices between 10 to 50 to reach a significant delay for the QD photons within the vapor cells.

Chapter 5

QD-Cs vapor interface

In the following, the first section introduces the concept of time domain spectroscopy enabled by the slow-light medium, which is based on the mapping of frequency domain onto time domain. After a theoretical investigation which takes line broadening into account, the technique is demonstrated for the emission of QDs under the on-demand operation at the π-pulse.

Based on this working principle, a novel photon-correlation technique is established in the next section, that allows the study of spectral diffusion dynamics of on-demand operated QDs. The theoretical description of a suitable model is followed by experimental results and quantification of line broadening for the investigated QDs.

In the third section, quantum states of light are investigated while using the medium as a variable delay line. The propagation of one and two-photon Fock-states in the dispersive medium are experimentally validated.

Finally, we explore the impact of Cs vapor-single photon interaction and resulting pulse distortion on the quantum optical properties of transmitted photons via HOM two-photon interference measurements in two vapor constellations, which allow to outline the potential of this interface for real-world applications.

5.1 High-resolution spectroscopy enabled by the slow-light effect

The obvious benefit of the slow-light effect is to induce a temporal delay for optical pulses [60, 104–106]. In this case, the signal at the output of the delay line is desired to be identical with the input. However, using the slow-light effect is not restricted to a delay line. Quite contrary, various applications make use of it [60], even benefit from the unwanted pulse distortion. For instance, the pulse length compression [107] within the slow-light medium increases energy density and enhances light-matter interaction [108]. Besides that, utilizing a slow-light medium in phase measurements and interferometry offers enhancement due to the spectral phase sensitivity $d\Phi/d\omega$ being proportional to the group index $n_g(\omega)$ [109–111].

In this section, we will focus on gathering spectral information upon time correlated detection using the strong dependence of $n_g(\omega)$ on the frequency ω. Indeed, in a strongly dispersive slow-light medium different spectral components map to different arrival times which are used to stretch ultra fast laser pulses and to capture their frequency spectra [112]. Due to mutual dependence of dispersion and pulse delay or distortion, the temporal information has even been used for km-long optical fibers to infer information about the material dispersion or spectrum of the transmitted pulses [113, 114]. The pulse duration in these cases were in the picosecond regime which can be delayed and distorted even in micron sized photonic crystals due to the much higher dispersion in these structures [105]. Elaborate techniques e.g. by inducing stimulated Brillouin scattering resonances in m-long fibers have shown high and tunable group velocity dispersion eventually allowing an impact for propagating nanosecond pulses [115]. Moreover, using a dispersion compensating fiber that offers strong group velocity dispersion, the joint spectrum of en-

This section is reproduced in parts from:
H. Vural et al., PRB **101**, 161401 (2020) ©2020 American Physical Society
H. Vural et al., Optica **5**, 367-373 (2018) ©2018 Optical Society of America

tangled photons from a parametric down-conversion source has been measured [114]. However, the THz bandwidths probed so far lies within the resolution limit of grating spectrometers and in particular is orders of magnitude larger than typical QD spectra.

Here, we explore at the example of a hot Cs vapor and QD photons the GHz bandwidth regime of slow-light spectroscopy, which is below the resolution limit of grating spectrometers. By benefiting from single-photon detector technology that allows temporal resolution in the sub-nanosecond regime, the deduction of high-resolution spectra from time domain measurements will be demonstrated. This shall serve to benchmark the spectroscopic capabilities of this specific interface and strengthen the subsequent important study on the spectral diffusion dynamics.

5.1.1 Dispersive mapping into time domain

To illustrate the concept of mapping frequency domain of single photons onto the time domain, we theoretically examine the propagation of exponentially decaying wavepackets (Lorentzian in the frequency domain $\chi_i^L(\omega)$) in a single spatial mode via TCSPC and FCSPC (the subscript i of $\chi_i^L(\omega)$ indicates the carrier frequency, the superscript L the propagation length, see Eq. (2.7)). The parameters are chosen similar to the upcoming experimental conditions with a decay constant of $\tau = 0.5\,\mathrm{ns}$ and the vapor cell length $L = L_V = 10\,\mathrm{cm}$ that is kept at a temperature of $T_V = 125\,^\circ\mathrm{C}$ which delivers a group index of $n_g = 22$ at $\omega/2\pi = 0.8\,\mathrm{GHz}$ detuning and $n_g = 13$ at $\omega/2\pi = 9.8\,\mathrm{GHz}$.

The medium's linear response, given by $n(\omega)+\frac{i}{2\omega/c}\alpha(\omega)$, performs the following mapping on the wavepacket $\chi(\omega)$ of finite bandwidth:

$$\chi_i^0(\omega) \longmapsto \chi_i^L(\omega) = \chi_i^0(\omega) e^{-\frac{L}{2}\alpha(\omega)} e^{i\frac{Ln(\omega)}{c}\omega} \quad . \tag{5.1}$$

The absorption $\alpha(\omega)$ reduces the amplitude, while the refractive index $n(\omega)$ introduces an effective propagation length $L{\cdot}n(\omega)$. This changes the relative phase between the frequency modes of a wavepacket causing an interference and modification of the temporal shape of single

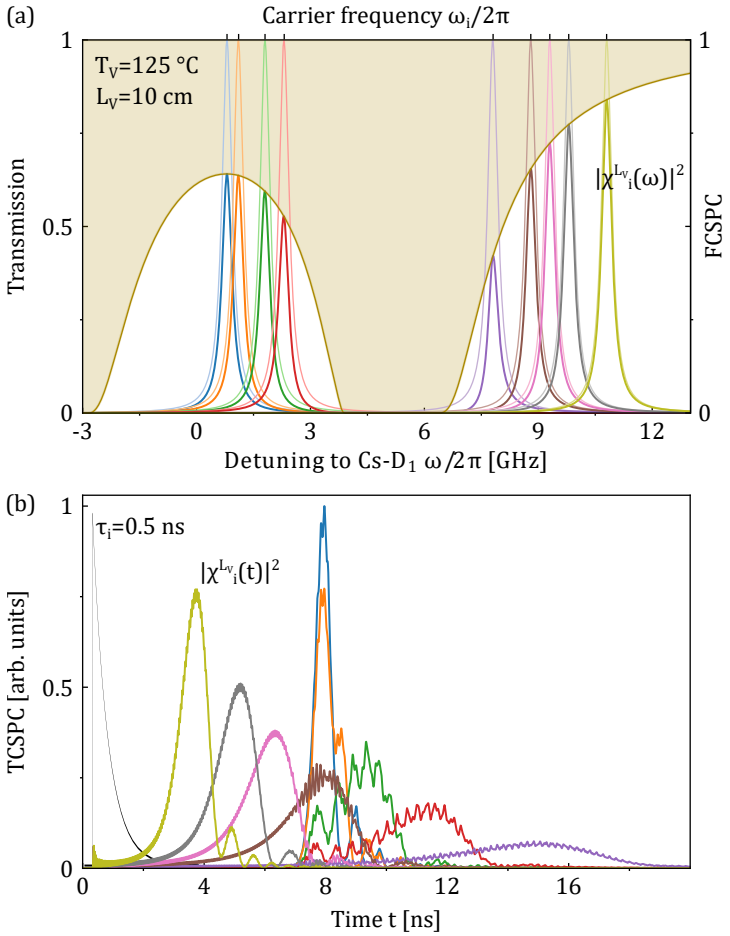

Figure 5.1. (a), Frequency domain: Lorentzian photons at various carrier frequencies ω_i before (thin) and after (thick) the Cs vapor of length L_V at temperature T_V. Transmission profile of vapor shown as shaded area. (b), Time domain: Transmitted photons corresponding with same color code as in the frequency domain. All photons enter the vapor with same initial decay constant $\tau_i = 0.5$. For comparison, the black curve, which corresponds to free space propagation, is shown.

photon pulses $|\chi_i^L(t)|^2 = |\mathcal{FT}\left\{\chi_i^L(\omega)\right\}|^2$, since the Fourier-transform $\mathcal{FT}$ operation is preceding the absolute square. Given the finite width of a Lorentzian and the strongly frequency dependent group index (see Fig. 2.2b) a pulse distortion is already expected.

In Fig. 5.1a, the initial spectrum is compared to its transmitted counterpart for selected carrier frequencies ω_i around the Cs-D_1 lines. A measurement of the photons in the frequency domain delivers $|\chi_i^{L_V}(\omega)|^2 = |\chi_i^0(\omega)|^2 e^{-L_V \alpha(\omega)}$, which reflects only the impact of absorption on the photons. The transmitted spectra are mostly still close to Lorentzian while the acquired phase of each frequency component is lost. This is contrary to the respective time domain which discloses the effect of dispersion, as shown in Fig. 5.1b.

A measurement of the intensity of a photon does not disclose any information on the phase and its spectral properties when propagated in free space $|\chi_i^{L_V}(t)|^2 = \frac{1}{\tau} e^{-(t-t_0)/\tau}\Theta(t-t_0)$ (black curve for all carrier frequencies), yielding the decay constant τ as the only identifiable parameter. However, upon propagation through the strongly dispersive Cs vapor, distinct temporal profiles occur for photons at different carrier frequencies. The very particular interference pattern of the transmitted photons allow assignment to their respective frequency domain. Hence, the usually undesired pulse distortion IS exploited for spectroscopic purposes, mapping frequency onto time domain.

Impact of line broadening

To gain an intuition on this type of spectroscopy with rather uncommon temporal profiles, we consider the impact of typical line broadening onto the time domain after the Cs vapor. Firstly, Lorentzian broadening under two different mechanisms is simulated (see Fig. 5.2a). One spectrum shall consist of an ensemble of Fourier-limited photons where broadening results upon a Lorentzian distribution of jittering carrier frequencies (blue curves). In the other case, a pure dephasing process is considered, where each photonic spectrum displays random sidebands such that the resulting total spectrum

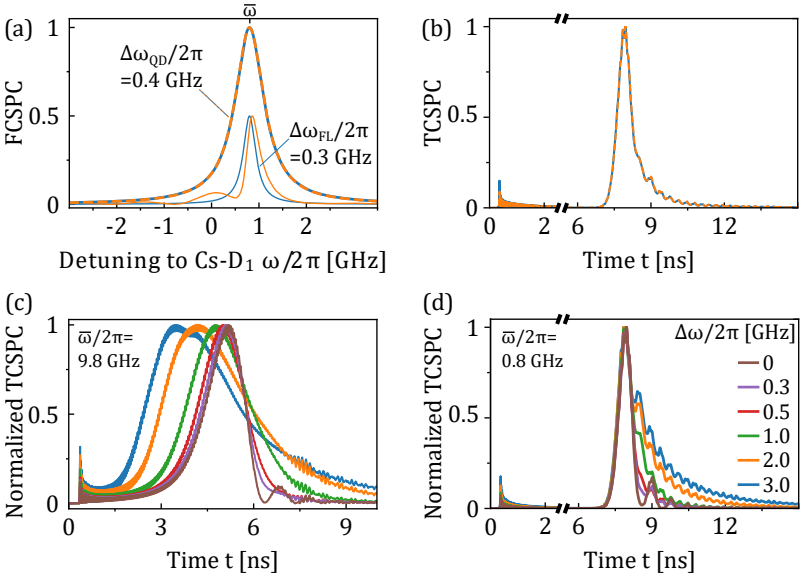

Figure 5.2. (a), Frequency domain signal of two individual photons and the total Lorentzian broadened spectra under the influence of a carrier frequency jitter of Fourier-limited photons (blue) or a pure dephasing process (orange). (b) Time domain signal of the spectra in (a). (c) & (d), Time domain signal of Gaussian broadened spectra with the center of emission at $\bar{\omega}$ and FWHM of Gaussian jitter distribution $\Delta\omega$. Legend applies to both plots.

is again Lorentzian broadened (see [74] and section 2.3.3). A measurement of the spectra via FCSPC would display the overlapping broadened Lorentzians. Because single photons deliver just a "click" at a certain frequency, the acquisition of the spectrum must integrate over many photons. For that reason, their is no way to distinguish the origin of broadening in this case, in particular a decision whether each photon is Fourier-limited or not cannot be made.

Fig. 5.2b shows the TCSPC signal when the Lorentzian broadened

emission spectra are propagated through the Cs vapor. The temporal profile of the broadened ensembles are delayed by about 8 ns and stretched due to dispersion. The temporal profiles of the total spectrum overlap as they do in the frequency domain. This suggests that the acquisition of an emission spectrum via slow-light spectroscopy is equivalent to a FCSPC measurement, reflecting the broadened stationary emission spectra only but hiding the cause of broadening. Moreover, this indicates that a jitter distribution of Fourier-limited photons can be used to describe broadened emission spectra under either mechanism.

In general, QD spectra are dominantly Gaussian broadened. For that, Fig. 5.2c and d shows simulations of the time domain signal of Gaussian broadened emission after the vapor. The spectra are investigated for two choices of emission center $\bar{\omega}$ and several widths $\Delta\omega$ of the jitter distribution consisting of Fourier-limited photons. At $\bar{\omega}/2\pi = 0.8\,\mathrm{GHz}$ detuning to Cs-D_1 the photons are homogeneously delayed owing to more uniform group velocity within the transmission window of the vapor (see Fig. 2.2b). The increase of Gaussian line width is reflected as temporal broadening and distinct decays. Despite the ensemble of various carrier frequency, the signatures of interference are present as oscillatory slopes.

In contrast, the emission centered at $\bar{\omega}/2\pi = 9.8\,\mathrm{GHz}$ displays largely distributed profiles due to a more dispersed group velocity distribution (see Fig 2.2b). This increases the sensitivity of slow-light spectroscopy while revealing that the edge of even a single Doppler-broadened vapor response would be exploitable for spectroscopic purposes. However, to realize a low distortion delay line, the center of two neighboring absorption lines is more suitable. In any case, given the usual high signal-to-noise ratio in TCSPC, the distinct temporal profiles are expected to allow the determination of the underlying Gaussian distributions. In the following experimental studies, the center of vapor transmission is chosen to be at $\bar{\omega}/2\pi = 0.8\,\mathrm{GHz}$ in order to keep temporal overlap of consecutively emitted photons minimal.

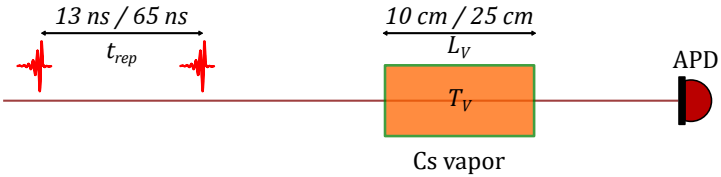

Figure 5.3. Experimental setup of the slow-light spectroscopy. Two options of laser repetition time t_{rep} and vapor cell length L_V are utilized.

5.1.2 Slow-light spectroscopy of the emission of QDs

The experimental setup to perform slow-light spectroscopy via TCSPC measurements is shown in Fig. 5.3. The emission of the QD under resonant π-pulse excitation is directed in a single spatial mode through a Cs vapor cell that is nominally kept at $T_V = 125\,°\mathrm{C}$. To avoid temporal overlap of successively emitted photons for the standard laser repetition of $t_{rep} = 13\,\mathrm{ns}$, a cell of length $L_V = 10\,\mathrm{cm}$ is utilized. Alternatively a cell of length $L_V = 25\,\mathrm{cm}$ is used which however necessitates the operation of a pulse picker to reduce the repetition rate to $t_{rep} = 65\,\mathrm{ns}$. The spectroscopy is performed at the center of Cs-D_1 lines' transmission window to keep stretching of the signals below the repetition. Suitable QD candidates on the sample are selected and their wavelength fine-tuned to the target frequency via the application of strain (see chapter 4).

Fig. 5.4a shows TCSPC for QD C, where the longer cell length and repetition are used. Compared to free space propagation the photonic wavepackets arrive at the detector with a huge vapor-induced delay of around $\Delta t_V = 17\,\mathrm{ns}$, further displaying the anticipated pulse distortion. To extract spectroscopic information from the time domain, a theory curve is simulated to fit the data under the assumption of a Gaussian broadened emission spectrum which consists of Fourier-limited single photons. For that, the measured initial decay constant of $\tau = 0.46\,\mathrm{ns}$ is fixed and a fit routine that evaluates $\langle|\chi_i^{L_V}(t)|^2\rangle_{\mathcal{N}}$

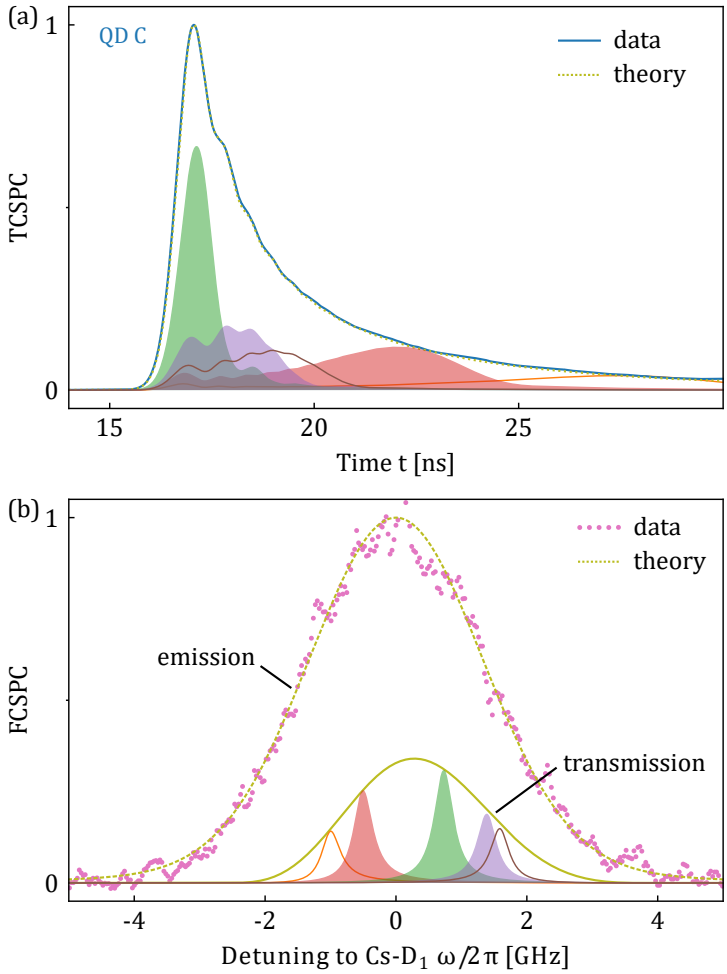

Figure 5.4. (a), Time domain of photons from QD C after propagation through the vapor. (b), Frequency domain interred from the time domain. Single Fourier-limited photons are included in both domains with corresponding color coding.

is performed, while vapor temperature, center $\bar{\omega}$ and FWHM $\Delta\omega$ of the Normal distribution $\mathcal{N}$ are varied.
The rising edge of the signal tightly determines the vapor temperature being $T_V = 123.9 \pm 0.1\,°\mathrm{C}$ in this case. The FWHM of the stationary Gaussian jitter is revealed to be $\Delta\omega/2\pi = 3.0 \pm 0.1\,\mathrm{GHz}$ with the center of emission at $\bar{\omega}/2\pi = 0 \pm 0.1\,\mathrm{GHz}$ detuning. Owing to high signal-to-noise ratio and excellent matching of theory with data, the uncertainty in frequency domain is comparable to high resolution spectra measured by a scanning FPI. Straightforward significant sensitivity improvements can be gained by increasing vapor temperature or tuning the center of emission to the wings of vapor transmission.
In Fig. 5.4b the independent FCSPC measurement of the emission spectrum of the QD is compared to the one that is revealed by slow-light spectroscopy. The accurate matching demonstrates the suitability of the method. Note, that the transmitted QD emission through the vapor amounts for 25% of the total emission spectrum. This is more than an order of magnitude higher than the mean transmission of a scanning FPI, which is why the introduced method comes with high signal-to-noise ratio.

In the theoretical introduction, it was pointed out that the measurements of spectrum with either method does not reveal any dynamics of the emission spectrum due to slow integration, but can only capture its stationary limit. To indicate the cumulative creation of the measured temporal profile, both complementary domains of single Fourier-limited photons are plotted for selected carrier frequencies. Remarkably, despite the inclusion of detector jitter that smoothes out fast modulations in the temporal shapes, the data still possesses a clear undulation. Supported by a perfect overlap of data and theory, two implications can be drawn out of it with regard to the quantum mechanical nature of the single photons.
First, given the interference-induced beats in the time domain data, any single photon must be in a superposition of its frequency components which proofs the validity of single photon wavepacket description according to Eq. (2.1). The interference of a single photon with itself after splitting and recombination into spatial modes is a famous

example to reveal its quantum nature [65]. Here, an analogy with regard to the frequency modes of a single quantum is demonstrated while the interference is resolved in the time domain.
The second implication is that the stationary spectrum can indeed be described as consisting of Fourier-limited wavepackets where the carrier frequencies are distributed according to the total spectrum. This is in analogy to a description of the emission spectrum via a density matrix of a mixed state that consists of pure states given by the single-photon wavepackets at certain carrier frequencies.

Conclusively, pulse distortion of single photon wavepackets in time domain reveals the spectrum and allows thereby to validate basic principles of the quantum mechanical description.

Slow-light spectroscopy of QD A and QD B

Fig. 5.5 shows slow-light spectroscopy of two further QDs using the shorter vapor cell of length $L_V = 10\,\mathrm{cm}$. To operate at the group indices $n_g(\omega) \gtrsim 20$ as before, the vapor temperature is set similar amounting to $T_V = 123.7\,^\circ\mathrm{C}$ for QD A and $T_V = 124.9\,^\circ\mathrm{C}$ for QD B. The delayed signal of $\Delta t_V \approx 7\,\mathrm{ns}$ after the vapor is shifted to compare the pulse distortion with the exponential decay without the vapor in path. Once again, theory curves are fitted to the data in the time domain to reveal the emission spectra of the QDs. This time however, the spectra are not only Gaussian broadened but consist of two separated lines, denoted as L and R. Despite the more complex spectra, the fit procedure yield results well matching the measured spectra. However, the fit to converge needs initialization with two Gaussian distributions. For complex line shapes that consists of several lines of various strengths [48, 116] this may cause an issue with convergence. In those cases, tuning the emission center from the bell shaped transmission window to its wings where vapor response is strongly asymmetric and more sensitive to detuning, could lift those difficulties.

All measured emission lineshapes display a line width of the stationary spectrum almost an order of magnitude larger than the

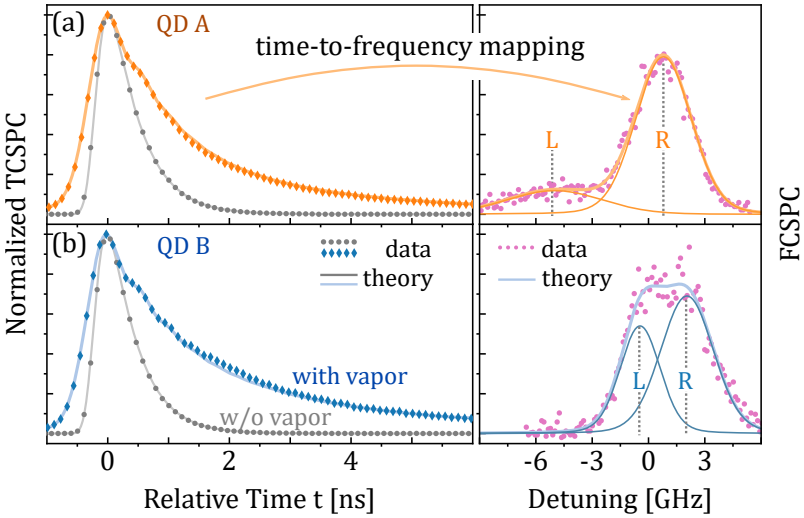

Figure 5.5. (a), Left panel: time domain of photons from QD A with and without the propagation through the Cs vapor. The data with vapor are shifted by $\Delta t_V \approx 7$ ns for sake of comparison. Right panel: Inferred emission spectrum and data measured by a scanning FPI. (b), The same as in (a) for QD B.

Fourier-limit $\Delta\omega_{FL} = 0.35\text{-}0.4$ GHz. This reveals a strong environmental influence on the two-level systems. The inhomogeneous Gaussian broadening marks a quasi-static environmental noise with regard to the radiative decay time [49, 73], yet with a large fluctuation amplitude.

The two distinct lines present in the spectra of the charged excitons of QD A & QD B has been reported to arise from the Stark-shift of an occupied charge trap in the vicinity to the QD's strain field [48, 116]. Since here no external magnetic field is applied and dynamic nuclear spin polarization is avoided by pumping the QD under linear polarization, a distinct Zeeman-splitting of the transitions can be excluded. Hence, based on the 5.8 GHz frequency difference between the lines

L and R of QD A, its distance to the charge trap is estimated to be $\sim$ 25 nm, while the 2.5 GHz for QD B yields $\sim$ 40 nm [116]. Note, that the lines L & R of the QDs do not share the same width, which shows altered environmental influences on the same QD depending on the filling of the charge trap. Comparing the QDs, the lines of QD A are broader which is consistent with a stronger impact of the closer charge trap.

Discussion

Slow-light spectroscopy, as demonstrated using a hot Cs vapor, convinces with faithful mapping of spectral information onto the time domain thereby competing in precision with interferometric techniques to measure emission spectra. It comes with a restriction to a narrow wavelength range but with the benefit to avoid moving parts as is the case for a scanning FPI or Fourier spectroscopy. However, this method can be realized in any slow light media [60] and extended to arbitrary wavelength regimes by tailoring dispersive waveguide structures [117]. Its particular strength lies in the perspective of on-chip integration and miniaturization [118, 119], which could play an important role for the future of integrated quantum technologies [120]. When a length constrain is dismissed, the presented method is applicable to any medium with finite non-linear refractive index curve over the bandwidth of a photon and broadening, respectively. If at least group velocity dispersion (GVD) is present, the interaction length L for observing a significant temporal pulse distortion and broadening after the propagation in the dispersive medium is given by:

$$L \approx \mathrm{GVD}^{-1}(\omega) \cdot \tau^2 \tag{5.2}$$

where τ is the pulse length. Hence, a small GVD does not disqualify the medium's use but necessitates an increased length of the interaction to reveal spectral properties out of temporal detection.

It is worth to mention that the observed stationary limit of the spectrum determines the maximally achievable two-photon interference with independent emitters, which is a key figure of merit for

lots of quantum technologies. So far unity interference visibility of independent remote emitters remain elusive due to non Fourier-limited stationary spectra of solid-state emitters under non-resonant or resonant pulsed excitation [92, 121–123]. Despite a modest interference visibility achieved in interfering remote QD emitters, near-unity visibility could be demonstrated for photons emitted by the same source [124]. For that, it is important to unveil the temporal dynamics of spectral diffusion, thus the cross over from high to low coherence. In the following section, the extension of slow-light spectroscopy to correlation measurements is performed that enables to reveal the QD's spectral diffusion.

5.2 Studying the spectral diffusion dynamics in QDs

The Gaussian inhomogeneous broadening encountered in the stationary QD spectra is arguably dominated by a slow (with regard to the radiative decay) change of the emission frequency. A QD transition is subject to decoherence because of coupling to it's mesoscopic environment. As schematized in Figure 5.6, in general, three interaction mechanisms play a dominant role.

(i) The influence of linear phonon coupling causes largely distributed side bands, and under quadratic coupling broaden the zero-phonon line [54] eventually degrading coherence of the emission. Cooling to 4 K and embedding the QD into a photonic cavity structure renders phonon decoherence to a marginal level [85]. (ii) The hyperfine interaction of charge carrier spins with $\sim 10^5$ nuclear spins of the atoms that form the QD is intrinsic to InGaAs QDs [42], being enhanced when an unpaired spin is localized in the QD [125]. Causing diverse effects that translate into the QD's spectrum, the hyperfine

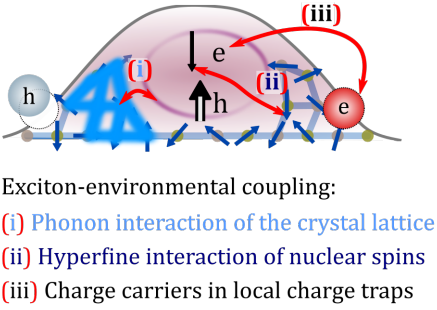

Figure 5.6. Illustration of the environmental coupling to QD-confined charge carriers.

interaction can be a limiting factor in the photon indistinguishability due to diffusion and fluctuation of the nuclear spins. Optical dynamic nuclear spin polarization and application of external fields have proven to reduce fluctuations [125, 126]. (iii) Charge noise is the main obstacle for many sample structures [55]. Charges trapped in the vicinity of a QD shift its transitions via the Stark-effect, while their fluctuations induce spectral diffusion and inhomogeneous broadening over time [48, 52, 116]. High quality growth [127] can reduce crystal defects which are generally located at layer interfaces, while passivation techniques neutralize effectively surface states [128] yielding state-of-the-art photonic structures and cavity systems [129].

To predict performances in quantum applications, famously HOM interference of consecutively emitted photons, the information gained in the measured stationary spectra is insufficient. This limitation applies also to standard Fourier spectroscopy [71], since the fundamental Wiener-Khinchin theorem relates to the stationary spectrum only [49,130]. Nevertheless, the dynamics of fluctuations in the emission frequency can be investigated by various means.

The majority of techniques to characterize spectral diffusion on the single emitter level probe the resonant scattering of the two-level system with a weak laser. The methods applied to date on QDs are spin noise spectroscopy [131] that probes laser polarization rotation, counting the photon statistics of florescence [132] and autocorrelation of the intensity time trace [52, 53], as any line shift of the QD transition translates into altered intensity. Applying the latter method, the different detuning-dependence of the sensitivity to spin and charge noise and disparity of their timescales have been used to identify the origin of fluctuations. For charged excitons, spin noise show a correlation time constant of tens to 100 microseconds while charge noise happens on milliseconds and beyond in charge coupled devices investigated by weak laser probe [52, 53]. However, excitation power influences both timescale and fluctuation amplitudes indicating that

This section is reproduced in parts from:
H. Vural et al., PRB **101**, 161401 (2020) ©2020 American Physical Society
H. Vural et al., Appl. Phys. Lett. **117**, 030501 (2020) ©2020 AIP Publishing

the quantification of spectral diffusion and HOM interference visibilities needs to be studied under the realistic pumping conditions.
Photon-correlation experiments after a narrow band filter can be performed under any excitation condition, however it is only indicating time scales of spectral diffusion [133, 134]. Another possibility is given by the direct study of HOM interference over the time difference of consecutive photons. This is often anyhow the desired information and can itself be used to reveal spectral properties of the emitter [72, 92]. The interference visibilities showed decays over various timescales of a few nanoseconds [93, 135], hundreds of nanoseconds [94] or microseconds [92, 96], demonstrating that decoherence is characteristic to the sample structure. However, the HOM visibilities corresponding to the stationary spectra were not reached in the range of investigations up to 15 μs, showing the insufficiency of these studies to cover the whole interesting range as delaying for photon synchronization at the beam splitter is an issue. Moreover fiber dispersion tend to dominate the wavepacket overlap reduction even for telecommunication wavelength at 1550 nm [92].
A method that probes the photons after their emission and without limitations on the investigated timescales is given by photon-correlation Fourier spectroscopy [136], recently used to resolve the temporal evolution of line broadening in biexciton-exciton cascades [137]. It utilizes a Michelson interferometer with displaced input and output paths to probe the coherence of consecutive photons via intensity correlation measurements over the path length difference.

Here, we introduce and demonstrate an alternative method based on the present hybrid interface: slow-light photon-correlation spectroscopy. This method exploits frequency dependent pulse distortion in the slow-light medium which is combined with photon-correlation to reveal the temporal dependency of emission frequency fluctuations. Significantly, it necessitates only a single correlation measurement to quantify the spectral diffusion over all time scales. In the following, first a model of QD spectral diffusion is described and its relation to time-dependent two-photon interference visibility is derived. This is

followed by the experimental investigation of QDs A & B which complements on the stationary emission spectrum presented in Fig. 5.5.

5.2.1 Classical diffusion model of the QD's spectral diffusion

The processes which cause spectral diffusion vary for the different material systems. However, in many cases, the stationary distribution of spectral diffusion happens to be a Gaussian, often a consequence of the central limit theorem [138]. A statistical description of the dynamics of spectral diffusion appears therefore mandatory [139]. Assuming the QD's transition frequency shifts caused by n independent two-state jump processes, the limit $n \mapsto \infty$ converges to the Ornstein–Uhlenbeck (OU) stochastic process, the only stationary Markovian Gaussian noise process [140]. The validity of this limit in the case of a QD can be expected just from the Gaussian stationary spectrum that is indicative for hyperfine coupling of the charge carrier spin to $\sim 10^5$ fluctuating nuclear spins and a large number of Stark-shifts of trapped and released charges further apart from the QD [42, 55].
Based on the Gaussian stationary spectrum, the spectral diffusion is moreover identified as a classical diffusion process rather than a quantum walk [141]. Indeed, the OU process which will be applied to effectively describe the spectral diffusion of the emission frequency, arises from the classical diffusion of a particle which undergoes a Brownian motion in a harmonic potential. In contrast to standard Brownian motion, the inclusion of a harmonic potential leads to the desired stationary and localized Gaussian distribution. The Smoluchowski equation in the form of a Fokker-Planck equation can be consulted to describe the evolution of the probability distribution function $p\left(x_2, t_2 | x_1, t_1\right)$ of the particle's position x_2 at time t_2 conditioned on initial position x_1 at time t_1. Here, the well known treatment of this problem and it's solution which is referred to as the Ornstein-Uhlenbeck process [142] is adapted. Replacing the position x_i with the emission carrier frequency ω_i and adjusting the constants yield

the solution $p_c^{\overline{\omega},\sigma}(\omega_2, \delta t|\omega_1)$ which predicts the probability of carrier frequency ω_2 of a photon emitted with time-difference δt following the emission of a first photon with carrier frequency ω_1:

$$p_c^{\overline{\omega},\sigma}(\omega_2, \delta t|\omega_1)$$
$$= \frac{1}{\sqrt{2\pi\sigma^2 S_c(\delta t)}} \exp\left[\frac{\left(\omega_2 - \overline{\omega} - (\omega_1 - \overline{\omega})\sqrt{1 - S_c(\delta t)}\right)^2}{2\sigma^2 S_c(\delta t)}\right]$$

$$\text{where} \quad S_c(\delta t) = 1 - \exp\left[-\frac{\delta t}{\tau_c/2}\right] \quad . \tag{5.3}$$

The physical mechanism c inducing the spectral diffusion is indicated with the subscript, while τ_c and σ are the important characteristic parameters of the process.
The probability of the first emission frequency follows the stationary Gaussian distribution $\mathcal{N}(\overline{\omega}, \sigma^2) = p_c^{\overline{\omega},\sigma}(\omega_1, \infty|\cdot)$ with center $\overline{\omega}$ and variance σ^2 (FWHM is $\Delta_c = 2\sqrt{2\ln(2)}\,\sigma$). Note, that this implies a sampling rate of first photons well below the time constant of spectral diffusion, which is fulfilled within the frame of our experiments.
Fig. 5.7a shows the time dependent probability distribution for a photon's carrier frequency ω_2, conditioned on a former emission at the frequency ω_1. For a short time difference $\delta t \mapsto 0$, the conditional probability $p_c^{\overline{\omega},\sigma}(\omega_2, \delta t|\omega_1) \mapsto \delta(\omega_2 - \omega_1)$ and hence the photons have likely identical frequencies. With increasing time difference between the photons, the distribution gets broader and it's center shifts towards the mean of the stationary Gaussian distribution. For long time differences $\delta t \mapsto \infty$, the second photon will be distributed according to the stationary Gaussian $p_c^{\overline{\omega},\sigma}(\omega_2, \infty|\cdot)$ independent of the initial frequency. This broadening mechanism produces a time-difference dependent line width leading to a characteristic exponential decay of the correlation function of emission frequencies: $\langle\omega_1(0)\omega_2(\delta t)\rangle \propto \exp(-\delta t/\tau_c)$, where τ_c can be defined as the emission frequency correlation time constant.

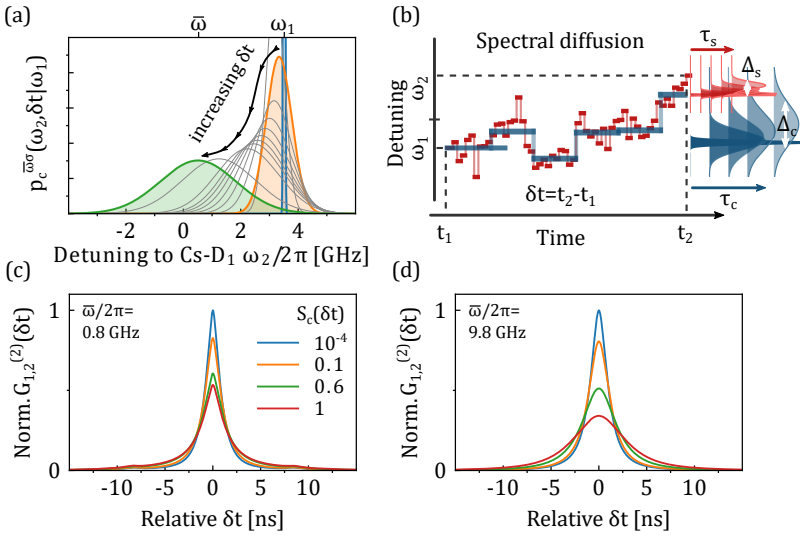

Figure 5.7. (a), Evolution of the probability distribution for the carrier frequency ω_2 of the emission conditioned on the initial emission at ω_1 . Green shaded Gaussian is the stationary distribution, orange area is a distribution after a short time difference δt and the gray curves are all in between. (b), Illustration of spectral diffusion composed of two independent OU processes c (blue) and s (red), with distinct time constants τ_i and widths Δ_i. (c) & (d), Simulations of photon correlation according to Eq. (5.7) for a diffusive emission of total line width of $\Delta_c = 3\,\mathrm{GHz}$ centered at $\bar{\omega}$ for various times parameterized by $S_c(\delta t)$. Legend applies to both plots.

In order to account for the known spectral diffusion mechanisms [52], the combination of two independent OU processes and a static Gaussian distribution is taken as an ansatz. The motivation behind this assumption is that each process is linked to independent noise processes of disparate timescales. The particular state of a noise source within the ensemble of possible states will determine the energy (and thus emission frequency) corresponding with this process

(see Fig. 5.7b). Diffusing independently to this, the second noise source will lead to a certain state and a corresponding energy shift. The cumulative energy-shifts will in the end determine the final carrier frequency of emission. Taking further a static distribution into account, the total spectral diffusion process $P(\omega_2, \delta t|\omega_1)$ is given by the following integral:

$$P(\omega_2, \delta t|\omega_1) = \int dc_1 dc_2 ds_1 ds_2 \quad p_c^{\overline{\omega},\zeta}(c_1, \infty|\cdot)\; p_c^{\overline{\omega},\zeta}(c_2, \delta t|c_1) \times$$
$$p_s^{c_1,\sigma}(s_1, \infty|\cdot)\; p_s^{c_2,\sigma}(s_2, \delta t|s_1 + c_2 - c_1)\; p_{ph}^{s_1,\kappa}(\omega_1, \infty|\cdot)\; p_{ph}^{s_2,\kappa}(\omega_2, \infty|\cdot) \tag{5.4}$$

As argued above, the initial emission frequency ω_1 stems from the respective stationary distributions of the processes. The first Gaussian distribution $p_c^{\overline{\omega},\zeta}(c_1, \infty|\cdot)$ describes the probability to emit the carrier frequency c_1 due to the charge noise. The state of spin diffusion shifts c_1 to s_1 with the probability $p_s^{c_1,\sigma}(s_1, \infty|\cdot)$. The static distribution of mainly phononic origin, indicated by ph, comes on top shifting s_1 to the final emission frequency ω_1. Its probability is given by the product of $p_{ph}^{s_1,\kappa}(\omega_1, \infty|\cdot)$ with the first two distributions.
After the time difference δt elapses, the diffusion induced by charge noise is at a state which would lead to the emission of carrier frequency c_2 with the probability $p_c^{\overline{\omega},\zeta}(c_2, \delta t|c_1)$. Once again, the independent spin diffusion shifts c_2 to s_2 which on account of shifted charge noise is given by the probability $p_s^{c_2,\sigma}(s_2, \delta t|s_1 + c_2 - c_1)$. The final emission frequency is ω_2 which comes from the static distribution $p_{ph}^{s_2,\kappa}(\omega_2, \infty|\cdot)$ centered at s_2.

The integral accounts for all possibilities where initial emission occurs at ω_1 and final frequency after the time difference δt is ω_2. The compact solution to the integral in Eq. (5.4) is given by:

$$P(\omega_2, \delta t|\omega_1) = \frac{1}{2\pi\sqrt{\Sigma^2(\delta t)\widetilde{\Sigma}^2(\delta t)}} \times \exp \tag{5.5}$$
$$\left[\frac{\frac{\Sigma^2(\delta t)+\widetilde{\Sigma}^2(\delta t)}{2}\left((\omega_1-\overline{\omega})^2+(\omega_2-\overline{\omega})^2\right)+2(\omega_1-\overline{\omega})(\omega_2-\overline{\omega})\frac{\Sigma^2(\delta t)-\widetilde{\Sigma}^2(\delta t)}{2}}{-2\Sigma^2(\delta t)\widetilde{\Sigma}^2(\delta t)}\right]$$

$$\text{where } \Sigma^2(\delta t) = \zeta^2 \left(1 - \sqrt{1 - S_c(\delta t)}\right) + \sigma^2 \left(1 - \sqrt{1 - S_s(\delta t)}\right) + \kappa^2$$
$$\text{and } \widetilde{\Sigma}^2(\delta t) = \zeta^2 \left(1 + \sqrt{1 - S_c(\delta t)}\right) + \sigma^2 \left(1 + \sqrt{1 - S_s(\delta t)}\right) + \kappa^2$$

Please note that additional independent OU processes could be included in a straightforward way into Eq.(5.5), just by the obvious scheme in $\Sigma^2(\delta t)$ and $\widetilde{\Sigma}^2(\delta t)$.

5.2.2 Mapping spectral diffusion into time domain

In the previous section, the slow-light induced mapping of a certain carrier frequency into time domain was discussed, which manifests itself as a distinct delay and pulse distortion. In particular, a narrow distribution of the emission spectrum implies a shorter signal in the time domain (see Fig. 5.2c & d), as photons closer in frequency end up similar in time. This feature can be used to assess the time-dependent line width of the QD's emission spectrum which results from the presence of spectral diffusion.
To do so, photon-correlation after the slow-light medium is considered, which delivers the time difference between the detected photons and the temporal shape of their cross-correlation. Given a first photon with carrier frequency ω_1 and a consecutive one emitted after the time difference δt with ω_2, the (classical) correlation after a slow-light medium of length L is described by:

$$G^{(2)}_{1,2}(\delta t) \propto \int dt\ |\chi_1^L(t)|^2\ |\chi_2^{L;c\delta t}(t+\delta t)|^2 = |\chi_1^L(t)|^2 \star |\chi_2^{L;c\delta t}(t)|^2. \tag{5.6}$$

In the course of a measurement, the spectral diffusion process $P(\omega_2, \delta t|\omega_1)$ will imprint the time-difference dependent shapes of all possible emission frequency combinations onto the correlation peaks:

$$\langle G^{(2)}_{1,2}(\delta t)\rangle_{P(\omega_2,\delta t|\omega_1)} \propto \langle |\chi^L_1(t)|^2 \star |\chi^{L;c\delta t}_2(t)|^2\rangle_{P(\omega_2,\delta t|\omega_1)} \quad , \qquad (5.7)$$

where, $\langle . \rangle_{P(\omega_2,\delta t|\omega_1)} = \int \mathrm{d}\nu_1 \mathrm{d}\nu_2 \; P(\omega_2, \delta t|\omega_1) \; |\chi^L_1(t)|^2 \star |\chi^{L;c\delta t}_2(t)|^2$.

To gain an intuition for the mapping of spectral diffusion onto the time domain, in Fig. 5.7c & d we consider a simulation of photon-correlation $G^{(2)}_{1,2}(\delta t)$ after the Cs vapor for a QD's emission following a single OU process c. With increasing time difference δt described in terms of $S_c(\delta t)$, which parameterize the overall evolution of the diffusion process (see eq. (5.3)), a pronounced broadening in the correlation peaks can be seen. Accompanied by this, a strong decrease of the peak amplitudes is visible, reflecting the broadening in the frequency distribution of emission. Once again, access to spectral properties of the emission in time domain after a slow-light medium is gained, however revealing this time its dynamics.

5.2.3 Temporal evolution of two-photon interference

The HOM interference visibility is an important figure of merit for a quantum emitter. The presence of spectral diffusion renders the wavepacket overlap of consecutive photons a time dependent property. By means of time-difference dependent HOM measurements, the spectral diffusion could be probed. However due to the need of photon synchronization at the beam splitter, this method is very laborious and has been limited to 15 microseconds of fiber delay [95]. In contrast, slow-light photon-correlation spectroscopy neither necessitate any photon synchronization nor displays the exponential enhancement of absorption with the probed time difference. And vice versa, the measured spectral diffusion process allows to calculate the time dependence of the HOM interference visibility for the quantum emitter.

Using the two photon interference visibility $\left(1 + \frac{(\omega_2-\omega_1)^2}{\Delta\omega^2_{FL}}\right)^{-1}$ for Fourier-limited photons of carrier frequencies ω_1 and ω_2, we incor-

porate the spectral diffusion process given in Eq. (5.5) to yield an analytic expression of HOM interference visibility V_{HOM} over the time difference of emission δt of the spectrally diffusing single-photon source:

$$V_{\mathrm{HOM},P}(\delta t) = \langle \left(1 + \frac{(\omega_2 - \omega_1)^2}{\Delta\omega_{FL}^2}\right)^{-1} \rangle_{P(\omega_2,\delta t|\omega_1)} \tag{5.8}$$

$$= \sqrt{\pi}\frac{\Delta\omega_{FL}}{2\Sigma(\delta t)} \exp\left[\left(\frac{\Delta\omega_{FL}}{2\Sigma(\delta t)}\right)^2\right] \mathrm{erfc}\left[\frac{\Delta\omega_{FL}}{2\Sigma(\delta t)}\right] \tag{5.9}$$

Thus, the knowledge of the spectral diffusion process is crucial to quantify the persistence of quantum effects while utilizing a single emitter. This is of particular interest for determining the useful number of photons in multi-photon quantum implementations [95] and the crossover from high to low coherence.

5.2.4 Characterization of spectral diffusion dynamics in QDs by slow-light photon-correlation spectroscopy

The experimental setup to perform slow-light photon-correlation spectroscopy is shown in Fig. 5.8a. The emission of a QD under resonant π-pulse excitation is directed in a single spatial mode through a Cs vapor cell that is nominally kept at $T_V = 125\,^{\circ}\mathrm{C}$. To avoid temporal overlap of successively emitted photons upon pulse distortion in the dispersive medium, we again utilize the cell of length $L_V = 10\,\mathrm{cm}$ for the standard laser repetition of $t_{rep} = 13\,\mathrm{ns}$. The operation is performed at the center of the Cs-D_1 lines' transmission window to minimize overlap of neighboring correlation peaks.

Fig. 5.8b shows the normalized photon-correlation histograms of QD A & QD B comparing the results with and without the vapor in the path. As for the case without the vapor, the histograms display a suppression of the central peak due to the single photon nature of the emission. The narrow correlation peaks as given by the decay constants are separated by the laser repetition t_{rep}. Over several

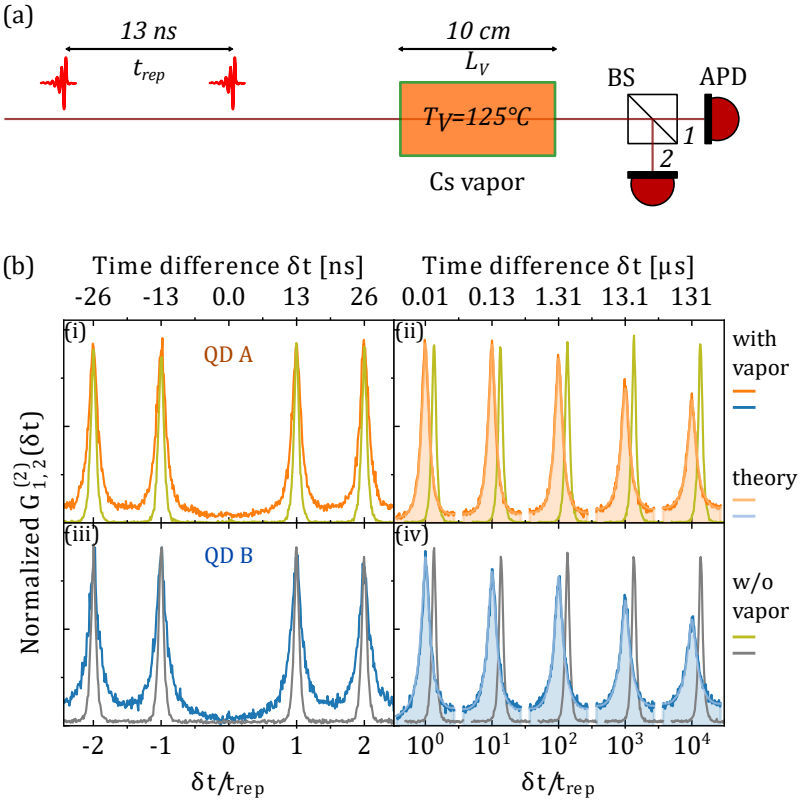

Figure 5.8. (a), Experimental setup of the slow-light photon-correlation spectroscopy. Laser repetition time is t_{rep} and vapor cell length L_V. (b), Normalized photon-correlation histograms over time difference δt for QD A & QD B without (olive and gray) and with (orange and blue) Cs vapor . Panels (i) and (iii) depict a short time window. Panels (ii) and (iv) depict selected correlation peaks over several timescales. Hereby, the peaks in the negative time differences axes are folded on top of the related positive ones to increase signal-to-noise ratio. The peaks without the vapor are shifted for the sake of clarity. Theory curves (light orange and light blue) are on top of the data.

timescales (see panels on the right hand side) the peak amplitudes and widths are as expected almost unchanged.
In contrast, the histograms using the vapor display strongly modified shapes. As expected, the anti-correlation in the central coincidence peaks is preserved, while the correlation peaks at multiples of the laser repetition are strongly broadened. More importantly, the temporal profiles of the correlation peaks, depicted over several timescales, show a significant reshaping. For increasing time difference between the detected photons, the peaks are strongly reduced in their amplitudes and noticeably broadened.

The observable reshaping of the peaks after the vapor testifies an evolving spectral diffusion over several timescales, since more distant carrier frequencies of photons result in broader correlation peaks. To reveal the parameters of the spectral diffusion dynamics, simulation curves as given by Eq. (5.7) are fitted for each of the lines L and R of the QDs (see Fig. 5.5). The cumulated theory curves excellently reproduce the correlation peak shapes, which evolve over time with rather uncommon profiles even not fitting to Voigt-profiles. Tab. 5.1 summarizes the inferred time constants and contributions of the different processes to the total spectrum.

For QD A two noise components with the time constants $\tau_c^A = 62 \pm 3\,\mu$s and $\tau_s^A = 7 \pm 1\,\mu$s are disclosed. This reveals that here charge (c) and spin (s) noise are both relevant contributions to the observed spectral diffusion. Moreover, a pronounced broadening below the laser repetition is revealed. At the sample temperature $\gtrsim 8\,$K this can mainly be associated to virtual phonon (ph) transitions that broaden the zero-phonon line [54]. Since the sample is glued on a piezo-transducer with poor thermal conductivity, the real temperature may lie even a few degrees higher, as already discussed in chapter 4. In addition, the observed static broadening may have contributions from undiscovered mechanisms originated in the growth mode, as MOVPE grown samples barely show very high indistinguishability of successively emitted photons.
As for QD B, charge noise is found to dominate the spectral diffusion dynamics and only one time constant $\tau_c^B = 22 \pm 1\,\mu$s is sufficient to

Table 5.1. Parameters extracted by the simulations: timescales of frequency correlation for the OU processes are τ_c and τ_s and corresponding linewidths are Δ_c and Δ_s; the width of the static Gaussian is Δ_{ph}; conditions of excitation, resonant π-pulse excitation (res.), or with the addition of weak cw non-resonant laser (res+nr). L and R are the two lines in the spectra of Fig. 5.5. τ_{LR} is the decay constant of jumps.

	unit	QD A		QD B		origin of
line		L	R	L	R	spectral
exc.		res		res+nr		diffusion
$\Delta_c/2\pi$	GHz	5.4	2.6	1.8	2.8	charge
τ_c	μs	62 ± 3		22 ± 1		noise
$\Delta_s/2\pi$	GHz	1.85 ± 0.1		–		spin
τ_s	μs	7 ± 1		–		noise
$\Delta_{ph}/2\pi$	GHz	0.9 ± 0.1		1.4 ± 0.1		phonon
τ_{LR}	ms	7.6 ± 0.1		6.8 ± 0.1		line jumps

describe the data. This different behavior is most likely connected to the preparation of the charged exciton state. While the charge state of QD A is by default given, most probably due to unintentional doping at its location, QD B necessitates a weak non-resonant laser for initialization of its charge state. The additional non-resonant laser with an energy above the bandgap continuously generates charge carriers dominating the noise coupled to the QD transitions even for very weak powers, in particular accelerating the fluctuations. This observation has been reported for studies under resonance fluorescence [52] and two-photon excitation [137], too.

Fig. 5.9a shows the peak amplitudes and areas for both QDs up to 250 μs, where the frequency correlations of the individual lines (R and L) become stationary. The growing discrepancy between peak area and amplitude over time difference signifies the broadening of peaks, however the peak shapes do change, too. The accurate matching of data and theory proofs the effectiveness of the utilized model consisting of OU processes. Notably, the composition of two OU

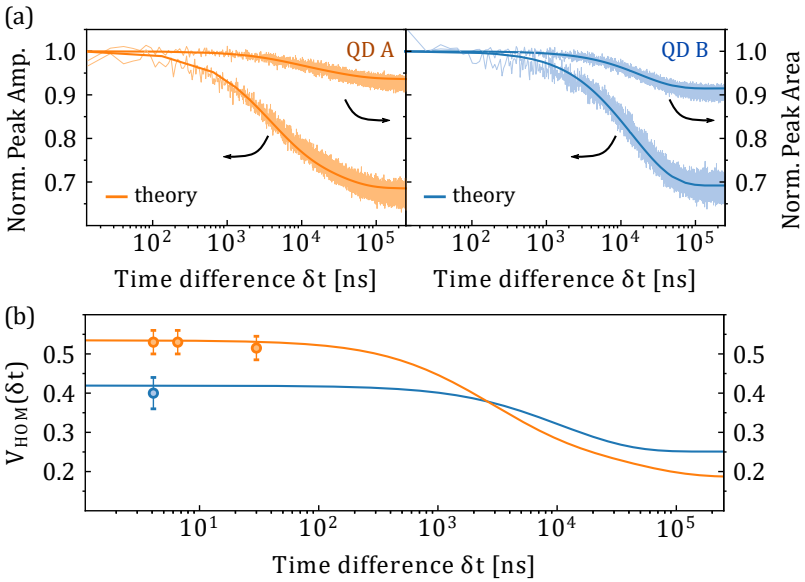

Figure 5.9. (a), Normalized correlation peak amplitude and area over the time difference. The curves on top of the data (light) represent simulation results. (b), Inferred HOM visibilities over time difference with color code matching (a). Circles represent independent HOM measurements.

processes for QD A is reflected in an earlier but flatter decay of correlations (in terms of correlation peak amplitudes) in comparison to the curves of QD B. The quantified diffusive and static broadening contributions to the spectrum can further be used to depict quantum optical properties of the non-classical light source, as the inferred broadening in each correlation peak is equivalent to a HOM measurement for photons with corresponding time difference δt. While the direct measurement of the HOM visibilities is demanding, the introduced method probes all time-differences simultaneously utilizing all detected photons without any need for further photon synchronization.

In Fig. 5.9b the time dependence of HOM visibility $V_{\mathrm{HOM}}(\delta t)$ inferred from the measured spectral diffusion is depicted. Independent HOM two-photon interference measurements for typical free space delays of $4, 6.5$ and $30\,\mathrm{ns}$ fit exactly to the curve, underpinning the reliability of the slow-light photon-correlation measurements. QD A starts at a higher visibility due to the narrower static broadening but falls below the value of QD B at tens of μs as a result of the larger total broadening. Note that the long time differences accessed and quantified here cannot be reached by standard HOM measurements due to eventually dominant fiber absorption at the necessary length (e.g. a delay of $200\,\mu$s in $40\,\mathrm{km}$ fiber corresponds to $> 130\,\mathrm{dB}$ loss at $850\,\mathrm{nm}$) ruling out the acquisition of correlation measurements in a reasonable time.

So far, the considered timescales contain the individual diffusive broadening of the lines L and R. Beyond that, a local charge trap induces a jump between the lines for both QDs. This dynamics can be identified in the long-term correlations, which is shown in Fig. 5.10a using a coarse binning due to computation limitation. After the individual lines have lost their correlations completely (the time scales considered in Fig. 5.9), a second decay with time constant $\tau_{\mathrm{LR}} \sim 7\,\mathrm{ms}$ is apparent (see Fig. 5.10a), fitting well to exponential decays and thereby revealing a telegraph noise behavior [143]. The stronger reduction of the correlations in the jump regime for QD A is originated in the larger intensity disparity between L and R (1:9) when compared to QD B (1:1.5) [144].

The present two-fold composition of timescale for the broadening dynamics has recently been observed for a biexciton-exciton cascade in an InGaAs QD under resonant two-photon excitation, too [137]. However, thanks to the dispersive mapping which provides the spectral information with absolute frequency reference, we are able to identify the regime of diffusion of a single line and its full expansion prior to the jump dynamics (indicated by the dashed line in Fig. 5.10a).

It is worth noting that both line jumps and spectral diffusion related to charge carrier noise, possess additional signatures in the intensity

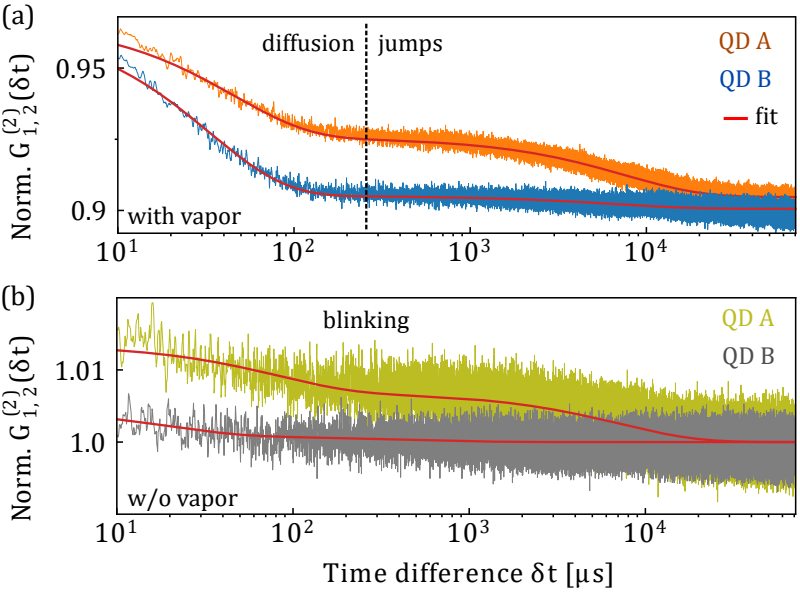

Figure 5.10. (a), Normalized photon-correlation after the vapor with a binning of 100 ns and smoothing for the peak repetition. Red curves are exponential fits with two decay constants. The two regimes of correlation reduction are indicated with a dashed line. (b), Normalized photon-correlation without the vapor.

correlation measurements without the vapor (Fig. 5.10b). This is observed as blinking at comparable timescales ($80\pm5\,\mu$s & 7.1 ± 0.1 ms for QD A and $20\pm5\,\mu$s for QD B) that arise due to charging or discharging of the QD inhibiting its re-excitation. We thus reveal the common origin of fluorescence intermittancy [145] and emission frequency diffusion under resonant π-pulse excitation. This implies that the reduction of charge traps during the sample growth is of key importance for both continuous emission and a narrow spectrum that eventually enables scalable quantum information technologies.

Discussion

Slow-light photon-correlation spectroscopy has been established as a method to reveal dynamics of emission line broadening by probing the photons of the charged exciton recombination in single QDs. The broadening is unveiled to consist of a static part that reflects phonon-induced broadening of the ZPL, a diffusive part that reflects charge and spin noise, and a part of Stark-shift induced discrete line jumps which reflects the occupation state of a local charge trap. The method is most useful for on-demand emitters, as it allows to investigate the photons under realistic conditions of excitation, in stark contrast to laser probes [52, 131]. Using this method, we have been enabled to identify the Ornstein-Uhlenbeck process as a suitable model to describe QD's spectral diffusion. The often utilized non-resonant laser initialization of a QD state [98, 146] turns out to accelerate fluctuations which can be related to charge noise of continuously generated charge carriers. The timescales disclosed for the different fluctuations in the micro- and milliseconds bring together the reports revealed by direct HOM visibility measurements [94, 96] and weak resonant probes [52, 53], showing their shortcomings but advancement of the present study.

While both the interferometric photon-correlation Fourier spectroscopy [136] and the presented method allow access to dynamics from, in principle, excitation state's lifetime to the stationary limit, the former poses less stringency on the probed wavelength while the latter necessitates only one correlation measurement. This can facilitate a tremendous ease for quantum emitters since count rates are often still an issue. Furthermore, the perspective of on-chip integration and miniaturization [105, 118, 119] is promising for future sustainability of the slow-light based method.

Assessing performances for quantum optical applications by rather straightforward photon correlation is a major achievement, such that the presented characterization of two-photon interference up to the stationary limit of diffusion at $250\,\mu$s extends the probed time scales by an order of magnitude compared to literature [95, 96].

However, this reveals also the need for controlling line broadening mechanisms to keep indistinguishability of photons high.
With this regard, successful shielding of nuclear spin fluctuations have been demonstrated by application of external magnetic field [125] in Faraday configuration. Additional optical control such as coherent population trapping can induce nuclear spin cooling [147], while QD's locking to a laser can be reached simply by dynamic nuclear spin polarization [126] induced by continuous resonant excitation. As for charge noise, high quality growth appears to be the major prerequisite. In addition, charge coupled devices have shown active stabilization of QD transitions by feedback on Rayleigh scattering or phonon side bands [148,149]. Finally, coupling QDs to micro-cavities in the regime of Purcell enhancement helps to keep indistinguishability high [85]. The lifetime reduction implies a natural broadening that often reaches more than an order of magnitude which diminishes the relative impact of frequency fluctuations [79].

5.3 Cs-vapor delay line for one- and two-photon Fock-states

A straightforward scheme to delay light is given in an optical cavity by multiples of the round trip time. Via polarization switching at a polarization beam splitter, light is released in and out of the cavity. Using this scheme delays of about a microsecond for one and two-photon Fock-states have been realized with corresponding 100 round trips [150]. While the photon number state fidelity shrinks with each round trip (vacuum component increases), the wavepacket distortion is ideally negligible. However, number of round trips for a significant delay increases with cavity miniaturization posing tight requirements for device losses.

Alkali vapors allow mapping of a light state into a long-lived collective state of the atomic ensemble [20], from where the stored light can be retrieved, for specific configurations, after the enormous waiting time of a second [31]. The majority of attempts utilize electromagnetically-induced transparency [151], where writing and reading are controlled via pulses. This allows a continuous on-demand variation of the delay for retrieving back the stored light state. However, the strength of control pulses induce noise photons via four-wave mixing and Raman transitions degrading the stored quantum state, while the small detuning of transitions further challenge filtering.

Despite attempts to make this scheme suitable for broadband QD photons [30], a realization remains so far elusive. An alternative scheme was introduced by a Raman memory with off resonant control and signal fields accepting GHz bandwidth photon storage, as successfully demonstrated for a parametric down conversion source [152]. However, this scheme encounters similar challenges due to an even stronger control field.

The aforementioned troubles can be circumvented by storing light

This section is reproduced in parts from:
H. Vural et al., PRB **103**, 195304 (2021) ©2021 American Physical Society
H. Vural et al., Optica **5**, 367-373 (2018) ©2018 Optical Society of America

in the excited state via a ladder scheme, as has been realized in rubidium [153] and cesium vapor [154]. Being noise free, this scheme however is ultimately limited by the much shorter coherences of the excited states. For the chosen orbital transitions in Rb the experimental and theoretical study yields about 100 ns of efficient storage time, while this was about 5 ns for the chosen Cs transitions.
Another approach that can accept large bandwidth storage is realized by a photon-echo based scheme in ion-doped rare-earth crystals [155]. For that, the inhomogeneously broadened absorption profile of an ensemble of ions is tailored to an atomic frequency comb. An absorbed signal is than released as an echo after a storage time determined by the inverse of the comb spacing. This scheme allows multi-mode storage in the time-bin which has also been demonstrated with QD photons [156]. Having shown high fidelity storage of time-bin entangled photons [157], this scheme lacks the on-demand operation capability.

The attempt to use the slow-light effect in a medium for realizing a delay line is obvious. Among other slow light media [60,104,105], the hyperfine-splitted D transitions of alkali vapor present an attractive choice for this purpose, especially with the restriction to GHz bandwidth. As already indicated, the presence of absorption line pairs render the refractive index profile between them almost to a linear function. This results in close to constant group velocity allowing to realize a 'low distortion' delay line. So far, laser pulses [158] or non-resonantly generated QD photons [36, 37] have been delayed in Cs vapor. Here, we use the pure single-photon emission of a QD to perform a delay line for one- and two-photon Fock-states, while monitoring the fidelity of the transmitted quantum states in the photon number basis.

5.3.1 Delaying one-photon Fock-states

The experimental setup to measure simultaneously the slow-light induced delay of the emission of a QD and the photon statistics of the transmitted emission is shown in Fig. 5.11. The single-photon

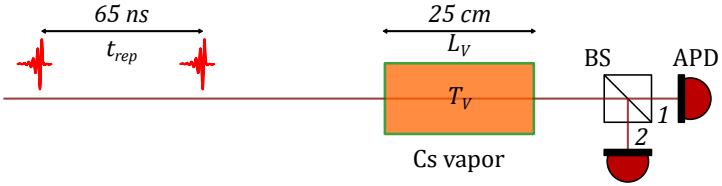

Figure 5.11. Single-photon delay line and setup to probe second-order coherence of delayed photons. TCSPC and $G^{(2)}_{1,2}$ are measured simultaneously. Laser repetition time t_{rep} and vapor cell length L_V are fixed, vapor temperature T_V is variable.

emission under resonant π-pulse excitation is directed through the vapor cell of length $L_V = 25\,\text{cm}$ where a variable vapor temperature T_V provides a tuning knob for the vapor response and hence the group index. Since we aim at maximizing achievable vapor-induced delays Δt_V, the laser repetition period is increased above expected delays to $t_{rep} = 65\,\text{ns}$ by exploiting a pulse picker. The operation is performed at the center of the Cs-D_1 lines where pulse distortion is minimal (see Fig. 2.2, Fig. 5.1 and Fig. 5.2). Measuring TCSPC allows to investigate the temporal domain and acquired the delay as in the previous sections. By simultaneous acquisition of the correlation $G^{(2)}_{1,2}$, any affect of vapor interaction on the purity of emitted one-photon Fock-states $|1\rangle$-state is probed.

Fig. 5.12 shows the experimental results obtained for QD C. From top to bottom, the vapor temperature is increased (see inset) which leads to a temporal delay Δt_V of detection times due to reduced velocity in the vapor. Following the theoretical description in section 5.1, the experimental data are excellently reproduced. The acquired delays at $T_V = 76.2\,^\circ\text{C}$, $114.44\,^\circ\text{C}$, $123.9\,^\circ\text{C}$ and $133.42\,^\circ\text{C}$ are closely described by the expected exponential behavior, reaching a group index $n_g(\omega) \geq 33$ and large fractional delays with $\Delta t_V/\tau > 50$ for the highest temperature. Significantly, delaying is achieved for almost all transmitted photons, with less than 1% of undelayed fraction stemming from photons at the wings of the Gaussian emission spectrum.

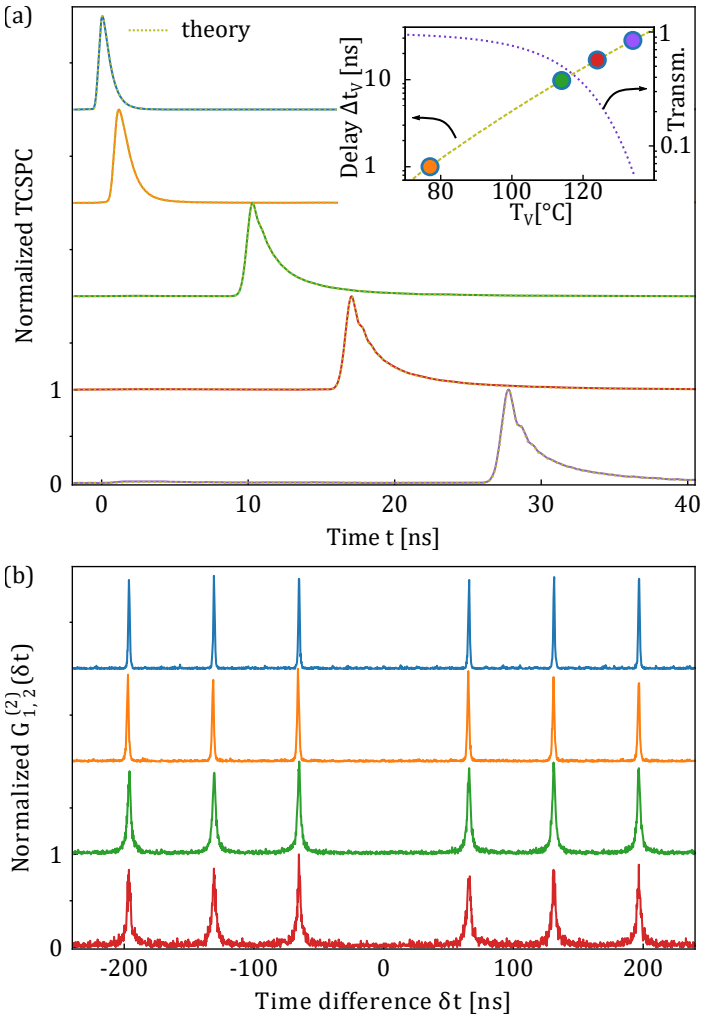

Figure 5.12. (a), TCSPC measurements at various vapor temperatures $T_V = 76.2\,°C$, $114.44\,°C$, $123.9\,°C$ and $133.42\,°C$ for QD C (lines) and theoretical predictions (dashed yellow). Inset: achieved vapor-induced delays Δt_V and corresponding vapor transmission. (b), Second-order coherence of delayed photons at various T_V. The color code corresponds with (a).

Accompanied with increasing delays Δt_V, the stronger dispersion in the vapor induces drastic pulse distortion, which we made useful for slow-light spectroscopy in the previous sections. However, as far as synchronization of signals by the vapor delay is concerned, this will lead to a reduction of maximal operation rates.

Fig. 5.12b depicts the simultaneously acquired photon statistics, except for the highest vapor temperature where tremendous absorption (see inset) prevents the acquisition of a correlation measurement in a reasonable integration time. The present peaks are separated by the excitation repetition period and display the increased temporal broadening with the temperature and a reduced signal-to-noise ratio due to the reduction in the rate of transmitted photons. For all temperatures and acquired delays, the single-photon nature is found to be preserved, as signified by the absence of coincidences amounting to a normalized value of $g^{(2)}_{1,2}(0) = 0.013 \pm 0.007$. In contrast to optical-controlled delay lines, this scheme inherently avoids any excitation in the vapor, thus any source of noise that may corrupt the photon statistics is absent. While this result may be rather obvious, it is of greater interest to study the effect of vapor-light interaction on a multi-photon state, as is performed in the following.

5.3.2 Slow-light of two-photon Fock-states

Higher number (N>1) path-entangled N00N-states have attracted attention in recent years, owing to the possibility of interferometry with superresolution [17,19,89]. Of particular importance is the possibility to overcome the shot-noise limit, referred to as supersensitivity and thereby to approach the Heisenberg-limit of interferometric phase estimation [18]. Utilizing HOM interference, single and indistinguishable photons can be used to prepare a 2002-state as has been demonstrated with QD photons [19].

So far, the delay of the two-photon Fock-state $|2\rangle$ was realized only in an optical cavity [150], while a 2002-state of narrow-bandwidth photons has been stored in cold atoms [159]. Here, we investigate the impact of the slow-light effect on the two-photon Fock-state by

probing the acquired delay and second-order coherence after interaction with the vapor. The generation and investigation of the $|2\rangle$-state follows the framework that was introduced in section 4.1.3.

Experimental setup

The experimental setup to delay two-photon Fock-states $|2\rangle$ is shown in Fig. 5.13. The operation is performed at the center of the Cs-D_1 lines with the vapor cell of length $L_V = 10\,\text{cm}$ that is kept at $T_V = 105\,^\circ\text{C}$. At these conditions, the speed of light is reduced by about an order of magnitude $n_g(\omega) \geq 7.8$ with simultaneous vapor transmission exceeding 90 %. The emission of QD A under resonant π-pulse excitation is directed into a HOM setup with the doubled laser repetition period of $t_{rep} = 6.5\,\text{ns}$. As discussed in section 4.1.3 a path-entangled 2002-state is generated upon successful HOM interference. The isolated consideration of path 5 projects out a $|2\rangle$-state, which is propagated through the Cs vapor and validated by a correlation measurement after BS_2. By means of the correlation $G^{(2)}_{7,8}$, the fidelity of the transmitted state $|1\chi_1^{L_V;5}, 1\chi_2^{L_V;5}\rangle_{out}$ to the $|2\rangle$-state is investigated. In section 4.1.3, we have seen that the fidelity without any vapor interaction is given by the HOM interference visibility as observed through increased coincidences.

To investigate the acquired vapor-induced delay Δt_V and impact of the slow-light effect on the temporal domain, time-correlated single-photon counting postselected on a coincidence (TCSPCp) event after BS_2 is performed. An event within the central coincidence peak heralds the arrival of a photon pair, upon this, one APD click is correlated to the excitation laser pulse.

Theoretical basics of TCSPCp

To gain an insight into the postselected TCSPCp at the output ports (7 & 8) of BS_2, we consider two parallelly polarized photons that have hit BS_1 simultaneously from different ports and subsequently propagated through the vapor. The state $|1\chi_1^{L_V;5}, 1\chi_2^{L_V;5}\rangle_{out}$ after

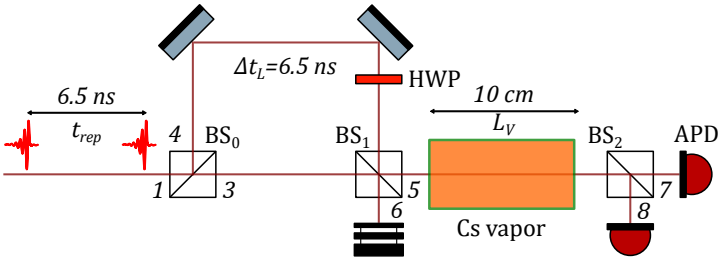

Figure 5.13. Experimental setup to generate two-photon Fock-states, investigate their fidelity by second-order coherence and to verify their delay by postselected TCSPC.

the vapor transforms at BS_2 to take the (unnormalized) form: $|1\chi_1^{L_V;7}, 1\chi_2^{L_V;8}\rangle + |1\chi_1^{L_V;8}, 1\chi_2^{L_V;7}\rangle + i|1\chi_1^{L_V;7}, 1\chi_2^{L_V;7}\rangle - i|1\chi_1^{L_V;8}, 1\chi_2^{L_V;8}\rangle$. The subscript i of $\chi_i^{j;k}$ indicates the carrier frequency, the superscript j before the semicolon indicates the propagation length in the Cs vapor and k marks the spatial mode (see Eq. (2.7) and Eq. (2.12)). TCSPCp detects the intensity of a photon e.g. at port 7 only for a coincidence event, i.e. under the consideration of the first two terms only, disregarding the last two. This leads to:

$$\begin{aligned}
&|\langle 0|\hat{a}_7(t)\left(|1\chi_1^{L_V;7}, 1\chi_2^{L_V;8}\rangle + |1\chi_1^{L_V;8}, 1\chi_2^{L_V;7}\rangle\right)|^2 \\
=&|\chi_1^{L_V}(t)|^2\langle 1\chi_2^{L_V;8}|1\chi_2^{L_V;8}\rangle + |\chi_2^{L_V}(t)|^2\langle 1\chi_1^{L_V;8}|1\chi_1^{L_V;8}\rangle \\
+&\chi_1^{*L_V}(t)\chi_2^{L_V}(t)\langle 1\chi_2^{L_V;8}|1\chi_1^{L_V;8}\rangle + \chi_2^{*L_V}(t)\chi_1^{L_V}(t)\langle 1\chi_1^{L_V;8}|1\chi_2^{L_V;8}\rangle.
\end{aligned} \tag{5.10}$$

Eq. (5.10) displays intensities that are weighted by the other photon respectively, and an interference term in the second line. To gain an intuition for this result, the analytic expression is examined, where the vapor is disregarded and a *free space* propagation is considered. Note, that the photonic states are normalized in this case but are not orthogonal for different carrier frequencies.

In fact $\langle 1\chi_2^{0;8}|1\chi_1^{0;8}\rangle = \frac{i}{i+\tau\delta\omega}$, where $\delta\omega = \omega_2 - \omega_1$.
With $\chi_1^{*0}(t)\chi_2^0(t) = \frac{1}{\tau}\Theta(t)e^{-t/\tau}e^{-i\delta\omega t}$, the interference part yields:

$$\begin{aligned} & 2\frac{1}{\tau}\Theta(t)e^{-t/\tau}\left(\frac{1}{1+\tau^2\delta\omega^2}\cos(\delta\omega\cdot t) + \frac{\tau\delta\omega}{1+\tau^2\delta\omega^2}\sin(\delta\omega\cdot t)\right) \\ =& 2\frac{1}{\tau}\Theta(t)e^{-t/\tau}\left(\frac{1}{\sqrt{1+\delta\omega^2/\Delta\omega_{FL}^2}}\sin(\delta\omega\cdot t + \arctan(\Delta\omega_{FL}/\delta\omega))\right), \end{aligned} \tag{5.11}$$

where the Fourier-limited line width $\Delta\omega_{FL} = \tau^{-1}$ was used. The interference part is an exponentially damped (due to the photon shape) sinusoidal oscillation, where the beat note follows the dependency given for the second-order coherence (see Eq. (2.19a)). Here however, with increasing carrier frequency difference of the two photons not only the beat frequency is increased but also the oscillation amplitude is decreased and the phase is shifted, as depicted in Fig. 5.14b.

The total result of TCSPCp is shown in Fig. 5.14a. The interference part adds up to the photonic wavepackets' temporal profiles, while $\delta\omega$ determines the overall area of TCSPCp. This is not unexpected since a higher photon wavepacket overlap given by the HOM visibility $V_{\mathrm{HOM}}(\delta\omega) = 1 + \delta\omega^2/\Delta\omega_{FL}^2$ increases the number of coincidence detection upon which the postselection is based. The inset in Fig. 5.14a compares all the TCSPCp normalized on their respective maxima, that reveals only slight deviation of signals from the exponential decay, which is exactly reproduced when two identical photons are considered.

In Fig. 5.14c, the impact of Gaussian line broadening on the TCSPCp signal is simulated and compared to the exponential decay of the standard TCSPC (dashed lines). Indeed, the overall TCSPCp is very close to the exponential decay when normalized to their maxima respectively, only indicating the interference by a slightly surpassing of the signal in earlier times and fall down in the later times.
In Fig. 5.14d, the simulation is performed with the Cs vapor in the path for parameters as was used for Fig. 5.2. This time, the TCSPCp

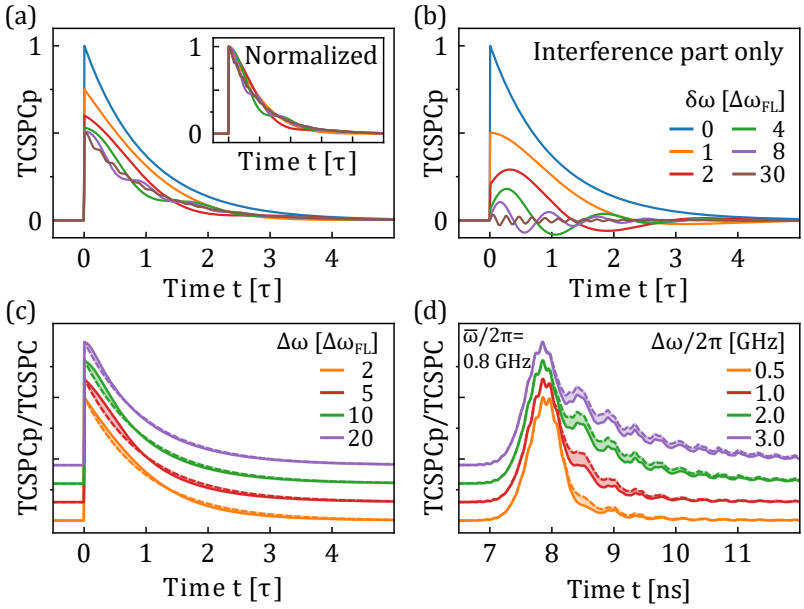

Figure 5.14. (a), Simulation of time-correlated single-photon counting postselected on a coincidence event (TCSPCp) after BS_2, depicted for various carrier frequency differences $\delta\omega$ of the two photons in units of the Fourier-limited line width $\Delta\omega_{FL}$. Inset compares the time domains normalized on their respective maxima. Legend and color code as in (b). (b) The interference part as in Eq. (5.11) which is the origin of the beats. (c), Comparison of standard TCSPC (dashed line) to TCSPCp (solid line) signal for various Gaussian broadened emission with FWHM $\Delta\omega$. Shaded areas highlight the difference between both signals. Curves are stacked for comparison. TCSPCp starts always above the TCSPC signal but evolves to lie below it. (d), Simulation of TCSPC and TCSPCp signals of Gaussian broadened spectra with the center of emission at $\bar{\omega}$ with the Cs vapor in path. Simulation parameters as for Fig.5.2. TCSPCp after the vapor lies below the TCSPC curve, highlighted by the shaded areas.

signals clearly lie lower than the TCSPC signals. Note, although the interference induces a narrower temporal profile for TCSPCp compared to TCSPC for the same broadening, the impact of spectral diffusion dynamics is almost not apparent (therefore not depicted). Thus, TCPSCp is not suitable to study the spectral diffusion as has been the case with the slow-light photon-correlation spectroscopy in the previous section, however it may at least be indicative for the propagation and transmission of two-photon Fock-states with reduced fidelity through the Cs vapor.

Delaying the two-photon Fock-states

Fig. 5.15a shows the correlation histogram of QD A after directing one output of the HOM interferometer through the Cs vapor. The qualitative pattern follows the correlations without the vapor (see Fig. 4.4). For perpendicular polarized photons at BS_1, the central coincidence peak amounts to half the value of the outermost peaks, as expected for non-interfering photons. In the parallel polarized case, two-photon interference at BS_1 bunches photon pairs in the outputs such that the coincidence rate rises. The visibility, calculated by comparing the central coincidence areas, amounts to the same value 0.53 ± 0.05 as for the experiment without the vapor in path 5. This shows that the fidelity of the two-photon state is not affected by the interaction with the vapor, despite the induced absorption and temporal broadening. The broadening helps to reduce the effect of detector jitter on the data such that the narrower profile of the coincidence peak and its theoretical maximum are closer resolved compared to the case without the vapor (see Fig. 2.5 and Fig. 4.4). Having the conformation that the central coincidence peak indeed includes the generated $|2\rangle$-state, we study now its temporal delay.

Fig. 5.15b depicts TCSPC* (the asterisk shall indicate that TCSPC is not performed in the standard way, but after the HOM interferometer and an additional beam splitter) and TCSPCp which is heralded upon an event in the highlighted central coincidence peak in Fig. 5.15a. The upper panel shows both signals in the absence

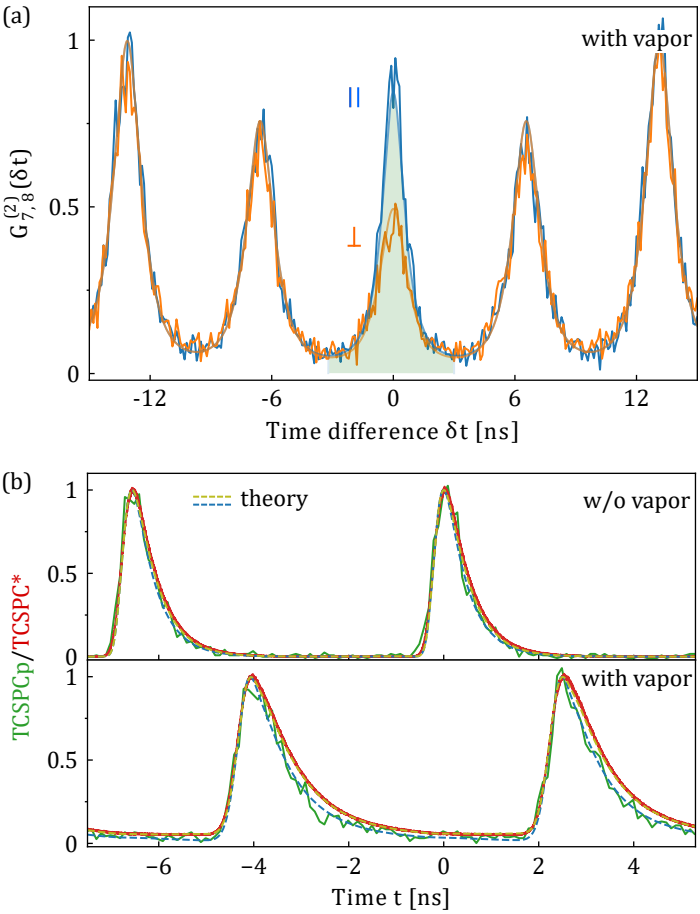

Figure 5.15. (a), Second-order coherence at the output ports of BS_2 following HOM interferometer output port 5 and interaction with the Cs vapor for parallel (||) and perpendicular (⊥) photon inputs. Light solid lines on top of data are theory curves. The events within the highlighted central coincidence peak are used for heralding TCSPCp. (b) Time domain signals of single detections at port 7, TCSPC*, compared to postselection on a coincidence event, TCSPCp. Dashed curves are simulations on account of the known spectral diffusion.

of a vapor. They overlap in the time domain, while the anticipated modulated temporal profile of TCSPCp remains unresolved due to statistical uncertainty in each bin of 100 ps width, as the heralding on a coincidence event causes a severe limitation of acquired data. The lower panel compares the case with Cs vapor placed into the path. Both signals are now delayed by about $\Delta t_V \approx 3$ ns, while the narrower TCSPCp is resolved thanks to the additional dispersion of the vapor. The delay amounts to more than 5 times the decay constant and is large enough to shift the time domain almost completely out of overlap to the undelayed signals. Theory curves for TCSPC of one-photon Fock-states and TCSPCp of photons after HOM interference and vapor interaction describe the data faithfully, although TCSPC* integrates all signals with contribution of interfering photons, too. The previously characterized spectral diffusion process is also accounted for in the simulations. Note, that the narrow time domain for photon pairs on which basis a distinction of photonic states can be made, fails when a Fourier-limited emission is considered. In this case, the correlation measurements at a beam splitter are a mandatory tool to distinguish between the Fock-states.

Discussion

We have demonstrated that the slow-light effect in a Cs vapor is suitable to realize a delay line for basic Fock-states. The acquired vapor-induced delays Δt_V amount to multiples of the initial pulse length allowing the vapor to be a tool for synchronization of signals among different time bin slots. In particular, this would enable slow-light Fourier-spectroscopy [110] with vapor transmission around 90%. Significantly, the quantum state in the photon number basis is completely preserved upon the interaction with the vapor, as experimentally verified for N=1 and 2. The combination of slow-light medium and higher number Fock-state (N=2) can open new perspectives in interferometry, reinforcing the enhancement in spectral phase sensitivity provided by the slow-light effect [109–111] with the enabling feature of the two-photon Fock-state for phase measurements with

superresolution and supersensitivity [19, 160].
The maximum fractional delay of above 50 ($\Delta t_V \approx 27\,\mathrm{ns}$) based on the slow-light effect marks a record value for a wide-bandwidth one-photon Fock-state. However, reaching delays beyond that is not possible with the present scheme, as its strength is paid in terms of absorption. This limitation together with the strong dispersion-induced pulse distortion can potentially be circumvented by the other delay and storage techniques mentioned in the introduction of this section.

Note, that all the GHz bandwidth storage schemes of the present day have shown storage times well below a microsecond, often below the fractional delay achieved in this work. Most significantly, the impact of pulse distortion on indistinguishability of wavepackets is an outstanding question that has not been tackled yet. In the following section, this question is addressed for the present Cs-vapor delay line.

5.4 Two-photon interference in the hybrid system

In section 5.2, we have determined that the HOM interference visibility for short time differences of successively emitted photons is given by a static Gaussian broadening. In section 5.1 photon-vapor interaction showed strong differences in temporal shapes for distinct carrier frequencies. This suggests an additional impact on photon indistinguishability, despite the preserved fidelity in the photon number basis. To shed light on this, in the following, two complementary experiments of two-photon interference are studied. In the first one, both photons are first delayed upon interaction with the Cs vapor, such that a subsequent quantum interference experiment sheds light on any decoherence arising from the interaction with the vapor. In the second experiment, only one photon is interacted with the vapor and synchronized to the other bare photon by the slow-light induced delay. In this case, the impact of pulse distortion on the indistinguishability is probed and feasibility of possible networking scenarios with vapor synchronization is evaluated.

5.4.1 Interference of photons after interaction with the Cs vapor

Fig. 5.16 shows the experimental setup to probe the HOM interference of single QD photons after their interaction with the vapor. The utilized HOM interferometer has a fixed arm length difference that amounts to $\Delta t_L = 4.3\,\mathrm{ns}$, for which a double pulse sequence is to be used to bring successive photons at BS_1 to interfere. All emitted photons under resonant π-pulse excitation are directed through the vapor of variable temperature, such that strength of dispersion and thus vapor-induced delay can be varied. By means of the second-order

This section is reproduced in parts from:
H. Vural et al., Optica **5**, 367-373 (2018) ©2018 Optical Society of America

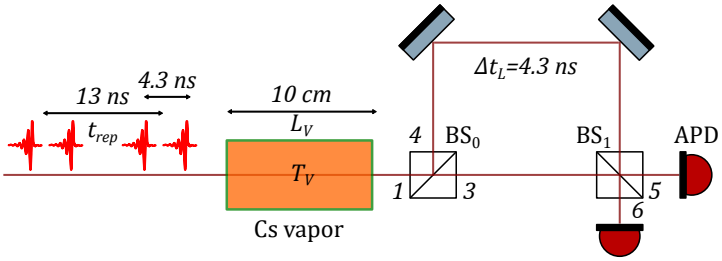

Figure 5.16. Experimental setup to interact the QD photons with the Cs vapor prior to their HOM interference. A double-pulse sequence to generate photons of 4.3 ns separation every repetition period t_{rep} is used. The vapor temperature T_V is variable to probe several vapor-induced delays Δt_V prior to HOM experiment. Second-order coherence after HOM interference is measured after beam splitter BS$_1$.

coherence given by the correlations $G^{(2)}_{5,6}$, the indistinguishability of successive photons are investigated.

Fig. 5.17a shows the histogram of HOM interference for the photons of QD C when a prior vapor-induced delay of $\Delta t_V = 2.5\,\text{ns}$ is introduced. The utilized double pulses imply a bit different pulse pattern with regard to previous experiments, however the central coincidence peak still testifies the interference. For parallel polarized photons the coincidences are strongly reduced while the dip in the central peak indicates the presence of a static broadening. In a series of experiments, the vapor temperature is increased and thus the acquired delays prior to the HOM interference. For all studied delays an unchanged visibility of $V_{\text{HOM}} = 0.52 \pm 0.04$ is found, despite increasing temporal broadening of peaks. This is further verified by simulations that take the corresponding spectral diffusion into account ($\Delta\omega_{ph}/2\pi = 0.9\,\text{GHz}$ FWHM of the static Gaussian jitter and $\Delta\omega/2\pi = 3.0\,\text{GHz}$ FWHM of the stationary Gaussian). From here, one can conclude that the interaction of photons with the vapor does not add any observable dephasing to the photon wavepackets.

Fig. 5.17b depicts the histogram for a vapor delay of $\Delta t_V = 5.8\,\text{ns}$

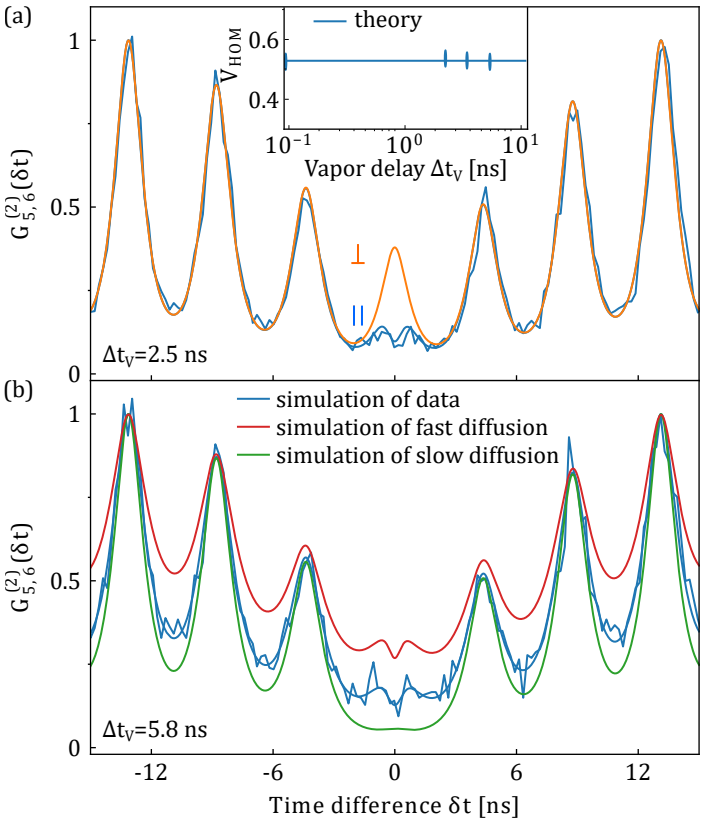

Figure 5.17. (a), Second-order coherence at the output ports 5 & 6 of the HOM interferometer after the vapor-induced delay $\Delta t_V = 2.5\,\text{ns}$ has been acquired for all photons. Data are for the case of parallel $\parallel$ polarized photons. Theory curves for both parallel and perpendicular $\perp$ polarization account for the spectral diffusion process. Inset: Points are measured HOM interference visibilities V_{HOM} after various vapor delays Δt_V. Solid line is the theoretical expected result based on the bare visibility of $V_{\text{HOM}} = 0.52$ and a corresponding Gaussian jitter of $\Delta\omega_{ph}/2\pi = 0.9\,\text{GHz}$. (b) Second-order coherence after a vapor-induced delay of $\Delta t_V = 5.8\,\text{ns}$. Theory curves for three cases: the proper diffusion process fitting the data and hypothetical limiting cases for a very slow and very fast spectral diffusion.

prior to the HOM interference. Alongside with the data, theory curves are presented, that compare the proper spectral diffusion to hypothetical cases where the inhomogeneous broadening of the QD is assumed to evolve immediately to its full extend ($\tau_c \mapsto 0$, fast diffusion limit) or where the emission contains no static broadening and successively emitted photons are indistinguishable ($\tau_c \gg t_{rep}$, slow diffusion limit). The former limit leads to much stronger broadened peaks in the histogram and strongly deviate from the data. Moreover, the HOM visibility is 0.2 in this case. In the latter limit, HOM visibility approaches unity, while the peaks are clearly narrower than the data. Hence, the interconnection of spectral diffusion, HOM visibility and unique temporal broadening of correlation peaks after the slow-light medium is once again revealed. Especially, this provides another proof of the validity of slow-light photon-correlation experiments of section 5.2, demonstrating the interconnection this time in a single measurement for a photon emission time difference of 4.3 ns.

A last comment shall address the rather surprising outcome, that HOM visibility remains unchanged upon interaction with the vapor, although the probed emission spectrum is broadened which should imply an additional distinguishability in time domain for two photons of different carrier frequencies (see Fig. 5.1 and Fig. 5.4). With this regard, one should keep in mind that the presented experiments probe an emission time difference of only 4.3 ns, which implies a probed line width of $\Delta\omega_{ph}/2\pi = 0.9\,\mathrm{GHz}$ corresponding to the static Gaussian broadening. However, the main reason for the conserved interference can be seen in the strong dependence of HOM visibility on the carrier frequency difference of interfering photons, but a rather weak dependence on the temporal domain. For example, two photons with the same decay constants that differ in carrier frequencies by one Fourier-limited line width yield only a low visibility of $V_{\mathrm{HOM}} = 0.5$. In contrast, the interference visibility of two photons with the same carrier frequencies but a decay constant difference of factor two (i.e. doubled line width) reduces only weakly to about $V_{\mathrm{HOM}} \approx 0.9$ [161]. The temporal domain of two photons to differ strongly within the frame of our Cs vapor dispersion is only given for photons that al-

ready differ in their carrier frequencies by such an amount, that the temporal distinguishability does not play a role anymore. In the following therefore, bare exponentially decaying photons will be interfered with vapor-delayed ones to investigate the direct impact of pulse distortion on the indistinguishability.

5.4.2 Interference of interacted and non-interacted photons

Fig. 5.18a shows the experimental setup to probe the HOM interference of a photon after its interaction with the vapor with a photon that has not interacted. The utilized HOM interferometer is chosen to compensate the time difference of successive photons that amounts to 4.3 ns, in parts by a free space propagation Δt_L and in parts with the vapor-induced delay Δt_V. The emitted photons under resonant π-pulse excitation are directed on a half-wave plate (HWP) which in combination with a polarization beam splitter (PBS) serves to adjust equal photon rates at BS_1. This helps to keep coincidence rate higher since the variable vapor delay, tuned by its temperature, modifies the transmission and reduces otherwise the coincidence probability. By means of second-order coherence given by the correlations $G^{(2)}_{5,6}$, the indistinguishability of successive photons is investigated. In this case however, the temporal domains at the inputs of BS_1 strongly differ, since photons of the upper path gets distorted, which pose the problem of temporal matching to maximize the interference visibility. By simulations, it turns out, that for the present QD spectral diffusion and vapor parameters in hand, overlapping the maxima of TCSPC signals of the distorted upper path and the exponential decay of the lower path is a reasonable choice.

Fig. 5.18b shows the histogram of HOM interference for the photons of QD C where vapor-induced delay amounts to $\Delta t_V = 1.7$ ns. For parallel polarized photons the coincidences are clearly reduced, however the visibility $V_{\mathrm{HOM}} = 0.38 \pm 0.06$ amounts to a lower value than before. For a higher vapor temperature and acquired vapor delay, the visibility further decreases. Interference of distorted photons

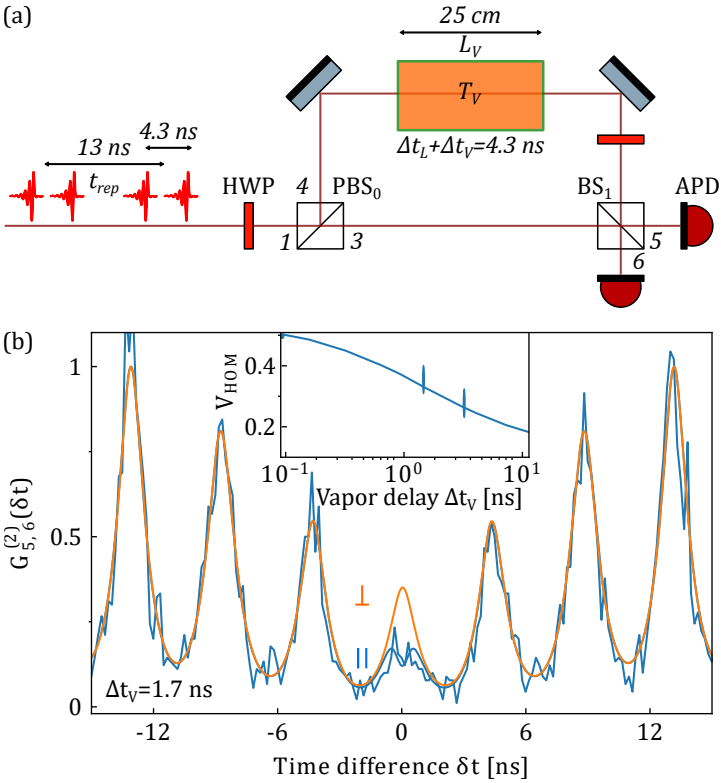

Figure 5.18. (a), Experimental setup of a HOM interferometer where synchronization of photons at BS_1 are partly induced by the vapor delay Δt_V and partly by free space propagation Δt_L. One of the interfering photons at BS_1 is affected by the slow-light medium, the other remains unaffected. (b), Second-order coherence at the output ports 5 & 6 of the HOM interferometer after the slow-light induced delay $\Delta t_V = 1.7$ ns has been acquired for synchronization. Data are for the case of parallel $\parallel$ polarized photons. Theory curves for both parallel and perpendicular $\perp$ polarization account for the spectral diffusion process. Inset: Points are measured HOM interference visibilities V_{HOM} after various vapor delays Δt_V for this interferometer constellation. Solid line is the theoretically expected curve under the present spectral diffusion process.

with exponential decays show a continuous drop of HOM visibility with increasing vapor delay. This is also verified by simulations that take the known spectral diffusion into account. Thus, although the interaction of photons with the vapor does not add any observable dephasing to the photon wavepackets, the introduced pulse distortion turns out to be a major obstacle, as the visibility reduces to half its initial value within a fractional delay of about five.

As synchronization within quantum information processing tasks is an important demand, in the following the potential of the present Cs-vapor delay line is benchmarked for the ideal case of Fourier-limited emitters. Note that, without the spectral broadening, the highest HOM visibility of two photons is obtained when cross-correlation of their wavepacket amplitudes are maximized. In the following simulations this is taken into account. Fig. 5.19a shows the HOM visibility and absorption over the acquired vapor delay for various wavepacket decay constants τ of exponentially decaying photons, which range from 1 ns, typical lifetime of bare InGaAs QD transitions, to 100 ps which results e.g. from Purcell enhancement in a micro-cavity structure. State-of-the art QD emitter widely exploit these structures to render inhomogeneous broadening insignificant and thereby to approach unity photon indistinguishability [16, 77, 96, 162].

With increasing vapor-induced delay Δt_V for one of the photons, the visibility drops for all curves rapidly within a few nanoseconds of vapor delay and continue to reduce slowly, while the absorption increases linearly up to 80 % to approach slowly unity. For smaller photon decay constants τ the drop of visibility is very strong and tend to completely vanish at the highest vapor delays, while the visibility remains high for the longer photon decay constants. In contrast, the absorption over Δt_V differs only insignificant among the various decay constants. A small τ corresponds with a large line width in the frequency domain, for which the vapor dispersion implies a stronger impact on pulse distortion. Thus, for the present delay line shortening the photon decay constant τ turns out to be detrimental.

For many applications, often the fractional delay $\Delta t_V/\tau$ is the figure

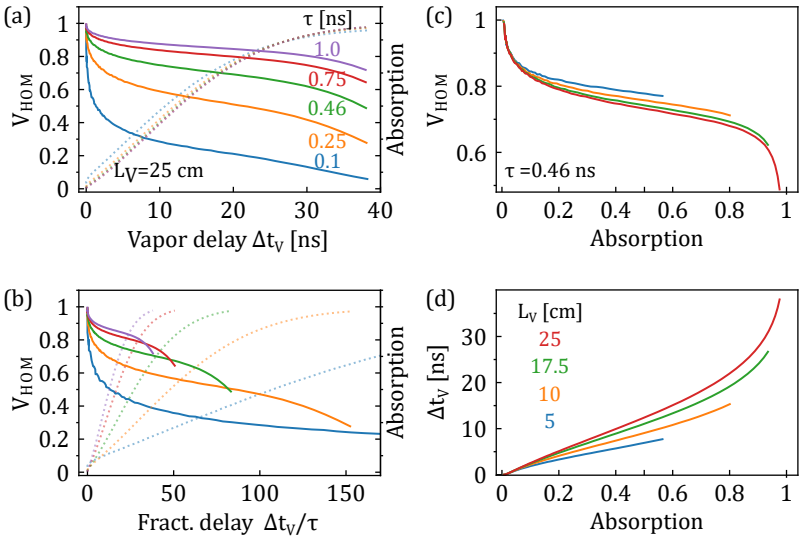

Figure 5.19. (a), Simulation of HOM visibilities V_{HOM} carried out for various decay times τ (solid lines) when the vapor-induced delay Δt_V is used for synchronization at the interfering beam splitter. The QD's emission is assumed to be Fourier-limited and the carrier frequency of the photons to match the point of vanishing group velocity dispersion for the least induced pulse distortion. Corresponding vapor absorption is shown in dashed lines. (b), Same results as in (a) over the fractional delay. Color code as in (a). (c), Simulation of HOM visibilities over the vapor absorption for various cell lengths L_V. Simulations are carried out for the decay constant of the experimentally investigated QD, $\tau = 0.46\,\mathrm{ns}$. Color code as in (d). (d), Acquired vapor delays over the vapor absorption for various cell lengths.

of merit rather than absolute delays [153]. Fig. 5.19b therefore depicts visibilities over the fractional delay. It is expected that a small τ reaches much higher fractional delays up to the point of complete vapor absorption. However even with regard to fractional delays, the visibility for smaller decay constants keep below the longer ones, reinforcing the aforementioned problem.

This issue poses not only a problem for slow-light based delay lines, but also for light-controlled storage schemes that rely on electromagnetically-induced transparency [151], as strong dispersion is created during the storage and retrieval processes [30]. It becomes clear that dispersion-based delay lines shall operate for fine tuning of small delays as far as quantum interference is concerned. For that, in Fig. 5.19c & d, we study up to a temperature of $T_V = 140\,^{\circ}\mathrm{C}$ whether the cell length of the Cs vapor can contribute to a significant advance. Fig. 5.19c depicts the visibility over vapor absorption for a fixed decay constant that matches to the one of QD C photons. For shorter cell length L_V, the absorption remains well below unity while only a slight increase of visibility is expected for the same absorption. However, in Fig. 5.19d one can see that this increment is connected to a lower vapor delay. Thus, the HOM visibility over the acquired vapor delay shows no dependence on the utilized vapor cell length (not shown, since all curves overlap). We can conclude, that except the limitation of delay imposed by a cut off vapor temperature, vapor cells of several centimeters show no advantage when compared to each other. However, with regard to optically-controlled storage schemes that incorporate dispersion, shorter cells are more suitable to keep absorption and pulse distortion minimal.

Discussion

The need for synchronization of quantum optical signals triggered a vast research field that is concerned about efficient storage of quantum optical states [20]. While the demand for ever faster information processing necessitates short pulses with corresponding larger spectral bandwidth, there is room for improvements with regard to sub-nanosecond and respective GHz bandwidth quantum memories. Until now, the impact of pulse distortion on quantum interference was not studied comprehensively for any storage scheme. The results achieved in this study constitutes a first attempt in this direction for a slow-light based alkali-vapor delay line. The experiments with all vapor-delayed photons indicate cautiously positive results through

conserved quantum interference visibilities that reveal preservation of photon wavepacket coherence in hot vapor for successive photons. However, the strong visibility reduction in case of the more application oriented scenario of the quantum interference of a single photon with a vapor-delayed one rises serious concerns about its applicability. This is particularly the case for applications where the temporal wavepacket plays a determining role after the storage, as is the case for quantum interference at a beam splitter. The presence of dispersion must be figured out for all other storage schemes and be diminished as far as possible. Notably, it is calculated that dispersion even in a telecommunication fiber can cause significant reduction of wavepacket overlap and quantum interference [92].

Pulse distortion arising from material dispersion turns out to be a weak spot especially within the frame of quantum optics, as classical pulse compensation methods are largely unsuitable for quantum states of light. That is why quantum-state preserving temporal and spectral shaping and compression techniques are being investigated, especially due to the need for combining different quantum systems of disparate bandwidth. Spectral and temporal pulse compression for ultra short (laser) pulses can be achieved with dispersive optical elements, filters and nonlinear techniques [163]. Electro-optic phase modulation has been successfully applied to create a time lens for compressing wide-bandwidth heralded single photons [164]. THz bandwidth photon wavepackets were compressed also via non-linear effects with tailored control pulses [165]. Longer pulses of MHz bandwidth can exploit the long coherence of trapped atoms and quantum cavity electrodynamics to provide temporal pulse shaping [166]. However, the present regime of pulse length from 100 ps to 1 ns of QD transitions is unexplored and remains a blind spot of these attempts. Eventually, it becomes clear that in addition to efficient wavelength conversion [92] photon pulse shaping will be a central topic for engineering future quantum technology solutions.

Chapter 6

Summary

The pathway to advanced quantum technological applications often includes hybrid quantum systems of matter mediated by quantum-states of light. This thesis examined a particular interface formed by a single semiconductor QD and Cs atoms in a hot vapor which is mediated by Fock-states of light. While the QD serves as an efficient single-photon emitter, alkali vapors are well known as storage media for classical light pulses.

Prior works on realizing a QD-alkali vapor interface have documented slowing down of the single-photon emission of QDs under incoherent excitation schemes. However, those schemes limit the efficiency of photon generation, generally display reduced single-photon purity and induce excessive frequency and timing jitter on the emitted photons. To be beneficial for advanced quantum implementations, ultrapure and highly indistinguishable photons have to be generated on-demand. By exploiting resonant excitation schemes numerous studies reported such an achievement.

To take a significant step closer to real-world implementations, in this work we utilized pulsed resonant excitation of single InGaAs QDs and thereby realized precisely timed emission of pure single and indistinguishable photons. The sample was engineered to emit light at a wavelength matching the Cs-D_1 transitions. This enabled extensive time-resolved studies of the optical and quantum-optical properties of the one- and two-photon Fock-states after interaction with a Cs vapor. By exploiting the slow-light effect, a delay line for both Fock-

states has been realized with high fractional delays, while the photon statistics was proven to be unchanged after the vapor. Moreover, the coherence preserving property of the slow-light effect has been proven in HOM interference measurements.

A major aspect of the studies in this work was related to the pulse distortion, that is induced on the photon wavepacket by the dispersion of the slow-light medium. On the one hand, via HOM measurements, the implications of pulse distortion for future quantum networks that rely on two-photon interference were investigated. On the other hand, we were able to exploit the essential connection between dispersion and specific pulse distortion for high-resolution time-domain spectroscopy. In particular, a novel technique based on slow-light photon-correlation has been established that has allowed to study the dynamics of spectral diffusion processes in QDs by investigating the emitted photons in the time domain.
In the following, the main results and conclusions are summarized.

On-demand pure single-photon generation
Pulsed resonant excitation is a promising excitation scheme to push semiconductor QD emission to its best performance. Using this technique, probabilistic QD state population and excessive dephasing, that results from non-resonant excitation of the surrounding matrix, are suppressed. Under resonant π-pulse excitation, we have generated pure single-photons on-demand from the charged exciton transition of single InGaAs QDs for their utilization in the interface with Cs atoms.
In power-dependent pulsed resonant excitation, the coherent excitation of the charged exciton state of QDs was demonstrated by observing clear Rabi oscillations. The peak excited-state population probability has been estimated to be ~ 0.75 at the π-pulse, while the emission into the zero-phonon line amounted to ~ 0.78, such that coherent photons have been generated with 60% efficiency. In addition to the efficient photon generation, the very high purity of the QD emission in the one-photon Fock-state has been confirmed by second-order coherence measurements. At the π-pulse, the nor-

malized intensity correlation yielded an effectively vanishing value of $g^{(2)}_{1,2}(0) = 0.014 \pm 0.006$ over all investigated QDs.
Alongside the high purity in the photon number basis, precisely timed photon emission has been verified. Both constitute salient features of the resonant excitation of QDs. Time-correlated single-photon counting on the zero-phonon line of the CX transitions showed a sharp wavepacket front and a mono-exponential decay, where a mean decay constant of $T_1 = 0.43 \pm 0.03\,\mathrm{ns}$ over the investigated QDs was extracted.
Besides these highly valuable properties of a two-level system, the impact of environmental fluctuations that couple to the QD transition has been identified. High-resolution spectra of the zero-phonon line displayed inhomogeneous Gaussian broadening up to one order of magnitude larger than the Fourier-limited line width of $\Delta\omega_{FL} = 0.37 \pm 0.05\,\mathrm{GHz}$. Moreover, a secondary line was often present in the spectra. The processes of line broadening constitute a major challenge for the usage of QD emitters in multi-photon and multi-source quantum implementations. The first step of improvements relies on the understanding of the processes behind the broadening under the π-pulse pumping: this has been enabled by the utilization of the present QD-Cs vapor interface.

Generation of the two-photon Fock-state using HOM interference

Both indistinguishability of the single-photons and successful generation of the two-photon Fock-state after interference at a beam splitter have been confirmed by utilizing the HOM effect. To allow the propagation of the two-photon state in the Cs vapor and its time-correlated detection, the usual HOM experiment has been extended. An additional beam splitter was placed at one output arm of the beam splitter, where the HOM interference took place. This allowed to verify the generation of two-photon Fock-states via the observation of increased coincidences at zero-delay in a second-order coherence measurement.

Before performing the actual experiment, the photon indistin-

guishability was benchmarked via the usual HOM experiment. As detected by a reduction of coincidences, the mean photon wavepacket overlap of interfering photons, which is given by the HOM visibility, has reached values up to $V_{\mathrm{HOM}} = 0.53 \pm 0.03$. In the extended experimental configuration the same visibility has been reproduced through increased coincidences at zero-delay and confirmed a fidelity of 53% of the generated two-photon state to the two-photon Fock-state. From the visibilities a coherence time of $T_2 \approx T_1 = 0.43\,\mathrm{ns}$ and an underlying Gaussian broadening of $\Delta\omega = 0.9\,\mathrm{GHz}$ FWHM is inferred. This line width (coherence time) is a factor of $3-4$ narrower (higher) than the emission line width (coherence time) of the total stationary QD spectrum. The unveiled discrepancy is usually encountered in solid-state quantum emitters and is caused by a slow spectral diffusion process.
In the literature, the high coherence of time-wise closely emitted photons from a single source has been exploited for multi-photon quantum implementations with fidelities close to unity. In contrast, for implementations with independent sources the total extent of broadening is a determining factor, for which high fidelity operation remains elusive. Here, a method that exploits the strong dispersion of the Cs vapor has been able to resolve the transition from high HOM visibilities for successively emitted photons (few nanoseconds apart) to the low visibilities expected from the broadened stationary emission spectra.

Studying QD spectral diffusion by slow-light photon-correlation spectroscopy
In this work a slow-light based spectroscopy technique has been introduced, through which the successful characterization of spectral diffusion dynamics of QDs has been demonstrated. In contrast to other techniques, here the diffusion dynamics is investigated directly on the emitted photons, enabling this type of study for a resonantly excited QD at the π-pulse.

So far, the strong dispersion over the Cs-D_1 lines has been used as a means to achieve the slow-light on photons that propagate through

the vapor. In addition to that, we have exploited the detuning-dependent unique pulse distortion of transmitted photons for mapping frequency domain to time domain. By this, a time-domain spectroscopy has been realized that is suitable to investigate GHz bandwidth broadening of QD spectra. In time-correlated single photon counting measurements of transmitted photons, the emission spectra of several QDs have been revealed. The excellent agreement to independently measured frequency-domain high-resolution spectra has demonstrated the applicability of the measurement principle. Moreover, spectral correlations of the QD's emission frequency has been investigated by the extension to a photon-correlation measurement of transmitted photons after the vapor interaction. The QDs' spectral diffusion yielded an incremental broadening of the correlation peaks with unique shapes at respective timescales. This has allowed to reveal the dynamics of spectral diffusion and to determine the temporal evolution of coherence and HOM visibility up to the stationary limit, all with a single second-order coherence measurement.

The results gained by the introduced method have enabled to identify the Ornstein-Uhlenbeck process as a suitable model to describe the spectral diffusion of QDs. The total line broadening has been unveiled to consist of three contributions: a static part, that reflects a phonon-induced broadening of the zero-phonon line and which is responsible for the non-unity HOM visibility at shortest time scales; a diffusive part that reflects spin and charge noise at $7\,\mu$s and $62\,\mu$s respectively for a QD under purely resonant excitation; and a part of Stark shift-induced discrete line jumps at 7.6 ms, which reflects the occupation state of a local charge trap. When utilizing non-resonant laser initialization as for another QD's charge state, a reduced single correlation time of $22\,\mu$s of the spectral diffusion is found which is dominated by fluctuations of the continuously generated charge carriers. The overall large noise amplitudes indicates that the QD sample, which is glued on top of a piezo-transducer, has a higher temperature than the anticipated 4 K. Correspondingly, there is potential for improvements in the sample growth to further reduce traps and excessive defects in the vicinity of QDs.

The timescales disclosed for the different fluctuations in the micro- and milliseconds are bridging the gap between reported timescales in direct HOM visibility measurements and weak resonant laser probes. Thanks to this advancement, the overall performance of a quantum emitter for quantum optical applications has been assessed by straightforward photon-correlations. This has been achieved by inferring the two-photon interference visibilities of consecutive photons up to the stationary limit of the diffusion processes. Knowing the timescales and noise amplitudes is useful for tailoring active and passive methods for controlling the line broadening that are intended to keep indistinguishability of the photon stream high.

Cs-vapor delay line for quantum-states of light
Besides being exploited for spectroscopy, the strong dispersion of the vapor at the Cs-D_1 lines and corresponding high group index $n_g(\omega)$ have been used to form a delay line for one and two-photon Fock-states. To achieve uniform photon delays, the QDs' emission have been tuned to the transmission window related to the ground-state hyperfine-splitting, where group velocity dispersion is low. At high fractional delays, the preservation of photon statistics after the vapor has been proven for both quantum states of light .

For the QD's emission of a one-photon Fock-state under the π-pulse pumping, up to $\Delta t \approx 27\,\mathrm{ns}$ delay has been reached for the highest investigated temperature of $T_V = 133.42\,^{\circ}\mathrm{C}$. With regard to the pulse length of the photon, this corresponds to a fractional delay of above 50, while $n_g(\omega) \geq 33$ has been achieved. The acquired delays showed the expected exponential dependence on the vapor temperature, while the unchanged purity of the transmitted photons has been confirmed via second-order coherence measurements after the vapor. The fraction of undelayed photons has been found to be less than 1% for all delays, which confirmed the faithful operation of the realized delay line.

The interaction of the two-photon Fock-state, which was generated by exploiting the HOM effect, has also been studied. For a vapor transmission above 90%, this light state has been delayed by

$\sim 3\,\mathrm{ns}$ which corresponds to a fractional delay of about 5. The study of time-correlated single-photon counting of the two-photon state has been performed by postselection of coincidence events. The imperfect two-photon Fock-state has been evidenced in the temporal shape of the signal. Through correlation measurements after interaction with the vapor, the preservation of the quantum-state has also been confirmed. With this, we have demonstrated that a two-photon state is utilizable in a slow-light medium in the same way as a one-photon Fock-state.

The achieved high fractional delays under the preservation of the quantum-state have enabled first practical implementations of the delay line.

Impact of pulse distortion on HOM interference

In two complementary configurations of the Cs vapor, we have studied how the pulse distortion upon the delay in the vapor impacts HOM experiments. The preservation of the coherence of photon wavepackets after the vapor-induced delay has been proven via HOM measurements. Moreover, a networking scenario has been experimentally mimicked that includes photon synchronization prior to a two-photon interference. In addition, achievable HOM interference visibilities for the Cs vapor slow-light delay line have been determined.

In the first of the two vapor configurations, the impact of the vapor on the coherence of the single photon wavepackets has been studied. All photons have been first delayed in the vapor and then fed into the HOM setup such that both interfering photons were influenced by pulse distortion. The HOM interference visibility for all vapor-interacted photons has been found to be identical with the visibility of the bare QD emission for investigated delays of up to $\Delta t_V = 5.8\,\mathrm{ns}$. This has allowed to conclude that the slow-light effect preserves coherence and, despite the pulse distortion, does not induce dephasing to the photons' wavepacket.

In the second vapor configuration, the impact of pulse distortion was studied. The delay within the long arm of the unbalanced Mach-Zehnder interferometer of the HOM setup was partly induced by the

Cs vapor, such that only one photon got distorted before the quantum interference at the beam splitter. In this case, the HOM interference visibility was found to rapidly reduce upon increased vapor-induced delays. This has allowed to deduce the strong impact of temporal wavepacket mismatch for quantum interference upon propagation through a dispersive medium, which constitutes a severe limitation for real-world applications.

To assess the performance of synchronization by vapor-induced delays for Fourier-limited photons, simulations were performed showing a drastic impact of photon's decay constant on the achievable HOM interference visibilities. In particular, the shorter photons, as being widely used in high-performance QD single-photon sources, suffer from strong pulse distortion due to corresponding larger bandwidth. This calls once again for a restriction of the propagation in a dispersive medium to a minimum. In the case of deterministic storage schemes that incorporate dispersion, keeping the cell length as short as possible will be beneficial. In the end, research on pulse compression methods that apply to GHz-bandwidth photons remains a future task.

Status and prospects

The Cs-vapor delay line that has been investigated in this work represents a first step towards the realization of an on-demand operating storage medium. Indeed, a scheme for such a storage based on electromagnetically-induced transparency has been proposed for QD photons in alkali vapor [30]. Within the frame of the slow-light effect, we demonstrated that the minimum requirement posed on a quantum memory, namely, realization of state preserving delays, is fulfilled. However, there is a trade-off between achievable delays in the vapor and the absorption, which severely limits both the transmission of photons and maximum delays. Moreover, the pulse distortion due to strong dispersion, although exploited here for spectroscopic purposes, is a bottleneck for the important quantum interference at

a beam splitter, demonstrating the need for storage mechanisms that incorporate minimal dispersive propagation [20].

QD spectral diffusion, which has been studied here via the dispersive mapping provided by the slow-light medium, demonstrates the need for active and passive stabilization of the QD's environment [33]. The inhomogeneous broadening does not only reduce the coherence of the emitter, but it also prevents the effective coupling to atomic transitions for realizing quantum interfaces. To take the next step forward and realize a quantum memory for QD photons within quantum information processing, Fourier-limited emission is fundamental. The realization of such an emission relies not only on a proper excitation scheme, but also on high-quality sample growth and passivation of residual defects [28, 127].

A prevailing paradigm is the extension of QD emission to the telecom C-band wavelength ($\sim 1550\,\mathrm{nm}$) by quantum frequency conversion or suitable sample growth [92, 168]. Wide-bandwidth storage at these wavelengths has been realized in a rare-earth-ion doped photonic crystal resonator [169] and a rare-earth ion-doped cryogenically cooled silica fiber [170]. In principle, higher excited transitions of alkali vapors may also be suitable to realize slow-light or more advanced storage schemes for telecom wavelength photons. In particular, the two-photon transition $5S_{1/2} \rightarrow 5P_{3/2} \rightarrow 4D_{5/2}$ in Rubidium is suitable for this purpose with the first transitions around 780.2 nm and the second ones around 1529.3 nm.

As a first step towards this direction, we have acquired the linear response of a Rb vapor for telecom photons by performing a two-photon spectroscopy over the complete manifolds of the aforementioned transitions employing counter-propagating laser beams (see Fig. 6.1). In contrast to the linear response of the D-transitions acquired with a single laser, the incorporation of a second laser makes this scheme selective to the velocity of atoms which results in Doppler-free spectra. Still, the Doppler-effect manifests itself in the appearance of absorption lines in the two-dimensional spectrum, while their slope is determined by the ratio of the wavelengths of the counter-propagating lasers $\sim -780.2/1529.3 = -0.51$. The transmission of

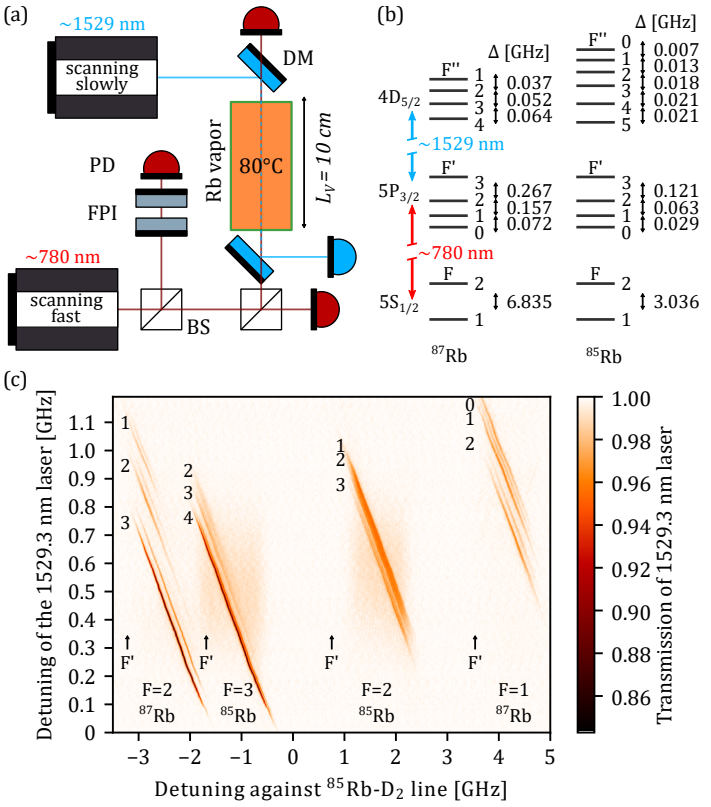

Figure 6.1. (a), Experimental setup of two-photon spectroscopy of Rubidium vapor $5S_{1/2} \rightarrow 5P_{3/2} \rightarrow 4D_{5/2}$ transitions at 780.2 nm and 1529.3 nm. An FPI serves for frequency linearization, dichroic mirrors (DM) guide the telecom wavelength laser on top of the red one. Photo diodes (PD) are used for detection of their transmission profile. The beam diameter of the red laser is four times larger than the telecom laser, while the intensities of linearly polarized lasers are $I_{780} = 15.4\,\mu\mathrm{W/mm^2}$ and $I_{1529} = 4.4\,\mu\mathrm{W/mm^2}$, respectively. (b), Energy-level diagram of the investigated two-photon transitions for both naturally occurring isotopes according to [167]. (c), Two-dimensional response of 1529 nm laser in Doppler-free two-photon spectroscopy of the hot Rb vapor with counter propagating beams. Ground-state hyperfine states appear column-wise.

the 1529.3 nm weak probe shows parallel absorption lines that exhibit a relative shift in the horizontal or vertical direction due to the hyperfine-splitting of the transitions. The map displays the majority of allowed transitions and yields their detunings, as listed in Fig. 6.1b. In contrast to a splitting of a few GHz of the ground-state $5S_{1/2}$, the splittings of $5P_{3/2}$ and $4D_{5/2}$ transitions are smaller by one and two orders of magnitude, respectively. Thus, the bandwidth restriction posed on the telecom photons to spectrally fit between the $5P_{3/2} \rightarrow 4D_{5/2}$-transitions for perceiving useful slow-light tightens to ~ 50 MHz and smaller. The reason for that lies also in the sharp absorption lines of widths of a few MHz, which according to Kramers-Kronig relations induce a dispersion profile that is also restricted to the same range. This calls once again for narrow bandwidth photons from QDs.

QD telecom wavelength single-photons have been developed and improved in recent years. However, the demonstrated emission is still far from being Fourier-limited and amounts to more than one GHz [171]. Embedding QDs in suitable cavities to reduce the impact of inhomogeneous broadening, as successfully implemented for the majority of QD sample structures in the ~ 900 nm range [25, 85], will keep the bandwidth broad due to a reduced lifetime and corresponding increased broadening. Given the need for a narrow bandwidth on the one hand to realize efficient photon storage in the vapor and the contradictory necessity to increase lifetime-limited bandwidth on the other hand, a new research field of spectral pulse compression techniques from the GHz to the MHz range eventually will become mandatory.

Chapter 7

Zusammenfassung

Die plakativ auch als die zweite Quantenrevolution [1] bezeichnete Entwicklung fortschrittlicher Quantentechnologien nähert sich seit der Jahrtausendwende immer mehr den begehrten praktischen Anwendungen. Diesem Zweck dienend werden verschiedene Quantensysteme untersucht, zu denen unter anderem Quantenzustände des Lichts [2–4], natürliche Atome und Ionen [5, 6], Defekte im Festkörper wie Stickstoff-Fehlstellen im Diamant [7] und Halbleiter-Quantenpunkte [8], sowie Quantisierungen in mesoskopischen supraleitenden [9] und nanomechanischen Strukturen gehören [10].

Im Rahmen der photonischen Quantentechnologien eignen sich Quantenzustände des Lichts besonders gut als Vermittler von Quanteninformation zwischen entfernten Knotenpunkten. Unter Verwendung von optischen Fasern oder Freiraumverbindungen zu Satelliten ist es vorgesehen, ein globales Quantennetzwerk [11] zu errichten. Es wird erwartet, dass diese Technologien, unter Verwendung von verschränkten Photonen und Quantenbits aus einzelnen Photonen, Vorteile für eine sichere Kommunikation [12–14], Fortschritte in der Informationsverarbeitung und Computing [15, 16], sowie Präzisionsmessung über die klassische Grenze hinaus ermöglichen [17–19].

Quantenspeicher werden in der Regel in langlebigen Spin-Grundzuständen realisiert [20] und spielen eine zentrale Rolle bei der Verarbeitung und Synchronisation von Quantenbits. Die Realisierung eines Speichers in Quantensystemen, die sich zur Erzeugung von Quantenzuständen des Licht mit hoher Repetition eignen,

stellt sich aufgrund von kurzen Kohärenzzeiten als äußerst schwierig dar [2–4]. Daher liegt der Schwerpunkt in jüngster Zeit auf hybriden Quantensystemen [21–23], welche die komplementären Stärken der einzelnen Systeme zusammenführen sollen, um den Anforderungen praktischer Quantentechnologien gerecht zu werden. Die Realisierung eines Quantenspeichers, welches in der Lage ist, die von nicht-klassischen Lichtzuständen getragene Information zu speichern und abzurufen, wird einen enormen Einfluss auf verschiedene Bereiche der photonischen Quantentechnologien haben.

Als Emitter einzelner und verschränkter Photonen demonstrierten Halbleiter Quantenpunkte in den letzten Jahren beeindruckende Fortschritte [8,24,25,27]. Maßgeblich dafür ist die starke Emission eines einzelnen Quantenpunkt-Übergangs in die Null-Phononen-Linie und ihre Kombination mit Mikroresonatorstrukturen. Die bisher berichteten höchsten Raten von detektierten Einzelphotonen (40 MHz bei 76 MHz Anregungsrate) [28] betreiben den Quantenpunkt in einem offenen Mikroresonator, während die beeindruckende Multi-Photonen-Interferometrie mit bis zu 20 Eingangsphotonen [16] kürzlich mit einem in Mikrosäulenresonator eingebetteten Quantenpunkt realisiert wurde. Bemerkenswerterweise handelt es sich bei beiden Emittern um einzelne InGaAs-Quantenpunkte, was die Stärke dieser Halbleitertechnologie für die Erzeugung und Sammlung von kohärenten Einzelphotonen offenbart.

Die Speicherung von Photonen zur Einführung einer Wartezeit von parallel laufenden Operationen erhöht die Effizienz von Quantengattern mit Mehrphotoneneingängen. Hinsichtlich der Synchronisation von Photonen bieten atomare Alkalidämpfe eine deterministische kohärente Speicherung und Wiedergewinnung [29–31]. Eine Schnittstelle, die einen Quantenspeicher für die Quantenpunkt-Emission in einem Alkalidampf realisiert, lässt jedoch aufgrund der Dekohärenz und des Rauschens in beiden Systemen immer noch auf sich warten. Innerhalb des Dampfes induzieren die starken Kontrollpulse, welche zur Speicherung einzelner Photonen benötigt werden, Rauschsignale über Prozesse wie Raman-Streuung und Vier-Wellen-Mischung, die letztlich den Quantenzustand der abgerufe-

nen Photonen verfälschen [30, 32]. Die Filterung und Unterscheidung von Signalen wird im Zusammenhang mit der Verbreiterung der Quantenpunkt-Emissionsspektren zusätzlich erschwert. So reduziert die relativ große natürliche Linienbreite ihrer kurzen strahlenden Lebensdauer, welche aufgrund inhomogener Verbreiterungsprozesse weiter erhöht wird, die spektrale Übereinstimmung an die atomaren Übergänge [23, 33]. Aus diesen Gründen bleibt ein Quantenspeicher für Quantenpunkt-Photonen zunächst schwer realisierbar.

Dennoch wurden erste Schritte zur Schaffung einer praktischen Schnittstelle unternommen. Die Bemühungen konzentrierten sich darauf, eine effiziente Absorption von Quantenpunkt-Photonen durch Alkalidämpfe zu erreichen [34,35], Verlangsamung von Licht zu generieren, der auf die chromatischen Dispersion der Doppler-verbreiterten D-Übergänge basiert [23,36,37], und schmalbandige Filterung im Cäsium (Cs)-Dampf , die durch Faraday-anomaler Dispersion [38] realisiert wird. In diesen Studien wurde jedoch nicht-resonantes Pumpen oder resonante Dauerstrichanregung des Quantenpunkts verwendet, wodurch die Möglichkeit zur genau getakteten Emission fehlte, die für effiziente Mehrphotonen-Quantenimplementierungen so wichtig ist.

In dieser Arbeit realisieren wir eine Schnittstelle aus heißem Cs-Dampf und auf Abruf generierten Quantenpunkt-Photonen, welche die bestehende Forschung in den folgenden Aspekten erweitert. Erstens untersucht diese Studie Photonen unter resonanter π-Puls Anregung, welche die Auswirkungen der Anregung sowohl auf die Linienverbreiterung als auch auf den zeitlichen Jitter minimiert. Zweitens wird die Wechselwirkung von Fock-Zuständen des Lichts mit dem Dampf in verschiedenen Experimenten im Hinblick auf ihre optischen und quantenoptischen Eigenschaften untersucht. Drittens wird die Schnittstelle als neuartige spektroskopische Apparatur verwendet, die sehr aufschlussreiche Untersuchungen der internen Dynamik der Quantenpunkte ermöglicht. Die starke Dispersion im Dampf prägt den Frequenzbereich der Photonen durch eindeutige zeitliche Formen in den Zeitbereich ein. Mit diesem spektroskopischen Mittel wird das noch offene Problem der Charakterisierung der Dynamik spektraler Diffusion von Quantenpunkten angegangen, indem die

unter der π-Puls Anregung emittierten Photonen untersucht werden. Schließlich wird der Einfluss der Pulsverzerrung auf die Quanteninterferenz untersucht, um das Potenzial dieser Schnittstelle für Anwendungsszenarien zu bewerten.
Im Folgenden werden die wichtigsten Ergebnisse und Schlussfolgerungen zusammengefasst.

Erzeugung von Einzelphotonen auf Abruf
Gepulste resonante Anregung ist ein vielversprechendes Anregungsschema, um die Emissionsqualität der Halbleiter-Quantenpunkte zur höchsten Güte zu befördern. Mit dieser Technik wird die zufällige Population der Quantenpunkt-Zustände und die exzessive Dephasierung, die aus der nicht-resonanten Anregung der umgebenden Matrix resultiert, unterdrückt. Unter resonanter π-Puls Anregung haben wir aus dem geladenen Exzitonübergang einzelner InGaAs-Quantenpunkte reine Einzelphotonen auf Abruf erzeugt, um sie in Experimenten mit Cs Atomen zu nutzen.
Unter leistungsabhängiger, gepulster resonanter Anregung wurde die kohärente Anregung des geladenen Exzitonzustandes von Quantenpunkten durch deutliche Rabi-Oszillationen nachgewiesen. Die maximale Populationswahrscheinlichkeit des angeregten Zustands wurde am π-Puls auf ~ 0.75 geschätzt, während die Emission in die Null-Phononen-Linie ~ 0.78 betrug, so dass kohärente Photonen mit 60% Effizienz erzeugt wurden. Zusätzlich zur effizienten Photonenerzeugung wurde die sehr hohe Reinheit der Quantenpunkt-Emission im Ein-Photonen Fock-Zustand durch Korrelationsmessungen bestätigt. Unter der π-Puls Anregung ergab die normalisierte Intensitätskorrelation über alle untersuchten Quantenpunkte einen verschwindend geringen Wert von $g^{(2)}_{1,2}(0) = 0.014 \pm 0.006$.
Neben der hohen Reinheit an Einzelphotonen konnte auch eine zeitlich präzise Photonenemission nachgewiesen werden. Beides sind hervorstechende Merkmale der resonanten Anregung von Quantenpunkten. Zeitkorrelierte Einzelphotonendetektion auf der Null-Phononen-Linie des geladenen Exzitonübergangs zeigte eine scharfe Front der Photonen Wellenpakete und einen monoexponentiellen Zer-

fall, wobei eine mittlere Zerfallskonstante von $T_1 = 0.43 \pm 0.03$ ns über alle untersuchten Quantenpunkte extrahiert wurde.
Neben diesen sehr wertvollen Eigenschaften eines Zwei-Niveau Systems wurde der übliche starke Einfluss von Umgebungsfluktuationen, die an den Quantenpunkt-Übergang koppeln, identifiziert. Hochaufgelöste Spektren der Null-Phononen-Linie zeigten eine inhomogene Gaußsche-Verbreiterung, die bis zu einer Größenordnung breiter war als die Fourier-limitierte Linienbreite von $\Delta\omega_{FL} = 0.37 \pm 0.05$ GHz. Außerdem war oft eine zweite Emissionslinie in den Spektren vorhanden. Die Prozesse der Linienverbreiterung stellen eine große Herausforderung für die Verwendung von Quantenpunkt-Emittern in Multi-Photonen- und Multi-Emitter Quantenimplementierungen dar. Der erste Schritt zur Optimierung ist das Verständnis der Prozesse hinter der Verbreiterung unter π-Puls Anregung und konnte durch die vorliegende Quantenpunkt - Cs-Dampf Schnittstelle untersucht werden.

Erzeugung des Zwei-Photonen Fock-Zustandes unter Verwendung von HOM Interferenz

Durch Ausnutzung des HOM-Effekts wurden sowohl die Ununterscheidbarkeit der Einzelphotonen als auch die erfolgreiche Erzeugung von Zwei-Photonen Fock-Zuständen nach Quanteninterferenz an einem Strahlteiler bestätigt. Zur Realisierung der Propagation des Zwei-Photonen Zustandes im Cs-Dampf und dessen zeitkorrelierten Detektion wurde das übliche HOM Experiment erweitert. Ein zusätzlicher Strahlteiler, der nach der Interferenz in einem Ausgangsarm platziert wurde, erlaubte in einer Korrelationsmessung, die Erzeugung von Zwei-Photonen Fock-Zuständen über erhöhte Koinzidenzen zu verifizieren.

Die mittlere Überlappung der Photonenwellenpakete interferierender Photonen ist durch die HOM Interferenzvisibilität gegeben. Anhand von verminderten Koinzidenzen im üblichen HOM Experiment konnten Visibilitäten von bis zu $V_{\mathrm{HOM}} = 0.53 \pm 0.03$ bestimmt werden. In der erweiterten Versuchsanordnung wurde durch das Messen erhöhter Koinzidenzen die gleiche Visibilität re-

produziert, was eine Fidelität von 53% des erzeugten Zwei-Photonen Zustands zum Zwei-Photonen Fock-Zustand bestätigte. Aus den Visibilitäteten konnte eine Kohärenzzeit von $T_2 \approx T_1 = 0.43\,\mathrm{ns}$ und eine zugrundeliegende Gaußsche-Verbreiterung von $\Delta\omega = 0.9\,\mathrm{GHz}$ FWHM abgeleitet werden. Diese Linienbreite (Kohärenzzeit) ist um einen Faktor $3 - 4$ schmaler (höher) als die Emissionslinienbreite (Kohärenzzeit) des gesamten stationären Quantenpunkt-Spektrums. Diese Diskrepanz ist bei Festkörper Quantenemittern in der Regel anzutreffen und wird durch einen langsamen spektralen Diffusionsprozess verursacht.
Die hohe Kohärenz von Photonen aus einer einzigen Quelle, welche in kurzen Zeitabständen aufeinanderfolgend emittiert werden, konnte in der Literatur für Multiphotonen-Quantenimplementierungen mit hohen Fidelitäten ausgenutzt werden. Im Gegensatz dazu ist bei Implementierungen mit unabhängigen Quellen das Gesamtausmaß der Verbreiterung bestimmend, weshalb hohe Fidelitäten schwer erreichbar bleiben. Hier konnte mit einer Methode, welche die starke Dispersion des Cs-Dampfes ausnutzt, der Übergang von hohen HOM Interferenzvisibilitäten für sukzessiv emittierte Photonen von wenigen Nanosekunden Zeitunterschied zu den aus den verbreiterten stationären Emissionsspektren erwarteten niedrigen Visibilitäten aufgelöst werden.

Untersuchung der spektralen Diffusion von Quantenpunkten durch Photonen-Korrelationsspektroskopie nach Lichtverlangsamung im Cs-Dampf

In dieser Arbeit wurde eine Spektroskopiemethode eingeführt, welche auf den Effekt der Lichtverlangsamung basiert. Mit ihrer Hilfe konnte die Dynamik der spektralen Diffusion von Quantenpunkten anhand der emittierten Photonen charakterisiert werden.

Bisher wurde die starke Dispersion über die Cs-D_1-Linien als Mittel zur Lichtverlangsamung der durch den Dampf propagierenden Photonen genutzt. Über dies hinausgehend haben wir die Eindeutigkeit der detuningabhängigen Pulsverzerrung transmittierter Photonen ausgenutzt, um den Frequenzbereich auf den Zeitbereich

abzubilden. Auf diese Weise wurde eine neuartige Zeitbereichsspektroskopie realisiert, die sich zur Untersuchung von GHz-Linienbreiten der Quantenpunkt-Spektren eignet. Durch zeitkorrelierte Einzelphotonendetektion von transmittierten Photonen wurden die Emissionsspektren mehrerer Quantenpunkte bestimmt. Ihre exzellente Übereinstimmung zu unabhängig gemessenen hochaufgelösten Spektren direkt im Frequenzbereich demonstrierte die hervorragende Funktionalität des Messprinzips. Darüber hinaus wurde durch die Erweiterung auf eine Photonen-Korrelationsmessung an transmittierten Photonen nach der Wechselwirkung mit dem Dampf, die spektrale Korrelation der Emission untersucht. Die spektrale Diffusion der Quantenpunkt-Emissionslinie ergab eine zunehmende Verbreiterung der Korrelationspeaks in den jeweiligen Zeitskalen. Dies hat es ermöglicht, die Dynamik der spektralen Diffusion aufzudecken und die zeitliche Entwicklung der Kohärenz bzw. HOM Interferenzvisibilitäten bis zum stationären Limit zu bestimmen.

Aus den Ergebnissen der eingeführten Methode konnten wir den Ornstein-Uhlenbeck Prozess als ein geeignetes Modell zur Beschreibung der spektralen Diffusion von Quantenpunkten identifizieren. Die gesamte Linienverbreiterung ergab sich aus drei Anteilen: einem quasi-statischen Anteil, der eine phononeninduzierte Verbreiterung der Null-Phononen-Linie widerspiegelt, welche für die reduzierte HOM-Visibilität bereits auf kürzesten Zeitskalen verantwortlich ist; einem diffusiven Anteil, der Spin- und Ladungsfluktuationen auf 7 μs- bzw. 62 μs für ein Quantenpunkt unter rein resonanter Anregung widerspiegelt; und einem Anteil von Stark-Verschiebung induzierten diskreten Liniensprüngen auf einer Zeitskala im Millisekunden-Bereich, die den Besetzungszustand einer lokalen Ladungsfalle widerspiegelt. Bei Verwendung einer nicht-resonanten Laserinitialisierung des Ladungszustandes, wie sie an einem anderen Quantenpunkt untersucht wurde, konnte festgestellt werden, dass die einzige Korrelationszeit der spektralen Diffusion mit 22 μs kleiner ausfällt und von Fluktuationen der kontinuierlich erzeugten Ladungsträger dominiert wird. Die großen Rauschamplituden deuten darauf hin, dass die Quantenpunkt-Probe, welche auf einen Piezo-Trancducer geklebt

ist, eine höhere Temperatur als die erwartete 4 K besitzt. Zusätzlich offenbart sich Potenzial für Verbesserungen bei dem Probenwachstum, um Ladungsträgerfallen und übermäßige Defekte in der Nähe von Quantenpunkten weiter zu reduzieren.

Die für die verschiedenen Fluktuationen aufgedeckten Zeitskalen im Mikro- und Millisekundenbereich schließen die Lücke zwischen den berichteten Zeitskalen bei direkten Messungen der HOM Interferenzvisibilität und Untersuchungen, welche auf die Streuung eines schwachen resonanten Lasers im Dauerstrichbetrieb basieren. Dank dieses Fortschritts konnte die gesamte Performance eines Quantenemitters für quantenoptische Anwendungen durch eine einfache Photonen-Korrelationsmessung erfasst werden. Diese Bewertung wurde erreicht, indem die HOM Interferenzvisibilitäten von aufeinanderfolgenden Photonen bis zur stationären Grenze der Diffusionsprozesse abgeleitet wurden. Die Kenntnis der Zeitskalen und der Rauschamplituden nützt zum maßschneidern der Methoden, welche durch aktive und passive Kontrolle der Linienverbreiterung die Ununterscheidbarkeit des Photonenstroms möglichst hoch halten sollen.

Cs-Dampf Verzögerungsstrecke für Quantenzustände des Lichts

Die starke Dispersion des Dampfes an den Cs-D_1-Linien und der entsprechend hohe Gruppenindex $n_g(\omega)$ wurde nicht nur für die Spektroskopie ausgenutzt, sondern auch zur Bildung einer Verzögerungsstrecke für Ein- und Zwei-Photonen Fock-Zuständen. Um eine möglichst gleichmäßige Verzögerung für alle Photonen der verbreiterten Quantenpunkt Spektren zu erreichen, wurde die Emission der Quantenpunkte auf das „Transmissionsfenster" der Cs-D_1-Linien abgestimmt. Dieses rührt von der Hyperfeinaufspaltung des Grundzustandes, und erlaubt an der maximalen Transmission minimale Dispersion der Gruppengeschwindigkeit. Für diese untersuchte System wurde bei großen relativen Verzögerungen die Erhaltung der Photonenstatistik nach dem Dampf für beide Quantenzustände des Lichts erfolgreich nachgewiesen.

Für die Quantenpunkt-Emission eines Ein-Photonen Fock-Zustandes unter der π-Puls Anregung wurden für die höchste untersuchte Temperatur von $T_V = 133.42\,^{\circ}\mathrm{C}$ bis zu $\Delta t \sim 27\,\mathrm{ns}$ Verzögerung erreicht. Dies entspricht in Bezug auf die Photonenlänge einer relativen Verzögerung von über 50, wobei $n_g(\omega) \geq 33$ erreicht wurde. Die erreichten Verzögerungen zeigten die erwartete exponentielle Abhängigkeit von der Dampftemperatur, während die unveränderte Photonenstatik der transmittierten Einzelphotonen durch Korrelationsmessungen nach dem Dampf bestätigt wurde. Der Anteil der nicht verzögerten Photonen betrug für alle Verzögerungen weniger als 1%, was den zuverlässigen Betrieb der realisierten Verzögerungsstrecke bestätigte.

Die Wechselwirkung des durch Ausnutzung des HOM-Effekts erzeugten Zwei-Photonen Fock-Zustands mit dem Dampf wurde ebenfalls untersucht. Bei einer maximalen Dampftransmission von über 90% wurde dieser Lichtzustand um $\sim 3\,\mathrm{ns}$ verzögert, was einer relativen Verzögerung von etwa 5 entspricht. Die Untersuchung der zeitkorrelierten Einzelphotonendetektion des Zwei-Photonen Zustandes wurde durch Selektion von Koinzidenzereignissen durchgeführt. Dabei waren die Anzeichen eines unvollkommenen Zwei-Photonen Fock-Zustands an der zeitlichen Form des Signals erkennbar. Durch Korrelationsmessungen nach dem Dampf wurde auch in diesem Fall die Erhaltung des Quantenzustands bestätigt. Damit wurde gezeigt, dass ein Zwei-Photonen Zustand in gleicher Weise zur Verlangsamung verwendbar ist wie ein Ein-Photonen Fock-Zustand.

Die erreichten hohen Verzögerungen unter Erhaltung des Quantenzustands haben erste praktische Implementierungen der Verzögerungsstrecke ermöglicht.

Auswirkung der Pulsverzerrung auf die HOM-Interferenz
In zwei komplementären Konfigurationen des Cs-Dampfes haben wir untersucht, wie sich die Pulsverzerrung nach der Verzögerung im Dampf auf HOM Experimente auswirkt. Die Erhaltung der Kohärenz von Photonenwellenpaketen nach der dampfinduzierten Verzögerung

wurde durch HOM-Messungen nachgewiesen. Darüber hinaus wurde experimentell ein Quantennetzwerk nachgeahmt, das eine Synchronisation von Photonen vor einer Zwei-Photonen Interferenz vorsieht. Schließlich wurden erreichbare HOM Interferenzvisibilitäten für die Verzögerungsstrecke aus Cs-Dampf ermittelt.

In der ersten der beiden experimentellen Konfigurationen wurde der Einfluss des Dampfes auf die Kohärenz der einzelnen Photonenwellenpakete untersucht. Alle Photonen wurden zuerst im Dampf verzögert und anschließend in das HOM Interferometer eingespeist, so dass beide interferierenden Photonen durch die Pulsverzerrung beeinflusst waren. Es wurde festgestellt, dass die HOM Interferenzvisibilitäten für untersuchte Verzögerungen von bis zu $\Delta t_V = 5.8\,\mathrm{ns}$ identisch mit der Visibilität der reinen Quantenpunkt-Emission sind. Dies lässt den Schluss zu, dass Lichtverlangsamung die Kohärenz erhält und trotz einer Pulsverzerrung keine Dephasierung der Photonenwellenpakete induziert.

In der zweiten Konfiguration wurde der Einfluss der Pulsverzerrung untersucht. Die Verzögerung im langen Arm des unsymmetrischen HOM Interferometers wurde dabei teilweise durch den Cs-Dampf induziert, sodass nur ein Photon vor der Quanteninterferenz am Strahlteiler verzerrt wurde. In diesem Fall wurde festgestellt, dass die HOM Interferenzvisibilität mit zunehmender dampfinduzierter Verzögerung schnell abnimmt. Daraus konnte die starke Auswirkung der zeitlichen Wellenpaketverzerrung auf die Quanteninterferenz abgeleitet werden. Dies stellt eine starke Einschränkung für reale Anwendungen dar, bei denen Propagationen in dispersiven Medien vorkommen.

Um die Performance der Synchronisation durch dampfinduzierte Verzögerungen für Fourier-limitierte Photonen zu beurteilen, wurden Simulationen durchgeführt, die einen drastischen Einfluss der strahlenden Lebensdauer des Quantenpunkts auf die erreichbaren HOM Interferenzvisibilitäten zeigten. Insbesondere leiden die kürzeren Photonen aufgrund der entsprechend größeren Bandbreite, wie sie in den besten Quantenpunkt-Einzelphotonenquellen häufig vorkommen, unter starken Pulsverzerrungen. Dies erfordert,

nach Möglichkeit, eine Einschränkung der Propagation in einem dispersiven Medium auf ein Minimum. Im Falle deterministisch operierender Speicherschemata, die Dispersion beinhalten, sollte daher die Zelllänge so kurz wie möglich gehalten werden. Ferner bleibt die Erforschung von Pulskompressionsverfahren, die für Photonen mit GHz-Bandbreite anwendbar sind, eine Aufgabe für die Zukunft.

Status und Perspektiven

Die in dieser Arbeit untersuchte Verzögerunsstrecke aus Cs-Dampf stellt einen ersten Schritt in Richtung der Realisierung eines auf Abruf arbeitenden Speichermediums dar. Ein Schema für eine solche Speicherung, das auf elektromagnetisch induzierter Transparenz basiert, wurde für Quantenpunkt-Photonen in Alkalidampf vorgeschlagen [30]. Im Rahmen der Lichtverlangsamung konnten wir zeigen, dass die Minimalanforderung an einen Quantenspeicher, nämlich die Realisierung zustandserhaltender Verzögerungen, erfüllt ist. Allerdings muss ein Kompromiss zwischen den erreichbaren Verzögerungen im Dampf und der Absorption eingegangen werden, der sowohl die Transmission von Photonen als auch die maximalen Verzögerungen stark einschränkt. Darüber hinaus stellt sich die Pulsverzerrung aufgrund der starken Dispersion kritisch für die wichtige Quanteninterferenz an einem Strahlteiler dar, obwohl sie hier für spektroskopische Zwecke ausgenutzt wurde. Dies zeigt die Notwendigkeit von Speichermechanismen [20], welche die Propagation unter Dispersion minimieren.

Die spektrale Diffusion von Quantenpunkten, die hier umfassend untersucht wurde, zeigt die Notwendigkeit einer aktiven und passiven Stabilisierung der Umgebung des Quantenpunkts [33]. Die inhomogene Verbreiterung reduziert nicht nur die Kohärenz des Emitters, sondern verhindert auch die effektive Kopplung an atomare Übergänge zur Realisierung von Quantenschnittstellen. Um den nächsten Entwicklungsschritt zu machen und einen Quantenspe-

icher für Quantenpunkt-Photonen im Rahmen der Quanteninformationsverarbeitung zu realisieren, ist eine Fourier-limitierte Emission von grundlegender Bedeutung. Die Realisierung einer solchen Emission hängt nicht nur von einem geeigneten Anregungsschema ab, sondern auch von einem qualitativ hochwertigen Probenwachstum und der Passivierung von Restdefekten [28, 127].

Ein vorherrschendes Paradigma ist die Erweiterung der Quantenpunkt-Emissionswellenlänge durch Quantenfrequenzkonversion oder geeignetes Probenwachstum [92, 168] in das Telekom C-Band ($\sim 1550\,\mathrm{nm}$). Speicherung breitbandiger Photonen bei diesen Wellenlängen wurde in einem mit Seltenen Erde-Ionen dotierten photonischen Kristallresonator [169] und einer mit Seltene Erde-Ionen dotierten, kryogen gekühlten Silicafaser [170] realisiert. Prinzipiell können auch höher angeregte Übergänge des Alkalidampfes geeignet sein, um Lichtverlangsamung oder Speicherschemata bei Telekomwellenlängen zu realisieren. Insbesondere der Zwei-Photonen Übergang $5S_{1/2} \rightarrow 5P_{3/2} \rightarrow 4D_{5/2}$ in Rubidium (Rb) mit den ersten Übergängen um 780.2 nm und den zweiten Übergängen um 1529.3 nm erscheint für diesen Zweck geeignet.

Als ersten Schritt in diese Richtung haben wir die lineare Antwort eines Rb-Dampfes für Telekom Photonen erfasst, indem wir eine Zwei-Photonen Spektroskopie über die kompletten Mannigfaltigkeiten der oben genannten Übergänge mit gegenläufigen Laserstrahlen durchgeführt haben (siehe Abb. 6.1). Im Gegensatz zum linearen Verhalten der D-Übergänge, die mit einem einzelnen Laser aufgenommen wurden, macht die Einbeziehung eines zweiten Lasers dieses Schema selektiv für die Geschwindigkeit der Atome, was zu dopplerfreien Spektren führt. Dennoch manifestiert sich der Doppler-Effekt im Auftreten von Absorptionslinien im zweidimensionalen Spektrum, wobei deren Steigung durch das Verhältnis der Wellenlängen der gegenläufigen Laser $\sim -780.2/1529.3 = -0.51$ bestimmt wird. Die Transmission des schwachen 1529.3 nm Signals zeigt parallele Absorptionslinien, die aufgrund der Hyperfeinaufspaltung der Übergänge eine relative Verschiebung in horizontaler oder vertikaler Richtung aufweisen. Die Karte zeigt die Mehrzahl der erlaubten Übergänge

und liefert deren Verstimmungen, wie sie in Abb. 6.1b aufgeführt sind. Im Gegensatz zu einer Aufspaltung von einigen GHz des Grundzustands $5S_{1/2}$ sind die Aufspaltungen der Übergänge $5P_{3/2}$ und $4D_{5/2}$ um eine bzw. zwei Größenordnungen kleiner. Eine nützliche Lichtverlangsamung der Telekom Photonen erfordert die spektrale Anpassung zwischen die $5P_{3/2}$- und $4D_{5/2}$-Übergänge. Somit limitieren sich die Bandbreiten auf $\sim 50\,\mathrm{MHz}$ und kleiner. Der Grund dafür liegt auch in den scharfen Absorptionslinien mit Breiten von wenigen MHz, die nach den Kramers-Kronig-Beziehungen ein Dispersionsprofil induzieren, das ebenfalls auf denselben Bereich beschränkt ist. Dies erfordert wiederum schmalbandige Photonen aus Quantenpunkten.

Einzelphotonen von Quantenpunkten bei Telekomwellenlängen wurden in den letzten Jahren entwickelt und verbessert. Die gezeigte Emission ist jedoch noch weit davon entfernt, Fourier-limitiert zu sein und liegt bei über einem GHz [92, 171]. Durch die Einbettung der Quantenpunkte in geeignete Resonatoren, um den Einfluss der inhomogenen Verbreiterung zu reduzieren, so wie es für die meisten Quantenpunkt-Probenstrukturen im $\sim 900\,\mathrm{nm}$-Bereich erfolgreich umgesetzt wurde [25, 85], bleibt die Bandbreite aufgrund der reduzierten Lebensdauer entsprechend breit. Angesichts der Forderung einer schmalen Linienbreite zur effizienten Realisierung der Photonenspeicherung im atomaren Dampf und der widersprüchlichen Notwendigkeit, die lebensdauerbegrenzte Bandbreite zu erhöhen, wird ein neues Forschungsfeld der spektralen Pulskompressionstechniken vom GHz- auf den MHz-Bereich notwendig werden.

Appendix A

Appendix

Derivation of the two-photon state in one output arm after HOM interference

To experimentally acquire the photon-correlation after the HOM interference inherent in an output arm of the beam splitter, an additional beam splitter was introduced into this mode, see Fig. 4.3. Starting with the interference of two single photon wavepackets $|1\chi_1^{0;3}\rangle = \int d\omega\ \chi_1^0(\omega)\hat{a}_3^\dagger(\omega)|0\rangle = \hat{A}_3^\dagger(\chi_1)|0\rangle$ and $\hat{A}_4^\dagger(\chi_2)|0\rangle$ at BS_1, the two-photon state after the first beam splitter is written as:

$$\hat{A}_3^\dagger(\chi_1)\hat{A}_4^\dagger(\chi_2)|0\rangle \overset{BS_1}{\mapsto} \frac{1}{2}\times$$
$$(\text{-}i\hat{A}_5^\dagger(\chi_1)\hat{A}_5^\dagger(\chi_2)+\hat{A}_5^\dagger(\chi_1)\hat{A}_6^\dagger(\chi_2)\text{-}\hat{A}_6^\dagger(\chi_1)\hat{A}_5^\dagger(\chi_2)\text{-}i\hat{A}_6^\dagger(\chi_1)\hat{A}_6^\dagger(\chi_2))|0\rangle \tag{A.1}$$

The experiments have considered the propagation of the photons in the spatial mode 5 and a photon-correlation after an additional beam splitter BS_2. Therefore, only the part of the above state which includes two photons in mode 5 is relevant. This results in the following

state after the second beam splitter:

$$\begin{aligned}&\text{-}i\hat{A}_5^\dagger(\chi_1)\hat{A}_5^\dagger(\chi_2)|0\rangle \overset{BS_2}{\mapsto} -\frac{1}{2}\times \\ &(i\hat{A}_7^\dagger(\chi_1)\hat{A}_7^\dagger(\chi_2)+\hat{A}_7^\dagger(\chi_1)\hat{A}_8^\dagger(\chi_2)+\hat{A}_8^\dagger(\chi_1)\hat{A}_7^\dagger(\chi_2)\text{-}i\hat{A}_8^\dagger(\chi_1)\hat{A}_8^\dagger(\chi_2))|0\rangle\end{aligned} \tag{A.2}$$

The correlations $G^{(2)}_{5,5}(t,\delta t)$ (see Eq. (2.17)) and $G^{(2)}_{7,8}(t,\delta t)$ end up to be proportional, which we have exploited for the experimental realization.

Moreover, the state in Eq. (A.2) has been used to study the propagation of the two-photon state $\hat{A}_5^\dagger(\chi_1)\hat{A}_5^\dagger(\chi_2)|0\rangle$ through a Cs vapor. The state's temporal shape and acquired delay has been studied via TCSPCp as discussed in section 5.3.2.

Definition of the Normal and the Lorentz distributions

The Gaussian normal distribution with mean $\overline{\omega}$ and variance σ^2 as a function of x is given by $\mathcal{N}(\overline{\omega},\sigma^2) = \frac{1}{\sqrt{2\pi\sigma^2}}\exp(-\frac{(x-\overline{\omega})^2}{2\sigma^2})$.

The Lorentzian distribution with mean $\overline{\omega}$ and full width at half maximum $\Delta\omega$ is defined as $\mathcal{L}(\overline{\omega},\Delta\omega) = \frac{1}{\pi}\frac{\Delta\omega/2}{(\Delta\omega/2)^2+(x-\overline{\omega})^2}$.

List of Figures

List of Tables

Bibliography

[1] A. G. J. MacFarlane, J. P. Dowling, and G. J. Milburn, *"Quantum technology: the second quantum revolution"*, Philosophical Transactions of the Royal Society of London. Series A: Mathematical, Physical and Engineering Sciences **361**, 1655–1674 (2003)

[2] J.-W. Pan, Z.-B. Chen, C.-Y. Lu, H. Weinfurter, A. Zeilinger, and M. Żukowski, *"Multiphoton entanglement and interferometry"*, Rev. Mod. Phys. **84**, 777–838 (2012)

[3] B. Lounis and M. Orrit, *"Single-photon sources"*, Rep. Prog. Phys. **68**, 1129 (2005)

[4] M. D. Eisaman, J. Fan, A. Migdall, and S. V. Polyakov, *"Invited review article: Single-photon sources and detectors"*, Review of Scientific Instruments **82**, 071101 (2011)

[5] A. Reiserer and G. Rempe, *"Cavity-based quantum networks with single atoms and optical photons"*, Rev. Mod. Phys. **87**, 1379–1418 (2015)

[6] R. Blatt and D. Wineland, *"Entangled states of trapped atomic ions"*, Nature **453**, 1008–1015 (2008)

[7] J. Wrachtrup and F. Jelezko, *"Processing quantum information in diamond"*, Journal of Physics: Condensed Matter **18**, S807–S824 (2006)

[8] P. Michler (Ed.), *"Quantum dots for Quantum Information Technologies"*, Springer International Publishing (2017)

[9] G. Wendin, *"Quantum information processing with superconducting circuits: a review"*, Reports on Progress in Physics **80**, 106001 (2017)

[10] P. Arrangoiz-Arriola, E. A. Wollack, Z. Wang, M. Pechal, W. Jiang, T. P. McKenna, J. D. Witmer, R. Van Laer, and A. H. Safavi-Naeini, *"Resolving the energy levels of a nanomechanical oscillator"*, Nature **571**, 537–540 (2019)

[11] C. Simon, *"Towards a global quantum network"*, Nature Photonics **11**, 678–680 (2017)

[12] L.-M. Duan, M. D. Lukin, J. I. Cirac, and P. Zoller, *"Long-distance quantum communication with atomic ensembles and linear optics"*, Nature **414**, 413–418 (2001)

[13] L. Childress, J. M. Taylor, A. S. Sørensen, and M. D. Lukin, *"Fault-tolerant quantum repeaters with minimal physical resources and implementations based on single-photon emitters"*, Phys. Rev. A **72**, 052330 (2005)

[14] J. L. O'Brien, A. Furusawa, and J. Vučković, *"Photonic quantum technologies"*, Nature Photonics **3**, 687– (2009)

[15] E. Knill, R. Laflamme, and G. J. Milburn, *"A scheme for efficient quantum computation with linear optics"*, Nature **409**, 46– (2001)

[16] H. Wang, J. Qin, X. Ding, M.-C. Chen, S. Chen, X. You, Y.-M. He, X. Jiang, L. You, Z. Wang, C. Schneider, J. J. Renema, S. Höfling, C.-Y. Lu, and J.-W. Pan, *"Boson sampling with 20 input photons and a 60-mode interferometer in a 10^{14}-dimensional hilbert space"*, Phys. Rev. Lett. **123**, 250503 (2019)

[17] M. W. Mitchell, J. S. Lundeen, and A. M. Steinberg, *"Super-resolving phase measurements with a multiphoton entangled state"*, Nature **429**, 161–164 (2004)

[18] T. Nagata, R. Okamoto, J. L. O'Brien, K. Sasaki, and S. Takeuchi, *"Beating the standard quantum limit with four-entangled photons"*, Science **316**, 726–729 (2007)

[19] M. Müller, H. Vural, C. Schneider, A. Rastelli, O. G. Schmidt, S. Höfling, and P. Michler, *"Quantum-dot single-photon sources for entanglement enhanced interferometry"*, Phys. Rev. Lett. **118**, 257402 (2017)

[20] A. I. Lvovsky, B. C. Sanders, and W. Tittel, *"Optical quantum memory"*, Nature Photon. **3**, 706–714 (2009)

[21] G. Kurizki, P. Bertet, Y. Kubo, K. Molmer, D. Petrosyan, P. Rabl, and J. Schmiedmayer, *"Quantum technologies with hybrid systems"*, Proc Natl Acad Sci USA **112**, 3866 (2015)

[22] A. A. Clerk, K. W. Lehnert, P. Bertet, J. R. Petta, and Y. Nakamura, *"Hybrid quantum systems with circuit quantum electrodynamics"*, Nature Physics **16**, 257–267 (2020)

[23] N. Akopian, L. Wang, A. Rastelli, O. G. Schmidt, and V. Zwiller, *"Hybrid semiconductor-atomic interface: slowing down single photons from a quantum dot"*, Nature Photon. **5**, 230–233 (2011)

[24] I. Aharonovich, D. Englund, and M. Toth, *"Solid-state single-photon emitters"*, Nature Photonics **10**, 631–641 (2016)

[25] P. Senellart, G. Solomon, and A. White, *"High-performance semiconductor quantum-dot single-photon sources"*, Nature Nanotechnology **12**, 1026–1039 (2017)

[26] I. Schwartz, D. Cogan, E. R. Schmidgall, Y. Don, L. Gantz, O. Kenneth, N. H. Lindner, and D. Gershoni, *"Deterministic generation of a cluster state of entangled photons"*, Science **354**, 434 (2016)

[27] M. Müller, S. Bounouar, K. D. Jöns, M. Glässl, and P. Michler, *"On-demand generation of indistinguishable polarization-entangled photon pairs"*, Nature Photon. **8**, 224–228 (2014)

[28] N. Tomm, A. Javadi, N. O. Antoniadis, D. Najer, M. C. Löbl, A. R. Korsch, R. Schott, S. R. Valentin, A. D. Wieck, A. Ludwig, and R. J. Warburton.
"A bright and fast source of coherent single photons", 2020

[29] D. F. Phillips, A. Fleischhauer, A. Mair, R. L. Walsworth, and M. D. Lukin, *"Storage of light in atomic vapor"*, Phys. Rev. Lett. **86**, 783–786 (2001)

[30] J. Wolters, G. Buser, A. Horsley, L. Béguin, A. Jöckel, J.-P. Jahn, R. J. Warburton, and P. Treutlein, *"Simple atomic quantum memory*

suitable for semiconductor quantum dot single photons", Phys. Rev. Lett. **119**, 060502 (2017)

[31] O. Katz and O. Firstenberg, *"Light storage for one second in room-temperature alkali vapor"*, Nature Communications **9**, 2074 (2018)

[32] S. E. Thomas, T. M. Hird, J. H. D. Munns, B. Brecht, D. J. Saunders, J. Nunn, I. A. Walmsley, and P. M. Ledingham, *"Raman quantum memory with built-in suppression of four-wave-mixing noise"*, Phys. Rev. A **100**, 033801 (2019)

[33] H. Vural, S. L. Portalupi, and P. Michler, *"Perspective of self-assembled ingaas quantum-dots for multi-source quantum implementations"*, Applied Physics Letters **117**, 030501 (2020)

[34] S. M. Ulrich, S. Weiler, M. Oster, M. Jetter, A. Urvoy, R. Löw, and P. Michler, *"Spectroscopy of the D_1 transition of cesium by dressed-state resonance fluorescence from a single (in,ga)as/gaas quantum dot"*, Phys. Rev. B **90**, 125310 (2014)

[35] J.-P. Jahn, M. Munsch, L. Béguin, A. V. Kuhlmann, M. Renggli, Y. Huo, F. Ding, R. Trotta, M. Reindl, O. G. Schmidt, A. Rastelli, P. Treutlein, and R. J. Warburton, *"An artificial rb atom in a semiconductor with lifetime-limited linewidth"*, Phys. Rev. B **92**, 245439 (2015)

[36] J. S. Wildmann, R. Trotta, J. Martín-Sánchez, E. Zallo, M. O'Steen, O. G. Schmidt, and A. Rastelli, *"Atomic clouds as spectrally selective and tunable delay lines for single photons from quantum dots"*, Phys. Rev. B **92**, 235306 (2015)

[37] R. Trotta, J. Martín-Sánchez, J. S. Wildmann, G. Piredda, M. Reindl, C. Schimpf, E. Zallo, S. Stroj, J. Edlinger, and A. Rastelli, *"Wavelength-tunable sources of entangled photons interfaced with atomic vapours"*, Nature Comm. **7**, 10375– (2016)

[38] S. L. Portalupi, M. Widmann, C. Nawrath, M. Jetter, P. Michler, J. Wrachtrup, and I. Gerhardt, *"Simultaneous faraday filtering of the mollow triplet sidebands with the cs-d1 clock transition"*, Nature Comm. **7**, 13632– (2016)

[39] P. Michler, A. Kiraz, C. Becher, W. V. Schoenfeld, P. M. Petroff, L. Zhang, E. Hu, and A. Imamoğlu, *"A quantum dot single-photon turnstile device"*, Science **290**, 2282–2285 (2000)

[40] P. Michler (Ed.), *"Single quantum dots: Fundamentals, applications and new concepts"*, Vol. 90 of *"Topics in applied physics"*, Springer-Verlag (Berlin, 2003)

[41] I. N. Stranski and L. Krastanow, *"Zur theorie der orientierten ausscheidung von ionenkristallen aufeinander"*, Monatshefte für Chemie und verwandte Teile anderer Wissenschaften **71**, 351–364 (1937)

[42] B. Urbaszek, X. Marie, T. Amand, O. Krebs, P. Voisin, P. Maletinsky, A. Högele, and A. Imamoglu, *"Nuclear spin physics in quantum dots: An optical investigation"*, Rev. Mod. Phys. **85**, 79–133 (2013)

[43] R. Pelzel.
"A comparison of movpe and mbe growth technologies for iii-v epitaxial structures".
2013

[44] U. Banin, Y. Cao, D. Katz, and O. Millo, *"Identification of atomic-like electronic states in indium arsenide nanocrystal quantum dots"*, Nature **400**, 542–544 (1999)

[45] M. Bayer, G. Ortner, O. Stern, A. Kuther, A. A. Gorbunov, A. Forchel, P. Hawrylak, S. Fafard, K. Hinzer, T. L. Reinecke, S. N. Walck, J. P. Reithmaier, F. Klopf, and F. Schäfer, *"Fine structure of neutral and charged excitons in self-assembled in(ga)as/(al)gaas quantum dots"*, Phys. Rev. B **65**, 195315 (2002)

[46] J. Hansom, C. H. H. Schulte, C. Le Gall, C. Matthiesen, E. Clarke, M. Hugues, J. M. Taylor, and M. Atatuïe, *"Environment-assisted quantum control of a solid-state spin via coherent dark states"*, Nature Physics **10**, 725–730 (2014)

[47] A. Högele, S. Seidl, M. Kroner, K. Karrai, R. J. Warburton, B. D. Gerardot, and P. M. Petroff, *"Voltage-controlled optics of a quantum dot"*, Phys. Rev. Lett. **93**, 217401 (2004)

[48] J. Houel, A. V. Kuhlmann, L. Greuter, F. Xue, M. Poggio, B. D. Gerardot, P. A. Dalgarno, A. Badolato, P. M. Petroff, A. Ludwig, D. Reuter, A. D. Wieck, and R. J. Warburton, *"Probing single-charge fluctuations at a* GaAs/AlAs *interface using laser spectroscopy on a nearby ingaas quantum dot"*, Phys. Rev. Lett. **108**, 107401 (2012)

[49] A. Berthelot, I. Favero, G. Cassabois, C. Voisin, C. Delalande, P. Roussignol, R. Ferreira, and J. M. Gérard, *"Unconventional motional narrowing in the optical spectrum of a semiconductor quantum dot"*, Nature Physics **2**, 759– (2006)

[50] Y.-M. He, Y. He, Y.-J. Wei, D. Wu, M. Atatüre, C. Schneider, S. Höfling, M. Kamp, C.-Y. Lu, and J.-W. Pan, *"On-demand semiconductor single-photon source with near-unity indistinguishability"*, Nature Nano. **8**, 213–217 (2013)

[51] J. C. Loredo, C. Antón, B. Reznychenko, P. Hilaire, A. Harouri, C. Millet, H. Ollivier, N. Somaschi, L. De Santis, A. Lemaître, I. Sagnes, L. Lanco, A. Auffèves, O. Krebs, and P. Senellart, *"Generation of non-classical light in a photon-number superposition"*, Nature Photonics **13**, 803–808 (2019)

[52] A. V. Kuhlmann, J. Houel, A. Ludwig, L. Greuter, D. Reuter, A. D. Wieck, M. Poggio, and R. J. Warburton, *"Charge noise and spin noise in a semiconductor quantum device"*, Nature Phys. **9**, 570–575 (2013)

[53] M. J. Stanley, C. Matthiesen, J. Hansom, C. Le Gall, C. H. H. Schulte, E. Clarke, and M. Atatüre, *"Dynamics of a mesoscopic nuclear spin ensemble interacting with an optically driven electron spin"*, Phys. Rev. B **90**, 195305 (2014)

[54] A. Reigue, J. Iles-Smith, F. Lux, L. Monniello, M. Bernard, F. Margaillan, A. Lemaitre, A. Martinez, D. P. S. McCutcheon, J. Mørk, R. Hostein, and V. Voliotis, *"Probing electron-phonon interaction through two-photon interference in resonantly driven semiconductor quantum dots"*, Phys. Rev. Lett. **118**, 233602 (2017)

[55] A. Reigue, R. Hostein, and V. Voliotis, *"Resonance fluorescence of a single semiconductor quantum dot: the impact of a fluctuating elec-*

trostatic environment", Semiconductor Science and Technology **34**, 113001 (2019)

[56] H. Vural, J. Maisch, I. Gerhardt, M. Jetter, S. L. Portalupi, and P. Michler, *"Characterization of spectral diffusion by slow-light photon-correlation spectroscopy"*, Phys. Rev. B **101**, 161401 (2020)

[57] F. Ripka, H. Kübler, R. Löw, and T. Pfau, *"A room-temperature single-photon source based on strongly interacting rydberg atoms"*, Science **362**, 446–449 (2018)

[58] S. Gao, O. Lazo-Arjona, B. Brecht, K. T. Kaczmarek, S. E. Thomas, J. Nunn, P. M. Ledingham, D. J. Saunders, and I. A. Walmsley, *"Optimal coherent filtering for single noisy photons"*, Phys. Rev. Lett. **123**, 213604 (2019)

[59] E. Wolf (Ed.), *"Progress in optics"*, Vol. 43, North Holland (2002)

[60] J. P. Khurgin and R. S. Tucker (Eds.), *"Slow Light: Science and applications"*, CRC Press (2008)

[61] H. Vural, S. L. Portalupi, J. Maisch, S. Kern, J. H. Weber, M. Jetter, J. Wrachtrup, R. Löw, I. Gerhardt, and P. Michler, *"Two-photon interference in an atom-quantum dot hybrid system"*, Optica **5**, 367–373 (2018)

[62] M. A. Zentile, J. Keaveney, L. Weller, D. J. Whiting, C. S. Adams, and I. G. Hughes, *"Elecsus: A program to calculate the electric susceptibility of an atomic ensemble"*, Computer Physics Communications **189**, 162 – 174 (2015)

[63] T. Udem, J. Reichert, R. Holzwarth, and T. W. Hänsch, *"Absolute optical frequency measurement of the cesium d_1 line with a mode-locked laser"*, Phys. Rev. Lett. **82**, 3568–3571 (1999)

[64] D. Steck, *"Quantum and atom optics"*(2007)

[65] B. E. A. Saleh and M. C. Teich, *"Fundamentals of Photonics"*, John Wiley & Sons, Inc. (2007)

[66] R. Loudon, *"The quantum theory of light"*, OUP Oxford (2000)

[67] G. Grynberg, A. Aspect, C. Fabre, and C. Cohen-Tannoudji, *"Introduction to quantum optics: From the semi-classical approach to quantized light"*, Cambridge University Press (2010)

[68] M. H. A. Reck, *"Quantum interferometry with multiports: Entangled photons in optical fibers"*, PhD thesis, (1996)

[69] K. J. Blow, R. Loudon, S. J. D. Phoenix, and T. J. Shepherd, *"Continuum fields in quantum optics"*, Phys. Rev. A **42**, 4102–4114 (1990)

[70] C. K. Hong, Z. Y. Ou, and L. Mandel, *"Measurement of subpicosecond time intervals between two photons by interference"*, Phys. Rev. Lett. **59**, 2044–2046 (1987)

[71] C. Santori, D. Fattal, J. Vučković, G. S. Solomon, and Y. Yamamoto, *"Indistinguishable photons from a single-photon device"*, Nature **419**, 594–597 (2002)

[72] T. Legero, T. Wilk, A. Kuhn, and G. Rempe, *"Characterization of single photons using two-photon interference"*, Elsevier (Amsterdam, 2006)

[73] R. Kubo, *"A stochstic theory of line shape"*, John Wiley & Sons, Inc. (1969)

[74] C. Santori, D. Fattal, J. Vuckovic, G. S. Solomon, and Y. Yamamoto, *"Single-photon generation with InAs quantum dots"*, New Journal of Physics **6**, 89–89 (2004)

[75] J. Yu, S. Yuan, J.-Y. Gao, and L. Sun, *"Optical pulse propagation in a fabry–perot etalon: analytical discussion"*, J. Opt. Soc. Am. A **18**, 2153–2160 (2001)

[76] M. Bayer and A. Forchel, *"Temperature dependence of the exciton homogeneous linewidth in* $\mathrm{in}_{0.60}\mathrm{ga}_{0.40}\mathrm{As}/\mathrm{GaAs}$ *self-assembled quantum dots"*, Phys. Rev. B **65**, 041308 (2002)

[77] N. Somaschi, V. Giesz, L. D. Santis, J. C., Loredo, M. P., Almeida, G. Hornecker, L. S. Portalupi, T. Grange, C. Antón, J. Demory, C. Gómez, I. Sagnes, N. D. Lanzillotti-Kimura, A. Lemaítre, A. Auffeves, A. G. White, L. Lanco, and P. Senellart, *"Near-optimal single-photon sources in the solid state"*, Nature Photon. **10**, 340–345 (2016)

[78] M. Schwartz, *"Fully integrated gaas-based quantum photonic circuits: resonant generation, splitting and detection of single-photon emission on-chip"*, PhD thesis, (2018)

[79] S. Unsleber, D. P. S. McCutcheon, M. Dambach, M. Lermer, N. Gregersen, S. Höfling, J. Mørk, C. Schneider, and M. Kamp, *"Two-photon interference from a quantum dot microcavity: Persistent pure dephasing and suppression of time jitter"*, Phys. Rev. B **91**, 075413 (2015)

[80] A. J. Ramsay, A. V. Gopal, E. M. Gauger, A. Nazir, B. W. Lovett, A. M. Fox, and M. S. Skolnick, *"Damping of exciton rabi rotations by acoustic phonons in optically excited* InGaAs/GaAs *quantum dots"*, Phys. Rev. Lett. **104**, 017402 (2010)

[81] K. Fischer, L. Hanschke, J. Wierzbowski, T. Simmet, C. Dory, J. Finley, J. Vučković, and K. Müller, *"Signatures of two-photon pulses from a quantum two-level system"*, Nature Physics **13**, 649–654 (2017)

[82] Z. X. Koong, D. Scerri, M. Rambach, T. S. Santana, S. I. Park, J. D. Song, E. M. Gauger, and B. D. Gerardot, *"Fundamental limits to coherent photon generation with solid-state atomlike transitions"*, Phys. Rev. Lett. **123**, 167402 (2019)

[83] A. J. Brash, J. Iles-Smith, C. L. Phillips, D. P. S. McCutcheon, J. O'Hara, E. Clarke, B. Royall, L. R. Wilson, J. Mørk, M. S. Skolnick, A. M. Fox, and A. Nazir, *"Light scattering from solid-state quantum emitters: Beyond the atomic picture"*, Phys. Rev. Lett. **123**, 167403 (2019)

[84] J. Wolters, A. W. Schell, G. Kewes, N. Nüsse, M. Schoengen, H. Döscher, T. Hannappel, B. Löchel, M. Barth, and O. Benson, *"Enhancement of the zero phonon line emission from a single nitrogen vacancy center in a nanodiamond via coupling to a photonic crystal cavity"*, Applied Physics Letters **97**, 141108 (2010)

[85] T. Grange, N. Somaschi, C. Antón, L. De Santis, G. Coppola, V. Giesz, A. Lemaître, I. Sagnes, A. Auffèves, and P. Senellart, *"Reducing phonon-induced decoherence in solid-state single-photon*

sources with cavity quantum electrodynamics", Phys. Rev. Lett. **118**, 253602 (2017)

[86] Y.-M. He, H. Wang, C. Wang, M.-C. Chen, X. Ding, J. Qin, Z.-C. Duan, S. Chen, J.-P. Li, R.-Z. Liu, C. Schneider, M. Atatüre, S. Höfling, C.-Y. Lu, and J.-W. Pan, *"Coherently driving a single quantum two-level system with dichromatic laser pulses"*, Nature Physics **15**, 941–946 (2019)

[87] A. Kurzmann, A. Ludwig, A. D. Wieck, A. Lorke, and M. Geller, *"Auger recombination in self-assembled quantum dots: Quenching and broadening of the charged exciton transition"*, Nano Lett. **16**, 3367–3372 (2016)

[88] M. C. Löbl, C. Spinnler, A. Javadi, L. Zhai, G. N. Nguyen, J. Ritzmann, L. Midolo, P. Lodahl, A. D. Wieck, A. Ludwig, and R. J. Warburton, *"Radiative auger process in the single-photon limit"*, Nature Nanotechnology **15**, 558–562 (2020)

[89] P. Kok, H. Lee, and J. P. Dowling, *"Creation of large-photon-number path entanglement conditioned on photodetection"*, Phys. Rev. A **65**, 052104 (2002)

[90] K. Toyoda, R. Hiji, A. Noguchi, and S. Urabe, *"Hong-ou-mandel interference of two phonons in trapped ions"*, Nature **527**, 74–77 (2015)

[91] R. Lopes, A. Imanaliev, A. Aspect, M. Cheneau, D. Boiron, and C. I. Westbrook, *"Atomic hong-ou-mandel experiment"*, Nature **520**, 66–68 (2015)

[92] J. H. Weber, B. Kambs, J. Kettler, S. Kern, J. Maisch, H. Vural, M. Jetter, S. L. Portalupi, C. Becher, and P. Michler, *"Two-photon interference in the telecom c-band after frequency conversion of photons from remote quantum emitters"*, Nature Nanotechnology **14**, 23–26 (2019)

[93] A. Thoma, P. Schnauber, M. Gschrey, M. Seifried, J. Wolters, J.-H. Schulze, A. Strittmatter, S. Rodt, A. Carmele, A. Knorr, T. Heindel, and S. Reitzenstein, *"Exploring dephasing of a solid-state quantum*

emitter via time- and temperature-dependent hong-ou-mandel experiments", Phys. Rev. Lett. **116**, 033601 (2016)

[94] J. C. Loredo, N. A. Zakaria, N. Somaschi, C. Anton, L. de Santis, V. Giesz, T. Grange, M. A. Broome, O. Gazzano, G. Coppola, I. Sagnes, A. Lemaitre, A. Auffeves, P. Senellart, M. P. Almeida, and A. G. White, *"Scalable performance in solid-state single-photon sources"*, Optica **3**, 433–440 (2016)

[95] H. Wang, Y. He, Y.-H. Li, Z.-E. Su, B. Li, H.-L. Huang, X. Ding, M.-C. Chen, C. Liu, J. Qin, J.-P. Li, Y.-M. He, C. Schneider, M. Kamp, C.-Z. Peng, S. Höfling, C.-Y. Lu, and J.-W. Pan, *"High-efficiency multiphoton boson sampling"*, Nature Photonics **11**, 361– (2017)

[96] H. Wang, Z.-C. Duan, Y.-H. Li, S. Chen, J.-P. Li, Y.-M. He, M.-C. Chen, Y. He, X. Ding, C.-Z. Peng, C. Schneider, M. Kamp, S. Höfling, C.-Y. Lu, and J.-W. Pan, *"Near-transform-limited single photons from an efficient solid-state quantum emitter"*, Phys. Rev. Lett. **116**, 213601 (2016)

[97] M. Rau, T. Heindel, S. Unsleber, T. Braun, J. Fischer, S. Frick, S. Nauerth, C. Schneider, G. Vest, S. Reitzenstein, M. Kamp, A. Forchel, S. Höfling, and H. Weinfurter, *"Free space quantum key distribution over 500 meters using electrically driven quantum dot single-photon sources—a proof of principle experiment"*, New Journal of Physics **16**, 043003 (2014)

[98] Y. Benny, Y. Kodriano, E. Poem, D. Gershoni, T. A. Truong, and P. M. Petroff, *"Excitation spectroscopy of single quantum dots at tunable positive, neutral, and negative charge states"*, Phys. Rev. B **86**, 085306 (2012)

[99] H. S. Nguyen, G. Sallen, C. Voisin, P. Roussignol, C. Diederichs, and G. Cassabois, *"Optically gated resonant emission of single quantum dots"*, Phys. Rev. Lett. **108**, 057401 (2012)

[100] K. D. Jöns, R. Hafenbrak, R. Singh, F. Ding, J. D. Plumhof, A. Rastelli, O. G. Schmidt, G. Bester, and P. Michler, *"Dependence of the redshifted and blueshifted photoluminescence spectra of single* $\mathrm{in}_x\mathrm{ga}_{1-x}\mathrm{As}$*/*GaAs *quantum dots on the applied uniaxial stress"*, Phys. Rev. Lett. **107**, 217402 (2011)

[101] L. Zhai, M. C. Löbl, J.-P. Jahn, Y. Huo, P. Treutlein, O. G. Schmidt, A. Rastelli, and R. J. Warburton, *"Large-range frequency tuning of a narrow-linewidth quantum emitter"*, Applied Physics Letters **117**, 083106 (2020)

[102] P. Siddons, C. S. Adams, C. Ge, and I. G. Hughes, *"Absolute absorption on rubidium d lines: comparison between theory and experiment"*, Journal of Physics B: Atomic, Molecular and Optical Physics **41**, 155004 (2008)

[103] D. Grischkowsky, *"Adiabatic following and slow optical pulse propagation in rubidium vapor"*, Phys. Rev. A **7**, 2096–2102 (1973)

[104] R. Boyd and D. Gauthier, *"Slow and fast light"*, Progress in Optics **43**, 363–385 (2001)

[105] T. Baba, *"Slow light in photonic crystals"*, Nature Photonics **2**, 465– (2008)

[106] J. B. Khurgin, *"Slow light in various media: a tutorial"*, Adv. Opt. Photon. **2**, 287–318 (2010)

[107] L. V. Hau, S. E. Harris, Z. Dutton, and C. H. Behroozi, *"Light speed reduction to 17 metres per second in an ultracold atomic"*, Nature **397**, 594–598 (1999)

[108] N. A. Mortensen and S. Xiao, *"Slow-light enhancement of beer-lambert-bouguer absorption"*, Applied Physics Letters **90**, 141108 (2007)

[109] Z. Shi and R. W. Boyd, *"Slow-light interferometry: practical limitations to spectroscopic performance"*, J. Opt. Soc. Am. B **25**, C136–C143 (2008)

[110] Z. Shi, R. W. Boyd, R. M. Camacho, P. K. Vudyasetu, and J. C. Howell, *"Slow-light fourier transform interferometer"*, Phys. Rev. Lett. **99**, 240801 (2007)

[111] U. Bortolozzo, S. Residori, and J. C. Howell, *"Precision doppler measurements with steep dispersion"*, Opt. Lett. **38**, 3107–3110 (2013)

[112] K. Goda and B. Jalali, *"Dispersive fourier transformation for fast continuous single-shot measurements"*, Nature Photonics **7**, 102–112 (2013)

[113] L. G. Cohen and C. Lin, *"Pulse delay measurements in the zero material dispersion wavelength region for optical fibers"*, Appl. Opt. **16**, 3136–3139 (1977)

[114] M. Avenhaus, A. Eckstein, P. J. Mosley, and C. Silberhorn, *"Fiber-assisted single-photon spectrograph"*, Opt. Lett. **34**, 2873–2875 (2009)

[115] Y. Okawachi, M. S. Bigelow, J. E. Sharping, Z. Zhu, A. Schweinsberg, D. J. Gauthier, R. W. Boyd, and A. L. Gaeta, *"Tunable all-optical delays via brillouin slow light in an optical fiber"*, Phys. Rev. Lett. **94**, 153902 (2005)

[116] D. Chen, G. R. Lander, K. S. Krowpman, G. S. Solomon, and E. B. Flagg, *"Characterization of the local charge environment of a single quantum dot via resonance fluorescence"*, Phys. Rev. B **93**, 115307 (2016)

[117] J. Li, T. P. White, L. O'Faolain, A. Gomez-Iglesias, and T. F. Krauss, *"Systematic design of flat band slow light in photonic crystal waveguides"*, Opt. Express **16**, 6227–6232 (2008)

[118] B. Wu, J. F. Hulbert, E. J. Lunt, K. Hurd, A. R. Hawkins, and H. Schmidt, *"Slow light on a chip via atomic quantum state control"*, Nature Photonics **4**, 776– (2010)

[119] M. Schwartz, E. Schmidt, U. Rengstl, F. Hornung, S. Hepp, S. L. Portalupi, K. llin, M. Jetter, M. Siegel, and P. Michler, *"Fully on-chip single-photon hanbury-brown and twiss experiment on a monolithic semiconductor-superconductor platform"*, Nano Lett. **18**, 6892–6897 (2018)

[120] S. Hepp, M. Jetter, S. L. Portalupi, and P. Michler, *"Semiconductor quantum dots for integrated quantum photonics"*, Advanced Quantum Technologies **2**, 1900020 (2019)

[121] R. Lettow, Y. L. A. Rezus, A. Renn, G. Zumofen, E. Ikonen, S. Götzinger, and V. Sandoghdar, *"Quantum interference of tun-*

ably indistinguishable photons from remote organic molecules", Phys. Rev. Lett. **104**, 123605 (2010)

[122] E. B. Flagg, A. Muller, S. V. Polyakov, A. Ling, A. Migdall, and G. S. Solomon, *"Interference of single photons from two separate semiconductor quantum dots"*, Phys. Rev. Lett. **104**, 137401 (2010)

[123] H. Bernien, L. Childress, L. Robledo, M. Markham, D. Twitchen, and R. Hanson, *"Two-photon quantum interference from separate nitrogen vacancy centers in diamond"*, Phys. Rev. Lett. **108**, 043604 (2012)

[124] J. H. Weber, J. Kettler, H. Vural, M. Müller, J. Maisch, M. Jetter, S. L. Portalupi, and P. Michler, *"Overcoming correlation fluctuations in two-photon interference experiments with differently bright and independently blinking remote quantum emitters"*, Phys. Rev. B **97**, 195414 (2018)

[125] R. N. E. Malein, T. S. Santana, J. M. Zajac, A. C. Dada, E. M. Gauger, P. M. Petroff, J. Y. Lim, J. D. Song, and B. D. Gerardot, *"Screening nuclear field fluctuations in quantum dots for indistinguishable photon generation"*, Phys. Rev. Lett. **116**, 257401 (2016)

[126] C. Latta, A. Hoğele, Y. Zhao, A. N. Vamivakas, P. Maletinsky, M. Kroner, J. Dreiser, I. Carusotto, A. Badolato, D. Schuh, W. Wegscheider, M. Atatüre, and A. Imamoglu, *"Confluence of resonant laser excitation and bidirectional quantum-dot nuclear-spin polarization"*, Nature Physics **5**, 758–763 (2009)

[127] A. V. Kuhlmann, J. H. Prechtel, J. Houel, A. Ludwig, D. Reuter, A. D. Wieck, and R. J. Warburton, *"Transform-limited single photons from a single quantum dot"*, Nature Comm. **6**, 824 (2015)

[128] B. Guha, F. Marsault, F. Cadiz, L. Morgenroth, V. Ulin, V. Berkovitz, A. Lemaître, C. Gomez, A. Amo, S. Combrié, B. Gérard, G. Leo, and I. Favero, *"Surface-enhanced gallium arsenide photonic resonator with quality factor of* 6×10^6 *"*, Optica **4**, 218–221 (2017)

[129] D. Najer, I. Söllner, P. Sekatski, V. Dolique, M. C. Löbl, D. Riedel, R. Schott, S. Starosielec, S. R. Valentin, A. D. Wieck, N. Sangouard,

A. Ludwig, and R. J. Warburton, *"A gated quantum dot strongly coupled to an optical microcavity"*, Nature **575**, 622–627 (2019)

[130] N. Leibovich and E. Barkai, *"Aging wiener-khinchin theorem"*, Phys. Rev. Lett. **115**, 080602 (2015)

[131] R. Dahbashi, J. Hübner, F. Berski, K. Pierz, and M. Oestreich, *"Optical spin noise of a single hole spin localized in an (inga)as quantum dot"*, Phys. Rev. Lett. **112**, 156601 (2014)

[132] C. Matthiesen, M. J. Stanley, M. Hugues, E. Clarke, and M. Atatüre, *"Full counting statistics of quantum dot resonance fluorescence"*, Scientific Reports **4**, 4911– (2014)

[133] G. Sallen, A. Tribu, T. Aichele, R. Andre, L. Besombes, C. Bougerol, M. Richard, S. Tatarenko, K. Kheng, and J.-P. Poizat, *"Subnanosecond spectral diffusion measurement using photon correlation"*, Nature Photon. **4**, 696–699 (2010)

[134] M. Abbarchi, T. Kuroda, T. Mano, M. Gurioli, and K. Sakoda, *"Bunched photon statistics of the spectrally diffusive photoluminescence of single self-assembled gaas quantum dots"*, Phys. Rev. B **86**, 115330 (2012)

[135] S. Gerhardt, J. Iles-Smith, D. P. S. McCutcheon, Y.-M. He, S. Unsleber, S. Betzold, N. Gregersen, J. Mørk, S. Höfling, and C. Schneider, *"Intrinsic and environmental effects on the interference properties of a high-performance quantum dot single-photon source"*, Phys. Rev. B **97**, 195432 (2018)

[136] X. Brokmann, M. Bawendi, L. Coolen, and J.-P. Hermier, *"Photon-correlation fourier spectroscopy"*, Opt. Express **14**, 6333–6341 (2006)

[137] C. Schimpf, M. Reindl, P. Klenovský, T. Fromherz, S. F. C. D. Silva, J. Hofer, C. Schneider, S. Höfling, R. Trotta, and A. Rastelli, *"Resolving the temporal evolution of line broadening in single quantum emitters"*, Opt. Express **27**, 35290–35307 (2019)

[138] F. M. Dekking, C. Kraaikamp, H. P. Lopuhaä, and L. E. Meester, *"A modern introduction to probability and statistics"*, Springer London (2005)

[139] W. B. Mims, K. Nassau, and J. D. McGee, *"Spectral diffusion in electron resonance lines"*, Phys. Rev. **123**, 2059–2069 (1961)

[140] K. Wódkiewicz, B. W. Shore, and J. H. Eberly, *"Pre-gaussian noise in strong laser–atom interactions: erratum"*, J. Opt. Soc. Am. B **1**, 759–759 (1984)

[141] J. Kempe, *"Quantum random walks: An introductory overview"*, Contemporary Physics **44**, 307–327 (2003)

[142] G. E. Uhlenbeck and L. S. Ornstein, *"On the theory of the brownian motion"*, Phys. Rev. **36**, 823–841 (1930)

[143] C. Laing and G. J. Lord (Eds.), *"Stochastic methods in neuroscience"*, Oxford University Press (2009)

[144] L. Fleury, A. Zumbusch, M. Orrit, R. Brown, and J. Bernard, *"Spectral diffusion and individual two-level systems probed by fluorescence of single terrylene molecules in a polyethylene matrix"*, Journal of Luminescence **56**, 15 – 28 (1993)

[145] R. G. Neuhauser, K. T. Shimizu, W. K. Woo, S. A. Empedocles, and M. G. Bawendi, *"Correlation between fluorescence intermittency and spectral diffusion in single semiconductor quantum dots"*, Phys. Rev. Lett. **85**, 3301–3304 (2000)

[146] O. Gazzano, T. Huber, V. Loo, S. Polyakov, E. B. Flagg, and G. S. Solomon, *"Effects of resonant-laser excitation on the emission properties in a single quantum dot"*, Optica **5**, 354–359 (2018)

[147] G. Éthier-Majcher, D. Gangloff, R. Stockill, E. Clarke, M. Hugues, C. Le Gall, and M. Atatüre, *"Improving a solid-state qubit through an engineered mesoscopic environment"*, Phys. Rev. Lett. **119**, 130503 (2017)

[148] J. H. Prechtel, A. V. Kuhlmann, J. Houel, L. Greuter, A. Ludwig, D. Reuter, A. D. Wieck, and R. J. Warburton, *"Frequency-stabilized source of single photons from a solid-state qubit"*, Phys. Rev. X **3**, 041006 (2013)

[149] J. Hansom, C. H. H. Schulte, C. Matthiesen, M. J. Stanley, and M. Atatüre, *"Frequency stabilization of the zero-phonon line of a*

quantum dot via phonon-assisted active feedback", Applied Physics Letters **105**, 172107 (2014)

[150] M. Bouillard, G. Boucher, J. Ferrer Ortas, B. Pointard, and R. Tualle-Brouri, *"Quantum storage of single-photon and two-photon fock states with an all-optical quantum memory"*, Phys. Rev. Lett. **122**, 210501 (2019)

[151] S. E. Harris, J. E. Field, and A. Imamoğlu, *"Nonlinear optical processes using electromagnetically induced transparency"*, Phys. Rev. Lett. **64**, 1107–1110 (1990)

[152] P. S. Michelberger, T. F. M. Champion, M. R. Sprague, K. T. Kaczmarek, M. Barbieri, X. M. Jin, D. G. England, W. S. Kolthammer, D. J. Saunders, J. Nunn, and I. A. Walmsley, *"Interfacing ghz-bandwidth heralded single photons with a warm vapour raman memory"*, New J. of Phys. **17**, 043006 (2015)

[153] R. Finkelstein, E. Poem, O. Michel, O. Lahad, and O. Firstenberg, *"Fast, noise-free memory for photon synchronization at room temperature"*, Science Advances **4** (2018)

[154] K. T. Kaczmarek, P. M. Ledingham, B. Brecht, S. E. Thomas, G. S. Thekkadath, O. Lazo-Arjona, J. H. D. Munns, E. Poem, A. Feizpour, D. J. Saunders, J. Nunn, and I. A. Walmsley, *"High-speed noise-free optical quantum memory"*, Phys. Rev. A **97**, 042316 (2018)

[155] M. Afzelius, C. Simon, H. de Riedmatten, and N. Gisin, *"Multimode quantum memory based on atomic frequency combs"*, Phys. Rev. A **79**, 052329 (2009)

[156] J.-S. Tang, Z.-Q. Zhou, Y.-T. Wang, Y.-L. Li, X. Liu, Y.-L. Hua, Y. Zou, S. Wang, D.-Y. He, G. Chen, Y.-N. Sun, Y. Yu, M.-F. Li, G.-W. Zha, H.-Q. Ni, Z.-C. Niu, C.-F. Li, and G.-C. Guo, *"Storage of multiple single-photon pulses emitted from a quantum dot in a solid-state quantum memory"*, Nature Communications **6**, 8652 (2015)

[157] E. Saglamyurek, N. Sinclair, J. Jin, J. A. Slater, D. Oblak, F. Bussieres, M. George, R. Ricken, W. Sohler, and W. Tittel, *"Broadband waveguide quantum memory for entangled photons"*, Nature **469**, 512–515 (2011)

[158] R. M. Camacho, M. V. Pack, J. C. Howell, A. Schweinsberg, and R. W. Boyd, *"Wide-bandwidth, tunable, multiple-pulse-width optical delays using slow light in cesium vapor"*, Phys. Rev. Lett. **98**, 153601 (2007)

[159] W. Zhang, M.-X. Dong, D.-S. Ding, S. Shi, K. Wang, Z.-Y. Zhou, G.-C. Guo, and B.-S. Shi, *"Interfacing a two-photon noon state with an atomic quantum memory"*, Phys. Rev. A **98**, 063820 (2018)

[160] A. J. Bennett, J. P. Lee, D. J. P. Ellis, T. Meany, E. Murray, F. F. Floether, J. P. Griffths, I. Farrer, D. A. Ritchie, and A. J. Shields, *"Cavity-enhanced coherent light scattering from a quantum dot"*, Science advances **2**, e1501256–e1501256 (2016)

[161] V. Leong, S. Kosen, B. Srivathsan, G. K. Gulati, A. Cerè, and C. Kurtsiefer, *"Hong-ou-mandel interference between triggered and heralded single photons from separate atomic systems"*, Phys. Rev. A **91**, 063829 (2015)

[162] F. Liu, A. J. Brash, J. OHara, L. M. P. P. Martins, C. L. Phillips, R. J. Coles, B. Royall, E. Clarke, C. Bentham, N. Prtljaga, I. E. Itskevich, L. R. Wilson, M. S. Skolnick, and A. M. Fox, *"High purcell factor generation of indistinguishable on-chip single photons"*, Nature Nanotechnology **13**, 835–840 (2018)

[163] *"Chapter 6 - pulse compression"*, In G. P. Agrawal (Ed.), *"Applications of Nonlinear Fiber Optics (Second Edition)"*, Academic Press (Burlington, 2008)

[164] M. Karpinski, M. Jachura, L. J. Wright, and B. J. Smith, *"Bandwidth manipulation of quantum light by an electro-optic time lens"*, Nature Photonics **11**, 53–57 (2017)

[165] J. Lavoie, J. M. Donohue, L. G. Wright, A. Fedrizzi, and K. J. Resch, *"Spectral compression of single photons"*, Nature Photonics **7**, 363–366 (2013)

[166] O. Morin, M. Körber, S. Langenfeld, and G. Rempe, *"Deterministic shaping and reshaping of single-photon temporal wave functions"*, Phys. Rev. Lett. **123**, 133602 (2019)

[167] J. Wang, H. Liu, G. Yang, B. Yang, and J. Wang, *"Determination of the hyperfine structure constants of the* ^{87}Rb *and* ^{85}Rb $4D_{5/2}$ *state and the isotope hyperfine anomaly"*, Phys. Rev. A **90**, 052505 (2014)

[168] S. L. Portalupi, M. Jetter, and P. Michler, *"InAs quantum dots grown on metamorphic buffers as non-classical light sources at telecom c-band: a review"*, Semiconductor Science and Technology **34**, 053001 (2019)

[169] M. F. Askarani, M. G. Puigibert, T. Lutz, V. B. Verma, M. D. Shaw, S. W. Nam, N. Sinclair, D. Oblak, and W. Tittel, *"Storage and reemission of heralded telecommunication-wavelength photons using a crystal waveguide"*, Phys. Rev. Applied **11**, 054056 (2019)

[170] E. Saglamyurek, J. Jin, V. B. Verma, M. D. Shaw, F. Marsili, S. W. Nam, D. Oblak, and W. Tittel, *"Quantum storage of entangled telecom-wavelength photons in an erbium-doped optical fibre"*, Nature Photonics **9**, 83–87 (2015)

[171] C. Nawrath, F. Olbrich, M. Paul, S. L. Portalupi, M. Jetter, and P. Michler, *"Coherence and indistinguishability of highly pure single photons from non-resonantly and resonantly excited telecom c-band quantum dots"*, Appl. Phys. Lett. **115**, 023103 (2019)

Publications

Articles with the focus on QD-Cs vapor interface:

- *Characterization of spectral diffusion by slow-light photon-correlation spectroscopy*
  H. Vural, J. Maisch, I. Gerhardt, M. Jetter, S. L. Portalupi, P. Michler, Phys. Rev. B **101**, 161401 (2020)

- *Delaying two-photon Fock-states in a hot cesium vapor using on-demand generated single-photons from a semiconductor quantum dot*
  H. Vural, S. Seyfferle, I. Gerhardt, M. Jetter, S. L. Portalupi, P. Michler, Phys. Rev. B **103**, 195304 (2021)

- *Controllable Delay and Polarization Routing of Single Photons*
  J. Maisch, H. Vural, M. Jetter, P. Michler, I. Gerhardt, S. L. Portalupi, Adv. Quant. Tech. **3**, 1900057 (2020)

- *Two-photon interference in an atom-quantum dot hybrid system*
  H. Vural, S. L. Portalupi, J. Maisch, S. Kern, J. H. Weber, M. Jetter, J. Wrachtrup, R. Löw, I. Gerhardt, P. Michler, Optica **5**, 367-373 (2018)

Articles with the focus on two-photon interference:

- *Perspective of self-assembled InGaAs quantum-dots for multi-source quantum implementations*
  H. Vural, S. L. Portalupi, P. Michler, Appl. Phys. Lett. **117**, 030501 (2020)

- *Two-photon interference in the telecom C-band after frequency conversion of photons from remote quantum emitters*
  J. H. Weber, B. Kambs, J. Kettler, S. Kern, J. Maisch, H. Vural, M. Jetter, S. L. Portalupi, C. Becher, P. Michler, Nat. Nanotech. **14**, 23-26 (2019)

- *Overcoming correlation fluctuations in two-photon interference experiments with differently bright and independently blinking remote quantum emitters*
  J. H. Weber, J. Kettler, H. Vural, M. Müller, J. Maisch, M. Jetter, S. L. Portalupi, P. Michler, Phys. Rev. B **97**, 195414 (2018)

- *Quantum-Dot Single-Photon Sources for Entanglement Enhanced Interferometry*
  M. Müller, H. Vural, C. Schneider, A. Rastelli, O. G. Schmidt, S. Höfling, P. Michler, Phys. Rev. Lett. **118**, 257402 (2017)

Erklärung der Selbständigkeit

Hiermit erkläre ich, dass ich die vorliegende Arbeit selbstständig und nur mit den angegebenen Hilfsmitteln angefertigt habe. Jeder Inhalt, der im Wortlaut oder sinngemäß anderen Werken entnommen wurde, ist durch Angabe der Quelle als Entlehnung kenntlich gemacht.

Ich habe mich andernorts nicht um einen Doktorgrad beworben und besitze keinen entsprechenden Titel.

Ich erkläre die Kenntnisnahme der dem Verfahren zugrundeliegenden Promotionsordnung der Universität Stuttgart vom 1. September 2011.

Stuttgart, im Dezember 2020

Hüseyin Vural